Efficient Perovskite Solar Cells for Monolithic Perovskite-Organic Tandem Solar Cells



Yun Xiao

Corpus Christi College

Department of Physics

University of Oxford

A thesis submitted for the degree of

Doctor of Philosophy

Hilary Term 2023

This thesis is dedicated to my family.

Declaration

I declare that the work in this thesis is my own work and not that of others, unless specifically indicated.

Abstract

Climate change and energy crisis are regarded as the two main global challenges threating the modern society. In this context, the development of photovoltaic solar cells has been placed on great expectations due to their clean and renewable energy features. As one representative among the emerging photovoltaic technologies, perovskite solar cells (PSCs) have made huge progress during the past decade. Pairing with another skyrocketing organic solar cells (OSCs), it is expected to further advance the device performance via realizing the monolithic perovskite-organic tandem solar cells (POTSCs), which will be presented in this thesis.

Firstly, the broad background and theory (**Chapter 1 & 2**) are introduced for general readers. Materials and Methods that used in this thesis are described in **Chapter 3**. As the wide bandgap (WBG) perovskites are vital to the POTSCs, a geometric manipulation strategy to optimize WBG PSCs is presented in **Chapter 4**. Next, a multifunctional buffer layer, ytterbium oxide, is reported in **Chapter 5** to alleviate the stability issue and contributes to efficient and stable PSCs. Targetting on the interfacial losses, a surface treatment is performed on WBG perovskite surface. To pair with the WBG subcells, the narrow bandgap (NBG) subcells based on organic absorbers is prepared. Followed by the design of interconnecting layers (ICL), the monolithc POTSCs comprising WBG-ICL-NBG are fabricated, where optical simiulation is carried out to provide optimization guidance (**Chapter 6**). Finally, the summary and hints for future studies are presented in **Chapter 7**.

Acknowledgement

Firstly, I would like to express deepest gratitude and profound thanks to my supervisors Prof. Henry J. Snaith and Prof. Moritz Riede. Henry gives me boundless freedom throughout my research time at Oxford and provides me with a great many supports in academia and beyond. Every meeting with him is worth expecting as he would always inspire you with new ideas, especially when you get lost and feel depressed. His enthusiasm and kindness does help me go through every *darkest hour* and cheer me up. Moritz is always patient and kind to guide me, step by step. I am impressive with his rigorous attitude of research. At the beginning of my DPhil study, he supported me to apply academic travels and explore wider fields, which not only enriches my DPhil journey but also deeply influences on my views of science and values. Secondly, I would like to thank Prof. Rui Zhu at Peking University. As a visiting scholar in Rui's group, he hosts me with meticulous care. He supports me without any reservation, enabling me to learn know-how and tricks that contributes a lot to my DPhil study.

Next, I would thank all my colleagues and friends in Snaith group, AFMD group and Rui's group: Hao, Hanyang, Irfan, Anna, Pascal, Sameer, Alberto, Bingjun, Grey, Andreas, Bernd, Pierluigi, Olivia, Suhas, Pietro, Alex, Mike, David, Nicky, Spencer, Suer, Peng, Deying, Shunde, Maotao, Hongyu, Lichen, Lei, Qiuyang, Xiaoyu, Fan, Yongqiang, Qixuan, Xiaohan, Rui, Jiang, Haoming, Haoxin, Tianyu, Yuchang, etc..

I also thank several groups within the University and around the global. Thanks you to Prof. Andrew Watt (Materials), Prof. Zheng-Hong Lu (Toronto), Prof. Laura Herz (Physics), Prof. Xiaojun Li (ICCAS).

Many thanks go to all the staffs at Physics and Corpus Christi, especially to Clare, Rachel and Jin, who support me throughout these years.

I sincerely thank my family. I cannot imagine how these years would be without your love and encouragement. You told me more than once that you always pride on me, and for me, I pride on you, too.

Finally I give thanks to myself. Thank you Yun for staying optimistic. Home is behind , go for the world ahead.

List of figures

Fig. 2.1 Structure of perovskite-type materials. **13**

Fig. 2.2 Absorption spectra of several PV materials. **14**

Fig. 2.3 Tuning the bandgap of perovskite via varying the I/Br raio. **15**

Fig. 2.4 Device structure of three main types of PSCs. **18**

Fig. 2.5 Working principle of PSCs and corresponding timescale for each step. **20**

Fig. 2.6 The roadmap of understanding ion migration. **26**

Fig. 2.7 The efficiency evolution of OSCs. **37**

Fig. 2.8 Energy offsets in typical organic blend. **40**

Fig. 2.9 Schematics of bandgap, Voc, and voltage loss in OSCs. **41**

Fig. 2.10 Schematics of energy losses in solar cells. **43**

Fig. 2.11 Evolution of three types of p-i-n perovskite-based TSCs **45**

Fig. 2.12 Schematics of a state-of-the-art perovskite-Si TSC. **47**

Fig. 2.13 Device structure for all-perovskite TSCs. **54**

Fig. 2.14 Interaction between the passivator and NBG perovskite films. **55**

Fig. 2.15 Working mechanism of the ICL of C60/$SnO_{1.76}$ **60**

Fig. 2.16 Relationship between bandgap combinations of two subcells and simulated efficiency. **68**

Fig. 3.1 A schematic for UPS spectra. **82**

Fig. 3.2 Schematics of layered stacks described by transfer matrix method. **87**

Fig. 4.1 Geometric morphology of perovskite films. Left: flat; Middle: hill; Right: mountain. **93**

Fig. 4.2 Device performance of PSCs with different geometries. **95**

Fig. 4.3 XRD results of mountain, flat and hill perovskite thin films. **97**

Fig. 4.4 UV-vis absorption results of mountain, flat and hill perovskite films. **98**

Fig. 4.5 Exploring the effects of geometric manipulation. **99**

Fig. 5.1 Overview of buffer layers. **107**

Fig. 5.2 Structural information for pure Yb film. **108**

Fig. 5.3 X-ray photoemission spectroscopy (XPS) spectra of the as-evaporated Yb film. **109**

Fig. 5.4 Morphological information for Yb_2O_3 films. **110**

Fig. 5.5 Band structures for Yb_2O_3. 111

Fig. 5.6 Photoemission spectroscopy of the lift-off samples. 112

Fig. 5.7 (a) Schematics of lift-off samples. Top-view SEM images of the peeled-off samples: (b) C60/Cu and (c) C60/Yb_2O_3/Cu. 114

Fig. 5.8 Photographs showing the color variation of devices after the aging. 115

Fig. 5.9 UPS depth profiling was measured at the Cu-electrode side. 116

Fig. 5.10 SEM images for NBG, MBG and WBG perovskites. 117

Fig. 5.11 Optoeletronic properties of perovskite films with differenct bandgaps. 118

Fig. 5.12 Device structure and performance for NBG, MBG and WBG PSCs. 119

Fig. 5.13 Statistic comparison between NBG PSCs with BCP and Yb_2O_3. 121

Fig. 5.14 Statistic comparison between WBG PSCs with BCP and Yb_2O_3. 122

Fig. 5.15 EQE of EL for NBG and WBG PSCs. 124

Fig. 5.16 Thermal stability tests for the encapsulated (a) NBG and (b) WBG PSCs with the BCP or Yb_2O_3 buffer layers in the N_2 glove box under 85°C in the dark. 126

Fig. 5.17 KPFM images showing the surface potential difference. 127

Fig. 5.18 Operational stability test for (a) NBG and (b) WBG PSCs. 128

Fig. 5.19 The chemical inertness of the Yb_2O_3 layer in the PSCs. 130

Fig. 5.20 Qualitative comparison for Yb_2O_3, BCP and SnO_x based on literatures.[33,301,321–323] 130

Fig. 6.1 Surface treatment for WBG perovskite. 137

Fig. 6.2 Optoelectronic properties of WBG perovskites. 138

Fig. 6.3 Device performance comparison between control and treated WBG PSCs. 139

Fig. 6.4 (a) Schematics of a POTSC. (b) Absorption spectra of perovskite and organic films. ... 140

Fig. 6.5 Device performance of perovskite and organic subcells. 141

Fig. 6.6 Properties of Yb_2O_3-based ICL. 142

Fig. 6.7 ICL working mechanism. 143

Fig. 6.8 Optical simulation for device optimization. 144

Fig. 6.9 Device performance of POTSC. 145

Fig. 6.10 Literature comparison of POTSCs. 146

Fig. 6.11 Statistics of device performance parameters for 31 POTSC devices. 146

List of tables

Table 2.1 Milestone of progress for p-i-n PSCs. Results in brackets are certified values. 18

Table 2.2 Commonly used materials for pin configured PSCs. 21

Table 2.3 Milestone of progress for WBG PSCs (E_g around 1.75 eV). 29

Table 2.4 Milestone of progress for OSCs. 38

Table 2.5 Summary of representative 2T perovskite-Si TSCs with p-i-n configuration. Values in the brackets are certified. 51

Table 2.6 Summary of representative 2T all-perovskite and POTSCs with p-i-n configuration. Values in the brackets are certified. 61

Table 3.1 Materials used in the experimental chapters. 72

Table 4.1 Photovoltaic parameters of champion mountain-, flat- and hill-type WBG PSCs. Average values and standard deviations are based on 12, 12 and 20 devices for each. 95

Table 4.2 Fitted data for TRPL measurements. 96

Table 5.1 Summary of photovoltaic parameters for the NBG, MBG and WBG PSCs. Average values and standard deviation are calculated based on 15 devices. 120

Table 5.2 Summary of representative efficient p-i-n NBG PSCs (1.53–1.56 eV) reported. 122

Table 5.3 Summary of representative efficient p-i-n WBG PSCs (1.75–1.80 eV) reported. 123

Table 6.1 Lifetime from fitting curves of the TRPL decay measurements according to methods introduced in Section 3.3. 138

Table 6.2 Device performance of WBG PSCs without and with surface treatment 138

Table 6.3 Summary of representative state-of-the-art p-i-n WBG (1.75~1.80 eV) PSCs in the literature. 139

Table 6.4 Key parameters and sources used in optical simulation. 143

Table 6.5 Device performance of champion POTSC and subcells. 146

Table 6.6 Summary of the key device performances of representative p-i-n POTSCs reported. 147

List of main abbreviations

AFM	Atomic force microscopy
ALD	Atomic layer deposition
CB	Conduction band
EL	Electroluminescence
EQE	External quantum efficiency
ERE	External radiative efficiency
ETL	Electron transporting layer
FA	Formamidine
FF	Fill factor
GIWAXS	Grazing incidence wide-angle X-ray scattering
HTL	Hole transporting layer
ICL	Interconnecting layer
ITO	Indium tin oxide
Jsc	Short-circuit current density
J-V	Current density - Voltage
KPFM	Kevin probe force microscopy
MA	Methylammonium
MBG	Mid-bandgap
MPP	Maximum power point
NBG	Narrow bandgap
NFA	Non-fullerene acceptor
n-i-p	Negative-intrinsic-positive
NIR	Near-infrared
OSC	Organic solar cell
PCE	Power conversion efficiency
p-i-n	Positive-intrinsic-negative
PL	photoluminescence
POTSC	Perovskite-organic tandem solar cell
PSC	Perovskite solar cell
PV	Photovoltaic
PVD	Physical vapor deposition
QFLS	Quasi-Fermi level splitting
REELS	Reflection electron energy loss spectroscopy
SAM	Self-assembly molecule
SEM	Scanning electron microscopy
SPO	Steady-state/stablized power output
SQ	Shockley-Queisser
SRH	Shockley-Read-Hall
(HR)TEM	High-resolved tramission electron microscopy
TRPL	Time-resolved photoluminescence
TSC	Tandem solar cell
UPS	Ultroviolet photoelectron spectroscopy
UV-vis	Ultraviolet-visible
Voc	Open-circuit voltage
VB	Valance band
WBG	Wide bandgap
XPS	X-ray photoelectron spectroscopy
XRD	X-ray diffraction

Contents

List of figures 1

List of tables 3

List of main abbreviations 4

Contents 5

1. Introduction 8

    1.1 Background and motivation 9

    1.2 Thesis outline 10

2. Theory 12

    2.1 Perovskite solar cells (PSCs) 13

        2.1.1 Fundamentals of perovskites 13

        2.1.2 Device physics 16

        2.1.3 Stability 28

        2.1.4 Wide bandgap (WBG) PSCs 29

    2.2 Organic solar cells (OSCs) 33

        2.2.1 Development of OSCs: from fullerene to NFA 33

        2.2.2 Working principles of NFA-OSC 38

    2.3 Perovskite-based tandem solar cells (TSCs) 42

        2.3.1 The concepts 42

        2.3.2 Main types of perovskite-based TSCs 45

        2.3.3 Design criteria for TSCs 66

3. Methods 71

    3.1 Materials 72

    3.2 Solar cells preparation 73

    3.3 Thin films and solar cells characterations 78

3.4 Optical simulation 84
4. Geometric manipulation for efficient WBG PSCs 88
4.1 Abstract 89
4.2 Introduction 89
4.3 Geometric manipulation 91
4.4 Device performance with different geometries 93
4.5 Mechanism 98
4.6 Conclusion 101
5. Efficient and stable PSCs enabled by ytterbium oxide 102
5.1 Abstract 103
5.2 Introduction 103
5.3 Properties of ytterbium oxide 106
5.4 The roles of ytterbium oxide at the interface 111
5.5 Device performance with universality verification 116
5.6 Device stability and conclusions 125
6. Yb_2O_3-based interconnecting layers for monolithic POTSCs 132
6.1 Abstract 133
6.2 Introduction 133
6.3 Surface treatment for WBG perovskite cells 136
6.4 Design of NBG organic cells and ICLs 140
6.5 Device performance of POTSC 143
6.6 Conclusion 147
7. Summary and outlook 148
8. Reference 151
Publications 186

1. Introduction

1.1 Background and motivation

Climate change and energy crisis are two main global challenges at present and are threating the peaceful development of modern society. To alleviate these issues, photovoltaics (PV) i.e. solar cells have received increasing attentions as they can directly convert the clean and renewable solar energy into electricity.

In recent years, the progresses in enhancing PV light-to-electricity power conversion efficiency (PCE) and lowering manufacturing cost greatly increase the competitivity of PV with other types of energy and thereby lead to the rapid expansion in energy market. These achievements are made mainly by silicon solar cells whose PCE has plateaued around 26% for more than two decades.[1] To further promote the utilization of solar energy, tremendous efforts have been put into the emerging thin-film solar cells, the latest generation PV technologies.

As two representatives of emerging solar cells, perovskite and organic solar cells (PSC, OSC) have both shown noticeable breakthrough in recent years. Driven by the advance in non-fullerene acceptors (NFA) design, the PCE of OSCs has come close to the threshold of 20%.[2,3] On the other hand, benefit from the multiscale defect passivation and composition engineering, PSCs efficiency has reached 26.1% certified recently, further narrowing the gap behind silicon solar cells.[4] To further increase the PCE to break the Shockley-Queisser limit, the maximum achievable PCE in theory for single-junction solar cells, it is inevitable to construct a tandem structure using more than one absorber for minimizing thermalization loss.[6] The features of PSC and OSC make them naturally suitable to pair with each other in tandem solar cells (TSC). Firstly, PSC and OSC have similar planar structures where intrinsic absorbers are sandwiched between

p-type and n-type contacts. Secondly, they are both solution-processable at low temperature. Thirdly, the main solvents to dissolve perovskites and organics are orthogonal. Fourthly, the bandgap of perovskites and organics are tuneable that enable complementary light absorption. In practice, the state-of-the-art narrow bandgap (NBG) perovskites have to employ Sn cations which is unstable in ambient environment, limiting the long-term stability of NBG perovskites. On the other hand, the highly efficient OSCs usually rely on the NFA with the bandgap between 1.2-1.4 eV, making them qualified substitutes as the NBG absorbers. Therefore, it is proper to pair a wide bandgap (WBG) perovskite with a NBG organic as the complementary absorbers to fabricate perovskite-organic tandem solar cells (POTSCs).

1.2 Thesis outline

The main focus of this thesis is on fabricating efficient POTSCs. A particular emphasis is laid on improving the performance of single junction PSCs with WBG, since it is usually the overall performance-limiting factor and placed as the front subcells which consequently act as the 'foundation' for the following layers.

Firstly, Chapter 1 provides a broad background to the topics to be discussed in this thesis.

Next, in Chapter 2, the theory and established knowledge in these topics are introduced. Section 2.1 discusses the perovskite materials properties, device physics, stability and the challenges of good WBG PSCs. Then Section 2.2 reviews the development of OSC from fullerene-based to NFA-based and associated working principles. Section 2.3 introduces the current status of perovskite-based TSCs and generates TSC design

criteria as the guidance.

Materials and Methods that used in this thesis are described in Chapter 3.

How to fabricate an efficient WBG PSC is then discussed in Chapter 4. Here a geometric manipulation strategy is proposed that can effectively boost the fill factor (FF) and obtain the overall improved performance.

Regarding the poor stability of PSCs, which is usually severer for WBG PSCs, in Chapter 5 a chemically stable Yb_2O_3 as the buffer layer at the charge transport layer/metal electrode interface is reported and how this buffer layer works towards stable and efficient PSCs is demonstrated.

The fabrication of monolithic POTSCs is presented in Chapter 6. The WBG PSC is firstly optimized via surface treatment, followed by the design of interconnecting layers (ICL) and finally the optimization of POTSCs.

In the final Chapter 7, the conclusions are summarized from the works in fabricating efficient and stable WBG PSCs and POTSCs. An outlook is given on the further optimization strategies in the future.

2. Theory

Part of this chapter (Section 2.3) is adapted from the review paper below, which has been submitted for publication.

Peng Chen[#], **Yun Xiao**[#], Shunde Li[#], Xiaohan Jia, Wei Zhang, Henry J. Snaith, Qihuang Gong and Rui Zhu. *The Promise and Challenges of Inverted Perovskite Solar Cells.*

[#]These authors contributed equally.

2.1 Perovskite solar cells (PSCs)

2.1.1 Fundamentals of perovskites

Material structures

As one type of minerals, perovskite was discovered for the first time by Prussian mineralogist Gustav Rose in 1839, named after the famous Russian mineralogist Count Lev A. Perovskiy.[7] Gradually, perovskite began to refer to a special kind of crystal structure and chemical formula ABX_3 (**Fig. 2.1**) following the first discovered perovskite $CaTiO_3$, where A = cation e.g. methylammonium ($CH_3NH_3^+$ or MA), formamidine ($CH_4N_2^+$ or FA) and Cs, B = divalent metal cation e.g. Pb and Sn, X = halogen anion e.g. I and Br. In fact, not only halide perovskites (ABX_3) owns such a featured crystal structure, but also oxide perovskites (ABO_3) e.g. $BaTiO_3$, $LiNbO_3$ own the structure as well. However, the latter does not possess notable potentials for PV applications, therefore to avoid ambiguity in this thesis 'perovskite' refer to halide perovskite (ABX_3) explicitly.

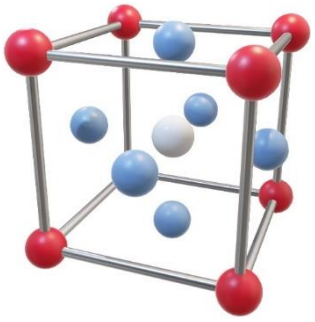


Fig. 2.1 Structure of perovskite-type materials.
Red, white and blue balls refer to A, B and X-site ions, respectively.

Optical properties

The electronic and optical properties of perovskite are vital to the performance of PSCs as the absorber material is responsible for converting light energy into electricity. The high absorption coefficient ~10^5 cm^{-1} (**Fig. 2.2**) is one of the most important features

of perovskite as the PV materials. It makes it possible that perovskite can absorb most of incident light within an ultrathin film of several hundreds of nanometers, enabling various ultrathin, light and flexible PV applications. Generally, optical transition type (direct or indirect transition) and transition probability are responsible for optical absorption. Perovskites own the merits of both GaAs (direct bandgap) and Si (p-p transition), giving rise to the high absorption coefficient (up to ~10^5 cm^{-1}).[8,9] Moreover, the absorption spectra of perovskites have steep band edges, indicating the well-ordered microstructure in crystalline materials, which is represented by Urbach energy.[10,11] Therefore, a small Urbach energy (high steepness for absorption edge) is usually desired for high-quality materials. Perovskites have been reported with small Urbach energy < 15 meV, which is much smaller than some semiconductors as shown in **Fig. 2.2** and very close to that of single-crystalline silicon (~11 meV).[12,13]

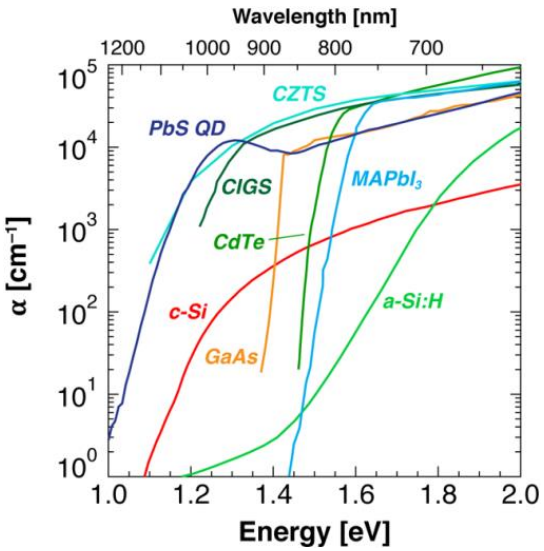


Fig. 2.2 Absorption spectra of several PV materials.
Reproduced with permission from Ref.[13]. Copyright 2017 American Chemical Society

The tunable bandgap and absorption range is another excellent feature. Different from typical PV materials e.g. Si, GaAs, CdTe, halide perovskites are a type of ionic crystals, allowing the easy tuning of bandgap and optical absorption by varying component ions,

crysrtal lattices and consequential band strctutres. For example, **Fig. 2.3** demonstrates the effect of I/Br ratio on the absorption edge.

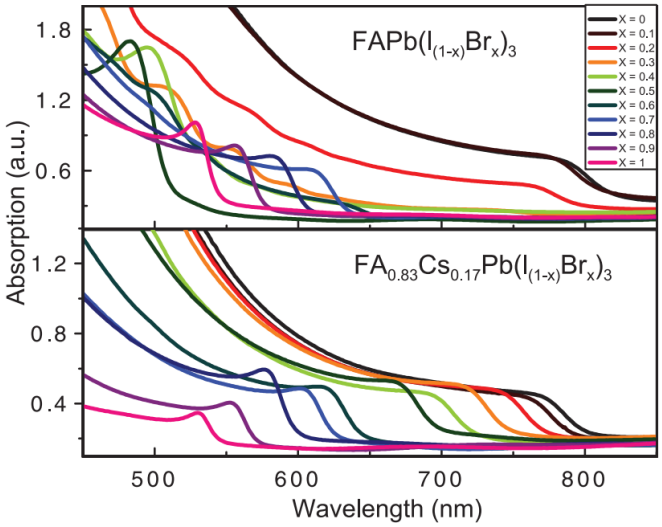


Fig. 2.3 Tuning the bandgap of perovskite via varying the I/Br raio.
UV-vis absorption spectra of $FAPb(I_{1-x}Br_x)_3$ and $FA_{0.83}Cs_{0.17}Pb(I_{1-x}Br_x)_3$, respectively. Reproduced with permission from Ref.[121] Copyright © 2016, American Association for the Advancement of Science

Carrier transport properties

The long charge carrier lifetime and diffusion length in perovskite is another superior property. The charge carrier diffusion length in perovskite materials is on the micrometer scale,[14,15] which is much larger than the typical perovskite film thickness around several hundreds of nanometers. This has been attributed to the so-called 'defect tolerance' that protects the carrier transport from traps. As the charge carrier transport will be significantly affected by the defects within the perovskite films, it is reasonable to account for this phenomenon from both sides of carriers *per se* and defects around. Focusing on the nature of carriers, it has been proved that carriers transport in perovskite in form of polarons which are able to screen the carrier-carrier and carrier-defect scattering and therefore possess long diffusion length.[16,17] From the viewpoint of defects, there is another explanation. Although there are tremendous defects in perovskite films on the scale of 10^{10} (monocrystalline) ~ 10^{16} (polycrystalline) cm^{-3},[18–

[20] such high defect density does not threat the long diffusion length and lifetime. Indeed, the carrier lifetime exceeding 20 μs can be obtained in a perovskite film with a high trap state density ~ 10^{15} cm^{-3},[21] which is much higher than other polycrystalline thin-film PV semiconductors e.g. CdTe (200 ns)[22] and CIGS (140 ns)[23]. It is believed that several frequent types of trap states either reside within the bands (valance bands, VB or conducting bands, CB) or are located at the shallow states near the band edges. The carriers trapped in the latter ones i.e. shallow defects can easily detrapped as free carriers. In fact, a clear and essential understanding on the origin of the superior carrier properties of perovskites is still lacking and debates are still going on. Explanations proposed to this puzzle includes intrinsic ferroelectricity, surface fields and diffusion, carrier−lattice coupling, large polaron formation.[24–32]

2.1.2 Device physics

Main milestone of progress

Over the past decade, the innovation of the device structure has been along with the perovskite material engineering and contributed synergically to the enhancement of PCE. The architectural evolution dates back to the age of dye-sensitized solar cells (DSSCs) in 2009 where perovskite was firstly used as the light harvester i.e. sensitizer to replace the organic dyes.[33] Adapted from the DSSC-like architecture containing liquid electrolyte, the first PSC was fabricated in 2009 and obtained a PCE of 3.8%.[34] As the perovskite dissolves rapidly in the corrosive liquid electrolyte which is indispensable for hole extraction in working cells, such PSC own a quite short life ~ several minutes that even makes the efficiency measurement difficult. The drawback of liquid-containing PSC was later solved by replacing the liquid electrolyte with 2,2',7,7'-Tetrakis[N,N-di(4-methoxyphenyl)amino] -9,9'-spirobifluorenea (spiro-

OMeTAD), a solid state hole transporting layer materials (HTL).[35] The transition to the all solid state PSCs enabled a longer lifetime ~ 500 h and a higher PCE of 9.7% in 2012.[36] Simultaneously, the first PSC breaking the 10% PCE threshold was reported with a novel structure where the usual conducting TiO_2 scaffold was replaced by insulating Al_2O_3.[37] It is worth mentioning that this novel architecture went the first step beyond the typical DSSC concept as it fully gets rid of the n-type conducting oxide. More importantly, this work for the first time discovered that perovskite has superior carrier transporting ability and also demonstrated the importance of reducing interfacial trap states, pointing the directions of following efforts. The excellent carrier transporting properties of perovskite reduces the necessity for employing bulk heterojunction and enables the simplicity of device structure. Inspired by this milestone work, a fully planar PSC with 15.4% PCE was successfully fabricated in 2013.[38] The fully planar structure confirmed that perovskites are able to behave as intrinsic layers to separate and transport both electrons and holes with long diffusion lengths. Moreover, the abandon of mesoporous oxide reduces the processing temperature from the high sintering temperature ~ 500℃ to sub 150℃. This simplifies the processing conditions and makes PSC compatible with flexible substrates. The concept of fully planar PSC also enables the positive-intrinsic-negative (p-i-n) configuration where HTL/ETL (ETL for electron transporting layers) can be deposited inversely below/above perovskite films (**Fig. 2.4**). The first p-i-n PSC was soon published with mere 3.9% and then enhanced to over 15% within one year.[39–41] The milestones of p-i-n PSCs have been summarised in the **Table 2.1**.

Table 2.1 Milestone of progress for p-i-n PSCs. Results in brackets are certified values.

Year	Perovskite	PCE (%)	Voc (V)	Jsc (mA cm^{-2})	FF	Ref.
2013	$MAPbI_3$	3.9	0.60	10.32	0.63	39
2013	$MAPbI_{3-x}Cl_x$	9.8	0.94	15.8	0.66	40
2014	$MAPbI_3$	14.9	/	/	/	41
2015	$MAPbI_3$	16.5	1.05	21.9	0.72	42
2017	$FA_{0.85}MA_{0.15}Pb(I_{0.85}Br_{0.15})_3$	21.0 (20.59)	1.14 (1.131)	23.7	0.78 (0.791)	43
2018	$(FA_{0.95}PbI_{2.95})_{0.85}(MAPbBr_3)_{0.15}$	21.51 (20.90)	1.21 (1.175)	22.50 (21.86)	0.790 (0.8137)	44
2020	$Cs_{0.05}(FA_{0.92}MA_{0.08})_{0.95}Pb(I_{0.92}Br_{0.08})_3$	23.0 (22.34)	1.17 (1.143)	24.1 (23.85)	0.816 (0.82)	45
2020	$Cs_{0.05}(FA_{0.98}MA_{0.02})_{0.95}Pb(I_{0.95}Br_{0.05})_3$	23.37 (22.75)	1.17 (1.164)	24.92 (24.69)	0.8017 (0.7916)	46
2021	MA0.6FA0.4PbI3	23.8	1.17	24.1	0.842	47
2022	$(FAPbI_3)_{0.95}(MAPbBr_3)_{0.05}$	24.3 (23.5)	1.19 (1.145)	24.8 (25.24)	0.829 (0.8125)	48
2022	$Cs_{0.05}FA_{0.85}MA_{0.1}PbI_3$	(23.91)	(1.15)	(24.90)	(0.83)	49
2022	$Cs_{0.05}(FA_{0.98}MA_{0.02})_{0.95}Pb(I_{0.95}Br_{0.05})_3$	25.0 (24.3)	1.18 (1.179)	25.68 (25.59)	0.823 (0.806)	50
2023	$Cs_{0.05}(FA_{0.95}MA_{0.05})_{0.95}Pb(I_{0.95}Br_{0.05})_3$	(25.39)	(1.21)	(24.8)	(0.8465)	51
2023	$Cs_{0.05}(FA_{0.95}MA_{0.05})_{0.95}Pb(I_{0.95}Br_{0.05})_3$	25.5 (24.90)	1.208 (1.203)	25.08 (25.02)	0.8437 (0.8273)	52
2023	/	25.86 (25.39)	1.187 (1.189)	25.69 (25.66)	0.8473 (0.8324)	53

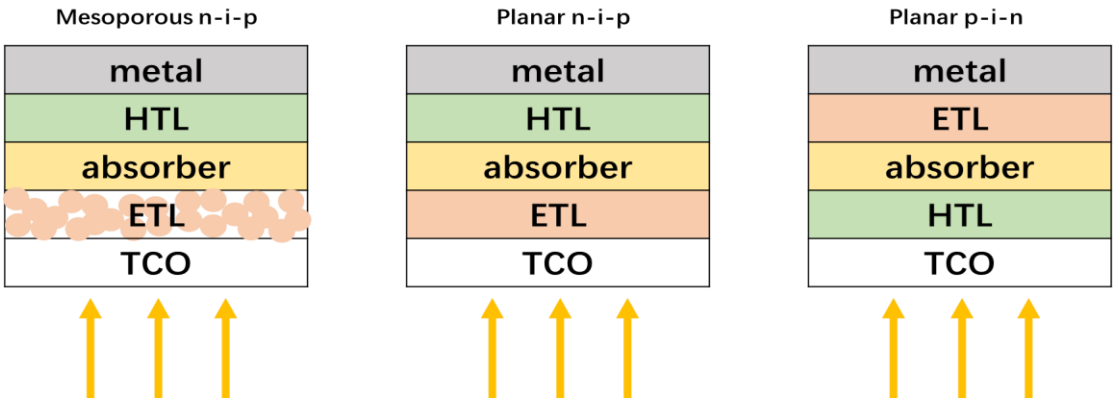


Fig. 2.4 Device structure of three main types of PSCs.
Left: mesoporous n-i-p; mid: planar n-i-p; right: planar p-i-n.

Structure and working principle

In recent years, planar architecture has demonstrated strong competitiveness due to the simplified structure, lower processing temperature and good compatibility with roll-to-

roll setup. To date, both types of planar PSCs, i.e. n-i-p and p-i-n configurations, have made great progress and reached the certified PCE of 25.73%[54] and 25.39%[51,53], respectively (note that the latest record for single-junction PSCs reaches 26.1% certified with unidentified type of configuration[5]). From the viewpoint of commercialization, however, the p-i-n configuration seems to be more promising compared to its n-i-p counterpart as it has many advantages e.g. better stability, ease of fabrication, negligible hysteresis and potential in integrated into tandem cells.[44,55,56] Therefore this thesis will focus on the p-i-n configuration.

As shown in **Fig. 2.4**, a typical p-i-n PSC mainly contains 5 component layers, namely, 1) front electrode (usually transparent conductive oxide, TCO), 2) HTL, 3) perovskite absorber layer, 4) ETL and 5) rear electrode (usually metal). The commonly used materials for each layer are summarized in **Table 2.2**. The working principle of a PSC is illustrated in **Fig. 2.5**. When a device is illuminated, the light passes through the front electrode and most of photons are absorbed by the perovskite layer. However, a small fraction of photons is absorbed by other non-perovskite layers which is known as parasitic absorption, one source of optical loss. Strategies to minimize parasitic absorption include selection of materials with weak absorption in visible spectrum. During the light illumination, photons with enough energy (larger than the bandgap) will be absorbed by perovskite layer to excite electrons from the valance band (VB) to conduction band (CB), which generates two opposite charge carriers i.e. electrons excited to the CB and holes left in the VB. These carriers with excess energy are called hot carriers as they initially inherit the photon energy which is greater than the bandgap so that their initial temperatures are above the perovskite lattice temperature. The lifetime of the hot carrier status is in the timescale of ps and then they will cool down

to the conduction band minimum (CBM) with the thermal energy release.[57,58] The hot carrier lifetime is related to carrier concentration, phonon bottleneck effect, large polaron character and electrostatic screening.[57,59–61] It is worthy noted that due to these mechanisms, halide perovskite possess much longer hot carrier lifetime (~2500 ps) than other PV materials e.g. GaAs (2 ps) and InN (10 ps), implying the greater potential of perovskite in exceeding SQ limit through maintaining greater open-circuit voltage (Voc) than Eg by hot carrier ultrafast extraction in the future.[62] After the carrier photogeneration, electrons and holes will transport and be selectively extracted by ETLs and HTLs respectively and transported to corresponding electrodes and external circuits. Along with the charge generation and extraction, there is always coexisting a competing charge recombination process which reduces the amounts of carriers extracted to external circuits. The efficient charge extraction depends both on the carrier properties of perovskite and the extraction ability of ETL/HTL. More information on recombination process will be given in next section.

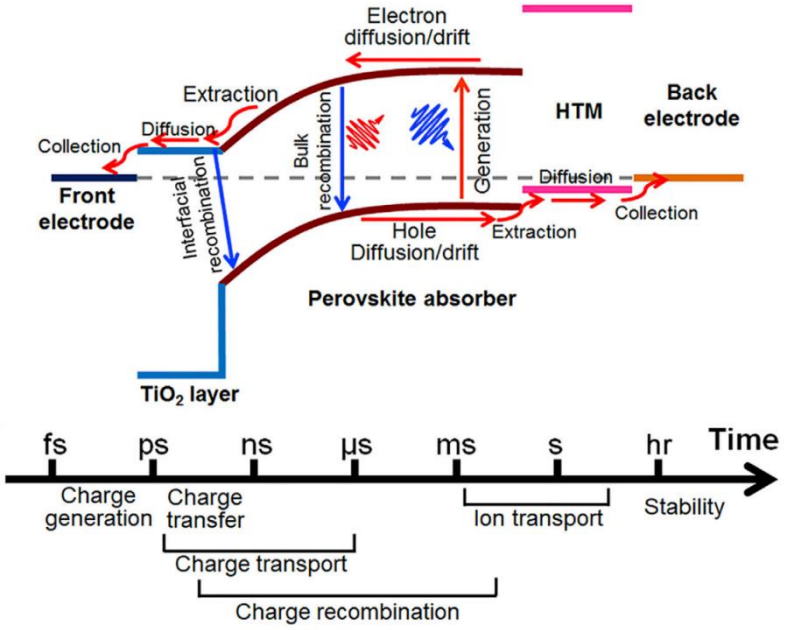


Fig. 2.5 Working principle of PSCs and corresponding timescale for each step. Reproduced with permission from Ref.[340] Copyright © 2018 Elsevier Inc

Table 2.2 Commonly used materials for pin configured PSCs.

Component layer	Materials
Rear electrode (metal)	Ag, Au, Cu
ETL	PCBM ([6,6]-phenyl-C61-butyric acid methyl ester), C60
Perovskite	$FAPbI_3$, $FA_yCs_{1-y}Pb(I_xBr_{1-x})_3$, $FA_yMA_zCs_{1-y-z}Pb(I_xBr_{1-x})_3$
HTL	PTAA (Poly[bis(4-phenyl)(2,4,6-trimethylphenyl)amine), poly-TPD (Poly(N,N'-bis-4-butylphenyl-N,N'-bisphenyl)benzidine), PEDOT:PSS (Poly(2,3-dihydrothieno-1,4-dioxin)-poly(styrenesulfonate)), SAM (self-assembly molecules), NiOx
Front electrode (TCO)	ITO (Indium tin oxide), FTO (Fluorine doped tin oxide)

Recombination

Along with the carrier generation and extraction, the recombination will coexist as the reverse process, including both radiative and non-radiative types which are competing processes. Note that in the calculation of theoretical maximum achievable PCE of solar cells, one assumption is assuming that all recombination processes within the solar cells are radiative where the electron-hole pair annihilation will release the energy in form of photons that can be further emitted into ambient or reabsorbed. However in practical devices, the nonradiative recombination widely occurs in the bulk and at the interfaces, where defects act as the traps, capture free carriers and mediate recombination. The nonradiative process lowers the density of free carriers, narrows the quasi-Fermi level splitting (QFLS) and eventually decreases the maximum open-circuit voltage (Voc) available. As the nonradiative recombination represents a major loss channel, it is essential to minimize it for achieving high efficiency.

The whole recombination of charge carriers can be expressed by the following equation:

$$\frac{dn}{dt} = -k_1 n - k_2 n^2 - k_3 n^3 \quad (Equation\ 2.1)$$

where n is carrier density, k is recombination rate constants with different order. The

first-order k_1 refers to the Shockley-Read-Hall (SRH) recombination, also known as (a.k.a) monomolecular recombination or defect/trap-assisted recombination as the trap process involves one charge carrier and one trap. The second-order k_2 refers to the band-to-band recombination aka bimolecular recombination as the process involves the annihilation of two opposite charge carriers i.e. one electron and one hole. The third-order k_3 refers to the Auger recombination which involves three carriers. These recombination rate constants can be determined using photoluminescence decay and pump probe spectroscopy.[63] The recombination rate $\frac{dn}{dt}$ is related to the photogenerated carrier density n, which is different under various light illumination. At the low light intensity, photogenerated carrier density is low ($<10^{15}$ cm^{-3}) and plenty of the trap states are unfilled. Therefore the dominate recombination mechanism is SRH recombination. The increasement of light intensity generates more charge carriers (10^{15}~10^{17} cm^{-3}). Once most traps have been filled, there are quite a few excess electrons and holes left and thus the bimolecular kinetics dominates the whole recombination. Further increasing the light intensity to a certain level can generate a substantial number of carriers ($>10^{17}$ cm^{-3}). In this stage, the crowded carriers increase the probability of three-body interactions and Auger recombination takes over the domination.

Note that the bimolecular recombination is radiative and is the inverse process of light absorption, which come to the same rate in thermal equilibrium according to the principle of detailed balance.[64] However both the defect-assisted and Auger recombination are non-radiative processes and therefore cause reduction in Voc, short-circuit current density (Jsc) and fill factor (FF). Usually the value of k_2=10^{-10}-10^{-11} cm^3 s^{-1} is much lower than k_1=10^6-10^8 s^{-1}, indicating the greater importance of defect-assisted recombination.[65–67] Since initiating the Auger regime requires a high light

intensity far beyond the usual illumination, such recombination is negligible as it is rare in normal working situation. It is in theory that non-radiative recombination can be mostly eliminated as it is strongly influenced by the quality of materials whereas the radiative recombination is actually the intrinsic property of materials. Therefore it is clear that the defect-assisted recombination is the main performance limiting factor to be tackled.

Ion migration

Fig. 2.6 depicts the progress on understanding the ion migration. Due to the intrinsic ionic and soft matter nature of perovskites, the constitute ions can migrate within the thin film and even diffuse into the adjacent layers, especially under the stimulation of external factors e.g. electric field, illumination. The ion migration deforms the perovskite crystal structure, changes the local stoichiometric ratio, and gives rise to numerous adverse phenomena. Indeed, not only the constituting ions in perovskite including both anions and cations, but also some ions from other device component layers, can migrate within the device. The migration tendency of ion species depends on the activation energy, i.e. an ion with lower activation energy is more easily activated to move. For instance, lead cations (Pb^{2+}) own much higher activation energy 2.31 eV than most of other ions, indicating that they will not migrate in most cases unless the perovskite is completely decomposed.[68] On the contrary, as one example with low activation energy (0.58 eV), iodine anions (I^-) become the most mobile ions in spite of their large ionic radius (2.06 Å) among halide ions.[69] The iodine migration within the mixed-anion perovskite layer directly gives rise to the phase segregation e.g. iodine-rich domains and bromide-rich domains, leading to the local inhomogeneous properties e.g. bandgap, lattice distortion.[70–72] Moreover, the high mobility and high reactivity

make iodine anions easily diffuse out of perovskite layers and react with other layers. For example, AgI and spiro-OMeTAD-I are the reaction products when iodine ions migrate into electrodes and HTLs, respectively.[73–76]

In addition to the anions, cations can also migrate and trigger notorious effects. Different from the lead cation with high activation energy 2.31 eV, A-site cations possess much lower activation energy e.g. 0.84 eV for MA, which can further decrease to 0.15 eV under the electric field and illumination.[69] The mobility of MA can be significantly accelerated particularly under the external stimulus, e.g. humidity, even leads to the formation of volatile gas. In contrast, due to the relatively larger molecular size (2.53 Å compared with 2.17 Å for MA), FA shows a much slower ion migration than MA, resulting in the enhanced stability for FA-based perovskites.[77] However, when it comes to FA-MA mixed cation perovskite, the differences between FA and MA in molecular sizes and dipole moments lead to the A-site cation redistribution vertically and laterally.[78–80] Cs is another common A-site cation and its addition with trace amount has been successfully proved to be useful strategy in depressing ion migration and boosting material structural stability.[81,82] One explanation attributes the mechanism to contraction of cubo-octahedral volume when incorporating partial Cs ion in FA-site and thereby enhance (FA–I) interaction.[83]

Apart from the intrinsic cations and anions in perovskite, ions from HTL/ETL and electrodes have also been confirmed to participate in ion migration within devices. For instance, lithium cations commonly added as the p-dopant in spiro-OMeTAD are highly mobile and will migrate into perovskite layers and even ETLs.[84–90] The formation of $LiPbX_3$ and LiX compounds indicates the redox reactions between lithium cations and

perovskite, drastically affecting the device stability.[85] With the lowest activation energy and molecular size, proton can migrate much easier than others. However, the origin of migrating protons is still elusive. One possible mechanism is that in humid environment water can dissociate into protons at the $MAPbI_3$ surface and promote the deprotonation of MA.[91,92] Detailed investigation with direct evidence is still absent. Regarding on the rear electrodes, noble metals e.g. Au and Ag are the common choices. Apart from that halide ions migrate to Ag and form silver halide, Ag ions can also migrate from electrodes into perovskite layers.[93–95] The low formation energy of interstitial Au and low diffusion barriers of Au in $MAPbI_3$ indicate that Au can also penetrate ETL/HTL and diffuse into perovskite layer easily.[93,96–100] Hence, suitable barrier materials are necessary to deposit to prevent the metal ion penetration. For example, a Cr layer of several nm is usually introduced before the deposition of Au electrode.[101,102] Evidences demonstrated that the Cr interlayer can successfully inhibit the Au ions diffusion through the spiro-OMeTAD into perovskite layers. To hinder the diffusion of Ag ions, a Bi interlayer has been inserted at the ETL/electrode interface.[103] The Bi interlayer with inert nature can reduce the outward iodine migration and inward Ag diffusion even at an elevated temperature of 85 degrees. In addition to the pure metal layers, metal oxides have also been proved to effectively act as the interlayer barriers for preventing the device degradation e.g. Cr_2O_3,[104] Al_2O_3 [105] and MoO_x[106].These studies demonstrate the detrimental effects of metal ion diffusion and stress the significance of interlayer barriers. Generally a suitable interlayer material should be inert to perovksites and adjacent layers, chemically stable at certain elevated temperature and ideally as thin as possible to avoid extra loss induced. In this thesis, a novel interlayer using ytterbium oxide will be discussed for fabricating efficient and stable p-i-n PSCs in Chapter 5.

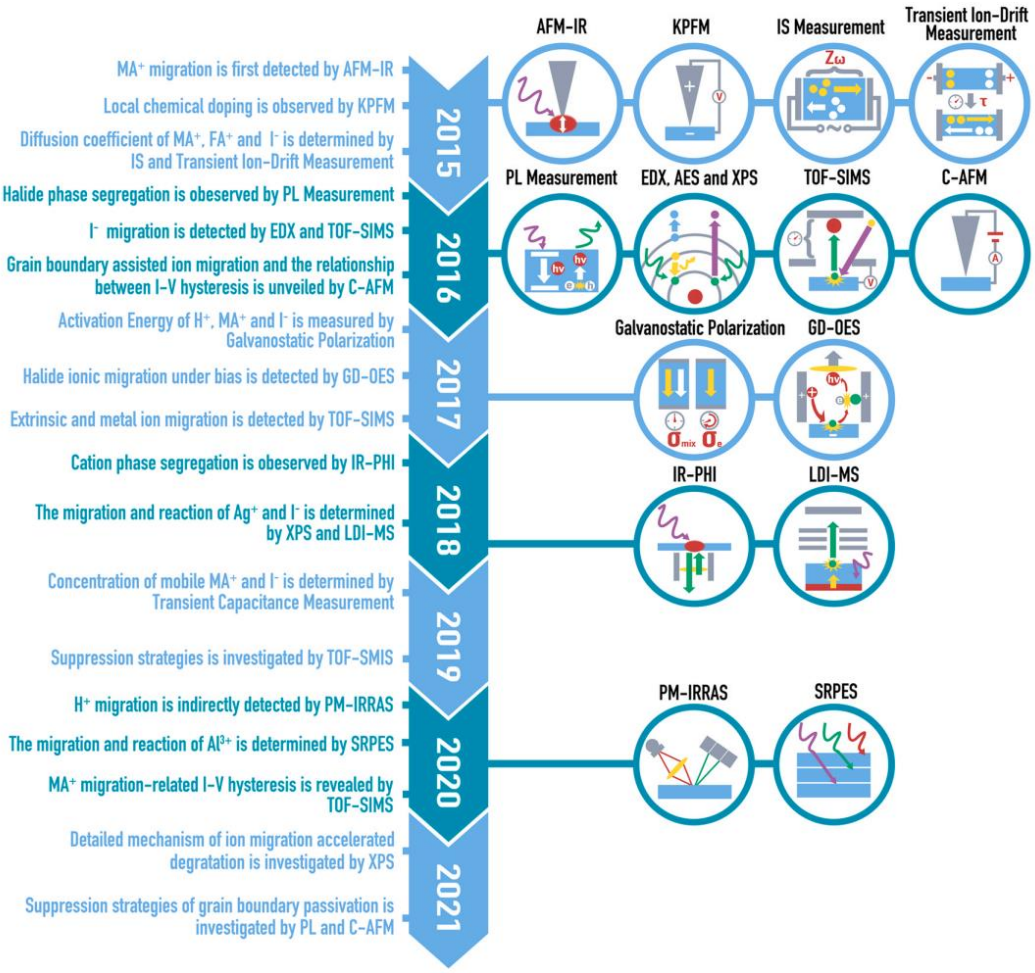


Fig. 2.6 The roadmap of understanding ion migration.
Reproduced with permission from Ref.[341] Copyright © 2022 Elsevier Ltd.

Hysteresis

Precise evaluation of PCE is important for assessing the performance of solar cells. However, a mismatch of current measured between forward scan (voltage bias from 0 V to Voc) and reverse scan (voltage bias from Voc to 0 V) has been long recognized, named as hysteresis, which remains unsolved and obstructs the performance assessment.[107] In fact, this phenomenon has been observed not only in PSCs but also other types of solar cells e.g. CIGS, DSSC, CdTe. More specifically, hysteresis is much more severe and commonly reported in conventional mesoscopic and planar nip configured PSCs than their pin counterparts. Although this thesis particularly focuses on the p-i-n structures which shows negligible hysteresis, the exploration of hysteresis

in general will sharpen the understanding of PSCs.

Due to the time-dependent photocurrent response phenomenon, the distinct current response at forward/reverse bias is believed to related to capacitive current, i.e. PSCs behave like capacitor in the presence of electric field.[108] The key challenge is to find out which components make PSCs like capacitors. Through the direct comparison between n-i-p and p-i-n structures without changing the perovskite composition, the significant alternation in the hysteresis clearly implies that no capacitive current and hysteresis measured in p-i-n structures in contrast to the large capacitive current and severe hysteresis in the n-i-p counterparts.[109] As keeping the perovskite layer the same, it seems other layers e.g. ETL/HTL ought to be responsible for the hysteresis. From the frequency-dependent capacitance measurement, TiO_2 and spiro-OMeTAD, commonly used ETL and HTL in n-i-p structure, are much more prone to accumulate charges at the perovskite/transporting layer interfaces than PCBM and PEDOT:PSS.[109,110] This delivers important information that the selective contact materials play key roles in determining the hysteresis and points out the direction for mitigation strategies. One potential origin of accumulated charges is derived from perovskite intrinsic ion migration, which become more severe with time under electric field, as introduced earlier. Additionally, charge carriers trapped in deep-level defects can also be released and disturb the normal photogenerated current-voltage response. And it is clearly that deep traps are associated with nonradiative recombination, and the severer nonradiative recombination, the severer hysteresis.

In summary, hysteresis is usually attributed to ion migration and defects with nonradiative recombination, which in turn deteriorate the solar cell performance and

stability. Therefore, the control on the ion migration and nonradiative recombination leads to the mitigation of hysteresis, finally contributing to both accurate performance evaluation and the long-term device operation.

2.1.3 Stability

Considering that high efficiencies have been recorded in both n-i-p and p-i-n PSCs, the concern on the long-term instability become the most challenging issue in front of the commercialization of PSCs. The factors affecting the device stability can be divided into two general categories: avoidable and unavoidable, which judges if the factors can be mitigated by effective encapsulation or protective environment under operation conditions. The avoidable factors include oxygen and moisture, whose interactions with solar cells can be prohibited assuming perfect encapsulation is applied. In fact, the encapsulation can also prohibit the escape of volatile species within PSCs. In contrast, some factors e.g. light, temperature and electrical bias are usually regarded as unavoidable as they exist with device operation and are hardly prevented using encapsulation. These factors are believed to associated with ion migration discussed above and still able to deteriorate the device performance with full encapsulation. Here the 'encapsulation' refers to the protection of solar cells using impermeable materials. The common encapsulation method in labs uses a piece of glass covering the cell which is sealed by epoxy resin. More information on encapsulation of PSCs is referred to Ref.[111,112]. In this thesis, Yb_2O_3 as a buffer layer will be introduced to alleviate ion migration and improve the device stability in **Chapter 5**.

2.1.4 Wide bandgap (WBG) PSCs

The rapidly growing demand on clean energy and consequently fast development of PV industry appeals for higher solar-electricity PCE. The maximum achievable PCE of typical single junction solar cells is calculated theoretically by the Shockley-Queisser limit.[6] Under a standard AM 1.5 solar spectrum illumination, a solar cell using an ideal bandgap, i.e. around 1.4 eV, absorber can give a PCE of 33.7% at most. As the major loss comes from the insufficient absorption of the broad solar spectrum using a single absorber, the multijunction (tandem) solar cells (TSCs) integrating two or more absorbers (subcells) with complementary absorption ranges become increasingly attractive for surpassing the SQ limit. Moreover, perovskite bandgap can be easily tuned from 1.2 to 2.4 eV through composition engineering. Also, the WBG PSCs with >1.7 eV perovskite can still achieve high PCE >20%,[113,114] which makes perovskite quite competitive in fabricating TSCs compared with other WBG materials. The WBG perovskite subcells in TSCs are expected to absorb the photons with high energy. To maximize the incident light absorption in TSCs, bandgap matching between WBG and NBG subcells are necessary, which will be further discussed in Section 2.3. Generally, the interested WBG perovskites are in the range of 1.7-1.8 eV as they are perfectly paired with mature NBG subcells around 1.1-1.3 eV e.g. silicon, OSC and CIGS. The development milestone of WBG PSCs with around 1.75 eV bandgap are given in the **Table 2.3**.

Table 2.3 Milestone of progress for WBG PSCs (E_g around 1.75 eV).

Year	Type	Perovskite	E_g (eV)	PCE (%)	V_{OC} (V)	J_{SC} (mA cm^{-2})	FF	Voc loss (V)	Ref.
2013		$MAPb(I_xBr_{1-x})_3$							115
2014		$FAPbI_yBr_{3-y}$							116

2014	p-i-n	$MAPb(I_{0.8}Br_{0.2})_3$	1.72	13.1	1.02	17.5	0.74	0.70	[117]
2016	p-i-n	$MAPbBr_{0.5}I_{2.5}$	1.75	14.9	1.21	15.8	0.78	0.54	[118]
2016	n-i-p	MAPbI2.1Br0.9	1.75	12.7	1.01	18.2	0.69	0.74	[119]
2016	p-i-n	MAPb0.75Sn0.25(I0.4Br0.6)3	1.73	12.6	1.04	15.5	0.78	0.73	[120]
2016	n-i-p	FA0.83Cs0.17Pb(I0.6Br0.4)3	1.74	17.1	1.2	19.4	0.75	0.51	[121]
2017	p-i-n	$MA_{0.6}FA_{0.4}Pb(I_{0.6}Br_{0.4})_3$	1.75	14.7	1.17	16	0.79	0.58	[122]
2018	p-i-n	FA0.6Cs0.4Pb(I0.7Br0.3)3	1.75	16.3	1.17	17.5	0.80	0.58	[123]
2019	p-i-n	FA0.8Cs0.2Pb(I0.6Br0.4)3	1.77	16.5	1.22	17.0	0.80	0.55	[124]
2019	p-i-n	FA0.8Cs0.2Pb(I0.7Br0.3)3	1.75	18.2	1.24	17.9	0.82	0.51	[125]
2020	p-i-n	FA0.6Cs0.4Pb(I0.65Br0.35)3	1.78	16.0	1.23	16.5	0.79	0.55	[126]
2022	p-i-n	FA0.75Cs0.25Pb(I0.6Br0.4)3	1.79	17.8	1.26	17.9	0.79	0.53	[127]
2022	p-i-n	FA0.8Cs0.2Pb(I0.7Br0.3)3	1.75	18.6	1.26	18.6	0.79	0.49	[128]
2022	p-i-n	DMA0.1Cs0.4FA0.5Cl0.05	1.80	17.7	1.26	17.4	0.80	0.54	[129]
2022	p-i-n	FA0.8Cs0.2Pb(I0.62Br0.38)3	1.76	17.3	1.22	17.4	0.82	0.54	[130]
2022	p-i-n	DMA0.1Cs0.3FA0.6Pb(I0.7Br0.3)3	1.75	20.3	1.32	18.7	0.82	0.43	[114]
2022	p-i-n	FA0.8Cs0.2Pb(I0.6Br0.4)3	1.79	20.2	1.33	18.1	0.84	0.46	[113]
2023	p-i-n	FA0.8Cs0.2Pb(I0.62Br0.38)3	1.78	18.6	1.27	17.7	0.83	0.51	[131]
2023	p-i-n	FA0.8Cs0.2Pb(I0.6Br0.4)3	1.77	18.5	1.31	17.8	0.79	0.46	[132]

To increase the bandgap to the interested range (1.7~1.8 eV) from the prototype $MAPbI_3$ (~1.57 eV), the most straightforward way is to increase the Br/I ratio. Starting from the common $MAPbI_{1-x}Br_x$, Hoke et al. observed distinct halide segregation induced by light soaking, forming iodine-rich domains with lower bandgap and bromide-rich domains with higher bandgap, respectively.[133] Therefore the phase segregation results in "unstable" bandgap and limits the attainable Voc. In addition, MA-based perovskites suffer from inherent thermal instability above 85 °C, making it difficult to operate as commercial PV products.[134]

Beyond MA-based perovskite, FA-based perovskite is more thermally stable, which is therefore more attractive for vulnerable WBG perovskite.[135–140] Limited by the Br/I phase, the WBG PSCs' progress far lags behind the mid-bandgap (MBG) perovskites. The breakthrough was made by Snaith group in 2016 when Cs was introduced to partially substitute FA in A-site.[121] Regarding the mixed-halide phase segregation which is widely observed in the single-cation perovskite e.g. $MAPb(I_{0.6}Br_{0.4})_3$ and $FAPb(I_{0.6}Br_{0.4})_3$, $FA_{0.83}Cs_{0.17}Pb(I_{0.6}Br_{0.4})_3$ demonstrates better resistance to the photoinduced halide segregation under identical light illumination. Also, the incorporation of Cs greatly reduces the Urbach energy to 16.4 meV in contrast to ~50 meV of other single-cation mixed-halide perovskites, implying suppressed electronic disorder. Finally, the champion cell delivers a Jsc of 19.4 mA cm^{-2}, a Voc of 1.2 V, and a PCE of 17.1%.

Although FA-Cs system become predominant in WBG PSCs, the Voc loss and vulnerable stability are still two main challenges. The former one refers to the phenomenon that the Voc does not go up with bandgap as expected, which is also known as Voc deficit (Voc loss = bandgap – qVoc, where q is the elementary charge) that limits the overall WBG device performance. In additional to halide segregation with low bandgap domains mentioned above, substantial nonradiative recombination is also believed to be the main source of voltage loss. Therefore, optimization strategies from either additives engineering or surface/interface engineering are emerged to address the issues. Generally, main functions of additives include improving perovskite crystallinity and film morphology, mitigating phase segregation, passivating traps. For example, lead thiocyanate $Pb(SCN)_2$ added in FA-Cs perovskite precursor has been

proved to improve crystallinity and grain size, possibly due to the CH_3NH_2 gas formed by $Pb(SCN)_2$.[141] Together with excess formamidine halides, $Pb(SCN)_2$ can further provide synergistic effects of reducing impurities and passivating grain boundaries.[142] Similarly, the incorporation of alkali cations e.g. K^+ can also decorate grain boundaries rather than being doped into the lattices, effectively suppressing ion migration and nonradiative recombination.[143] In addition, highly polar formamide is utilized to improve the solubilization of Cs^+ salt and mitigate uncontrollable precipitation and finally reduce the non-active phases and defects.[144] Surface treatment represents another strategy that can mitigate the nonradiative recombination pathway, form low-dimension perovskite and improve the band alignment. A few types of ammonium molecules have been successfully applied as surface passivators including guanidinium (GA),[44] phenethylammonium (PEAI)[145], and butylammonium[146]. For instance, benzylamine (BA) post-treatment was found to effectively passivate perovskite surface, block ion migration and suppress phase segregation by forming 2D perovskite atop the bulk perovskite. [147] The effect of surface treatment can also be achieved through tuning the surface electronic properties. GABr treatment was found to increase the surface work function by 280 meV through formation of graded surface structure, greatly improving energy level matching.[125] Benefiting from the reduced nonradiative recombination, the champion WBG PSC passivated by (butyl-)ammonium treatment can generate a remarkable PCE of 19.4% and a high Voc of 1.31 V (i.e. Voc deficit=0.41 V), exceeding 90% of the SQ limit. Apart from ammonium treatment, electron-donating ligand TOPO[148] and atomic layer deposition grown Al_2O_3[149] have also been demonstrated their effectiveness in surface passivation and Voc enhancement.

Another challenge for WBG PSCs is instability. Virtually, WBG perovskites share most

of degradation factors with other perovskites such as moisture, light illumination, oxygen, high temperature. Furthermore, WBG PSCs also suffer from issues attributed to mixed halides which is necessary in widening the bandgap. For state of the art WBG PSCs (**Table 2.3**), mixed cations (FA-(MA)-Cs) and mixed halides (I-Br) are widely used, implying the phase segregation being the risk for device stability. Beyond the unstable phases discussed above[133], halide phase segregation was also observed even in dark and inert environment.[150] This indicates that the mixed halide perovskite may sit in a metastable phase that tend to segregate spontaneously, and this process can be accelerated by light illumination to provide energy for ion migration over energy barriers, which was supported by multiscale modelling and nanoscale imaging.[28] Although studies prove that demixing regions can be back to remixing on heating/photoheating or simply placing in the dark, the mobile ions may likely be trapped at surface, grain boundaries or even diffuse into adjacent layers, giving rise to the irreversible process.[151] In addition, the widened bandgap via band levels shifted upward/downward lead to the energetically mismatch interfaces with common transporting layers used for mid-gap perovskites, resulting in the accumulation of charges at the interfaces and stresses the imporatnace of redesigning transporting layers specifically for WBG perovskites.[152]

2.2 Organic solar cells (OSCs)

2.2.1 Development of OSCs: from fullerene to NFA

OSCs are composed of organic semiconductors as light harvesters, sandwiched by charge transporting layers and electrodes. The development of OSCs has gone through a long process dated back to 1959,[153] where the early OSCs only have low efficiency below 0.1%, which was then attributed to the undissociated free charge carriers. Due to

the weak intermolecular forces and low dielectric constants (typically 2-4), organic materials have difficulties in dissociating the Coulombically bound electron-hole pair, or an exciton, into free one electron and one hole. In contrast to the small exciton binding energy (E_b) in inorganic semiconductors (E_b ~ 15 meV for silicon) that can be easily overcome by thermal energy (25.85 meV at 300K), organic semiconductors have much large E_b (e.g. 0.7 eV).[154] The electric field provided by the difference of work functions of electrodes is also insufficient for exciton dissociation. Moreover, the exciton usually has a short diffusion length below 10 nm which is much smaller than the thickness of absorber layer (>100 nm), making it further difficult to extract charge carriers before their recombination. Therefore effective dissociation of excitons limits the development of early OSCs.

The breakthrough came with the first efficient OSC reported by C. W. Tang in 1986.[155] Tang proposed the seminal concept of donor-acceptor heterojunction (D-A) which becomes the heart of OSC development in the past several decades. The idea is to make use of energy offset between electron affinities (EA, and/or ionization potentials, IP) two organic materials to overcome the exciton binding energy. The material with higher EA will accept dissociated electrons, known as the acceptor, while the material with lower IP will accept dissociated holes, known as the donor. The D-A heterojunction was firstly made planar via vacuum deposition which was then improved to the solution-processed bulk heterojunction (BHJ) by Alan Heeger *et al*. in 1995 for shortening the exciton diffusion and facilitating exciton dissociation via more D-A interfaces.[156] By adopting BHJ, it allows for thick absorber films used for more light absorption.

As shown in the **Fig. 2.7,** in the early stage, efficient OSCs are based on the BHJ blend

of P3HT:PCBM and efficiency is generally enhanced via morphology improvement. Afterwards, numerous donor materials have been designed e.g. PCDTBT, PBDB-T, PTB7-Th, which help the PCE break the 10% threshold. Although donor and acceptor materials are both important in BHJ, the acceptors have attracted much less attentions than donors for a long time. In this period, fullerene-based acceptors dominated the choice of acceptors due to the favourable features such as suitable electron affinity, high electron mobility and ability to form interpenetrating networks with donors. The PCE of 12.1% was recorded in 2017, marking the ceiling of fullerene-based OSCs.[157] However fullerenes' weak absorption in visible and near infrared (NIR) regions makes it difficult to step further. Also it suffers from poor thermal stability and photochemical stability as well as the need for time-consuming purification, rendering it nonideal acceptor in the long run.

The scenario has been changed by the highly efficient non-fullerene acceptors (NFA) which then bring OSCs into a new era since 2010s. In fact, NFA has a long story of development since 1986 when vacuum deposition dominates the fabrication of planar bi-layered OSCs. The representative examples include PDI derivative and SubPc. The invention of solution-processed BHJ made the fullerene-based acceptors stand out because of their good compatibility with a large range of donors. In contrast, NFA in this stage are in 2D planar form that shows strong aggregation and consequently poor morphology.[158] Thus the PCE of NFA-based OSCs are merely in the range of 2-3%. Focusing on suppressing the excessive aggregation, the studies began to make the NFA from 2D to 3D as the fullerene derivatives. This is achieved by either twisting the backbone or introducing bulky out-of-plane side chains. In 2015, Zhan et al. designed the A-D-A type fused-ring electron acceptor (FREA) ITIC which became a milestone.

In the A-D-A structure, the intramolecular push-pull effect is realized via an electron-donating conjugated backbone core along with electron-withdrawing end units, ensuring strong electron accepting properties.[159] Also, the fused core unit has 4 bulky side chains, giving rise to the increased solubility and suppressed aggregation. The end units are in the π-π stacking, rendering the efficient electron transport. Due to the A-D-A molecular structure, the strong electron intramolecular push-pull effect leads to a narrow bandgap with strong absorption in 500-800 nm, leading to the overall PCE of 6.8%. One year later, Zhan group reported another A-D-A molecule IDIC delivering an impressive PCE of 11% which is comparable with the best fullerene-based OSCs. Learning from the success of these A-D-A NFA, the research community understands the relations between the key structural elements, e.g. the core unit, the end unit and the side chain, and the material properties, e.g. energy levels, solubility, crystallinity and carrier mobility. Following the strategy of molecular engineering of A-D-A structure, the OSCs enter the booming time soon. Many efficient NFA are designed such as ITIC-Th1, IT-4F, COi8DFIC, SN6IC-4F, among which the emergence of Y6 and its derivatives became the landmark of latest OSC development. In 2019 Zou et al. reported Y6 for the first time, which delivered a tremendous PCE of 15.7%.[160] Compared with traditional A-D-A NFA, Y6 possesses higher degree of conformational rigidity and uniformity, giving rise to rather unique packed 3D network for efficient electron transport and exciton delocalization.[161] The suppressed tail state energetic disorder also contributes into the impressive small energy loss.[162] The invention of Y6 opened the new avenue of efficient OSCs and considerable efforts have been put into the molecular engineering of NFA. Star NFA after Y6 include BTP-ec9, L8-BO and BS3TFe-4F. These molecules own ultranarrow bandgap ~1.2 eV, outstanding absorption in visible and NIR region, ordered packing for electron transport and

excellent solubility and miscibility with many donors. All these features contribute to the high PCE of OSCs around 19% reported in recent years.[163–165] Some representative milestones of the progress for the OSCs have been listed in the **Table 2.4**.

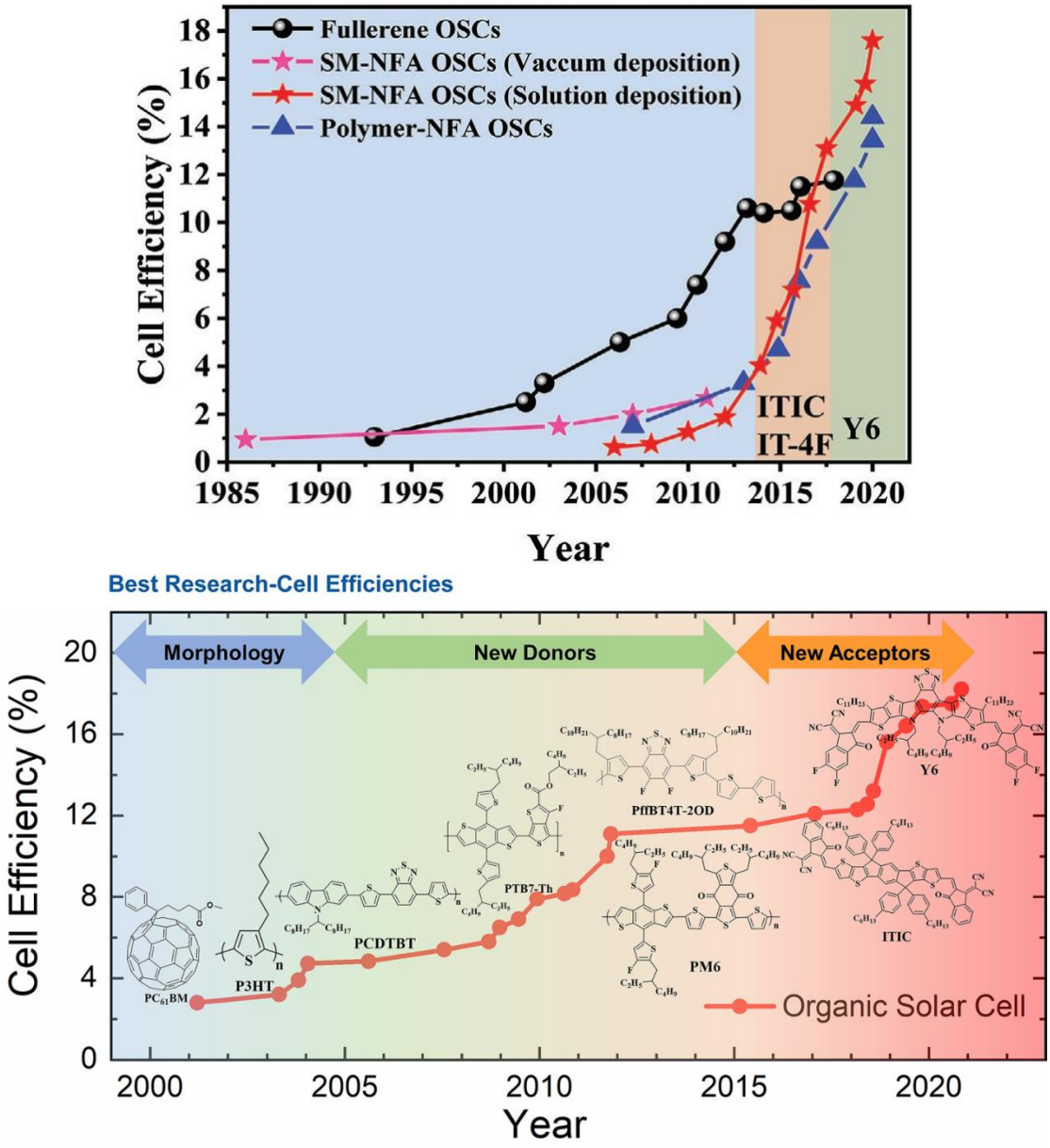


Fig. 2.7 The efficiency evolution of OSCs.
Top: fullerene OSCs vs NFA OSCs. Bottom: Main factors trigger the OSC development. Reproduced with permission from Ref.[342] Copyright © 2022 American Chemical Society and Ref.[177] Copyright © 2021 Wiley-VCH GmbH

Table 2.4 Milestone of progress for OSCs.

Year	Organic absorber	PCE (%)	V_{OC} (V)	J_{SC} (mA cm^{-2})	FF	Ref.
1986	Copper phthalocyanines : perylene derivative	1			0.65	155
1995	MEH-PPV : PCBM	2.9				156
2001	MDMO-PPV : C60	4.3				166
2005	P3HT : PCBM	4.4	0.61	10.6	0.674	167
2010	PTB7 : PCBM	7.4	0.74	14.5	0.69	168
2012	PTB7 : PCBM	9.2	0.754	17.46	0.700	169
2013	PTB7-Th : PCBM	9.35	0.80	15.73	0.743	170
2016	PffBT4T-C9C13 : PC71BM	11.7	0.784	19.8	0.73	171
2017	PTB7-Th : DR3TSBDT : PCBM	12.1	0.77	23.3	0.704	157
2019	PM6 : Y6	15.7	0.83	25.3	0.748	160
2019	PM6 : Y7	17.0	0.858	25.6	0.776	172
2020	D18 : Y6	18.22	0.859	27.7	0.766	173
2021	PM6 : BTPeC9 : L8-BO-F2	18.66	0.853	27.35	0.80	174
2022	D18 : BS3TSe-4F : Y6-O	19.03	0.845	29.41	0.796	175
2023	D18-Cl : PM6 : L8-BO : BTP-eC9	19.61	0.898	27.02	0.808	176

2.2.2 Working principles of NFA-OSC

The emergence of NFA in high-performance OSC makes it interesting to answer the following questions: what is so special about these NFA and how do they really work? Although the device physics to explain the success of NFA has yet fully understood, it is obvious that the principle of NFA greatly challenges the existing wisdom based on fullerene-based OSC. This section will briefly introduce some conjectures proposed and interested readers are referred to Ref.[177,178] for more information.

In a simplified picture, one incident photons absorbed promote an electron from the

highest occupied molecular orbits (HOMO) to the lowest unoccupied molecular orbits (LUMO), leaving a hole behind. Such an electron-hole pair is Coulombically bound, which is known as an exciton or a photoexcited singlet state (S_1). In inorganic semiconductors with high dielectric constants (usually > 10), the exciton is highly delocalized with a large radius, in which the Coulomb attraction (aka exciton binding energy) can be easily overcome by thermal energy. However the situation is much more challenging in organic semiconductors due to the low dielectric constants of 2~4 in general, giving rise to the more localized nature of the photoexcited states i.e. a more tightly bound exciton. The typical binding energy in organic semiconductors is 0.3~0.7 eV, which is much larger than the thermal energy (~25 meV) at room temperature.[179,180] Therefore it requires the external driving force to overcome the binding energy and dissociate excitons into free charge carriers collectable. This brings the invention of BHJ. The practical device using BHJ works well which commonly requires an energy offset > 0.3 eV as driving force for dissociating excitons by empirical rules. However, the theory on the exciton dissociation process is far lag behind. Historically, it is believed that the dissociation of excitons into free charge carriers is not straightforward but going through a medium so-called charge-transfer state (CTS), described by Marcus theory and Onsager−Braun theory.[181] In this framework, the exciton migrates to the D-A interface and firstly transit to a CTS. Afterwards the CTS can go through two competing processes, either further split into free charge carriers or directly decay to the ground state via geminate recombination. The difference between the energy of exciton (S_1) and CTS (E_{CT}) is regarded as the driving force for this transition, which is provided by the energy offset between EA (IP). It is traditionally believed that the larger the offset, the stronger the driving force. This plausible statement is concluded based on the fullerene-based OSC and dominates the understanding of device physics and

design for BHJ for a long time (**Fig. 2.8**). Unfortunately the energy offset 'necessary' in fullerene-based OSC also contributes into the voltage loss, as shown in **Fig. 2.9**. The champion-performing fullerene-based OSC with PCE >10% generally exhibit a low Voc of 0.8 V along with a large voltage loss > 0.8 V.[182,183] The dilemma effects of energy offset, 1) needed for efficient charge generation, and 2) causes considerable voltage loss, incurs the trade-off between high Jsc and high Voc in fullerene-based OSC, limiting the advances of PCE.

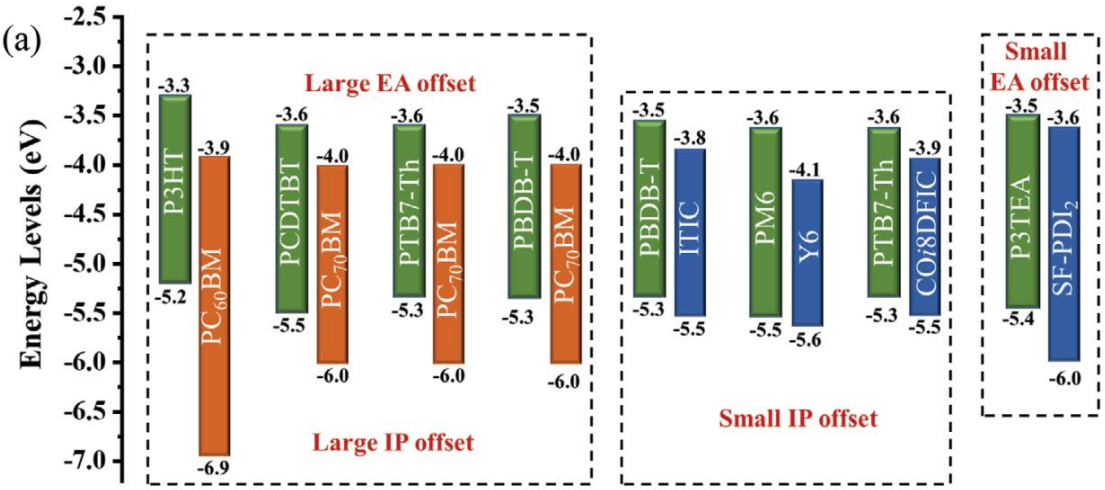


Fig. 2.8 Energy offsets in typical organic blend.
EA=electron affinity. IP=ionization potential. Reproduced with permission from Ref.[343] Copyright © 2020 WILEY-VCH Verlag GmbH & Co. KGaA, Weinheim

Compared with the fullerene-based OSC, the most impressive fact of NFA is that it can maintain a high IQE over 90% (internal quantum efficiency, used as the efficiency indicator of converting absorbed photons into collectable carriers) when the driving force is modest (<0.1 eV), rendering the NFA-based OSC with both high Jsc and high Voc simultaneously, which is now well accepted as the key of NFA success.[184–187] This greatly shocks the established working principle of OSC and raises again the doubt on the exciton-CTS-carriers process. Suffice to say that it will be more challenging to

figure out this process in NFA-based BHJ since both donors and NFA contribute intensively to the light absorption, thereby both electron and hole transfer processes (channel 1 and channel 2) are significant, in contrary to the fullerene-based BHJ where only the donors are highly absorptive.

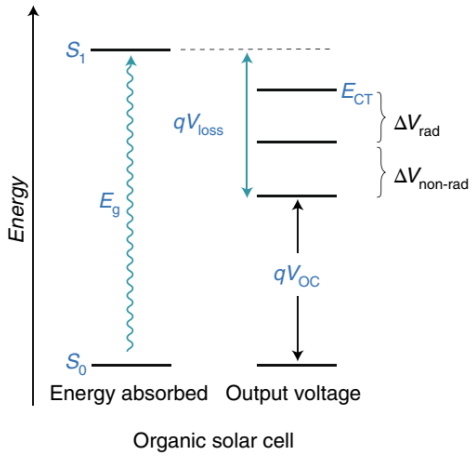


Fig. 2.9 Schematics of bandgap, Voc, and voltage loss in OSCs.
S_0: ground state. S_1:excited state. E_{CT}:charge transfer state. q:elementary charge. ΔV_{rad}:radiative recombination loss. $\Delta V_{non\text{-}rad}$:non-radiative recombination loss. E_g: bandgap. V_{loss}: voltage loss.
Reproduced with permission from Ref.[158] Copyright © 2018, The Author(s)

It is noted that the small offset does not necessarily guarantee the small voltage loss. In addition to the driving force, the voltage loss also comprises the contribution of radiative (absorption above/below the bandgap) and nonradiative recombination, as shown in **Fig. 2.9**. The radiative contribution from above-bandgap absorption comes from the mismatch between radiation received in a narrow solid angle from the sun, which counts 0.25 eV and is unavoidable for all types of solar cells.[188] The below-bandgap absorption depends on the energetic disorder and tail states, which is smaller for crystalline inorganics and perovskite while larger for organics.[189] For the nonradiative recombination term, typical fullerene-based OSC show large values >0.3 eV.[190] Since the contribution from the driving force can be decreased using NFA, it is therefore important to understand and minimize the non-radiative term beyond the

driving force for further minimizing the voltage loss. Currently the origin of the reduced non-radiative loss in NFA is still a subject for debating. The triplet exciton formation has now been believed to highly relate to the primary nonradiative recombination and major loss channel.[191–193] It is shown that the sidechain engineering has negligible effect on the charge transfer state while can effectively inhibit the NFA triplet exciton formation. In the fullerene-based absorbers, the small energy difference and strong electronic couplings between the charge transfer state and the lowest-lying triplet exciton state of fullerene acceptor molecules make the spin-triplet recombiatnion much easier to occur. In contrast, NFA blends provide larger energy difference and weaker couplings between these states that strongly retards the relaxation rate to the triplet exciton state, giving rise to the suppression of triplet recombination and thus more efficient charge generation. Guided by these findings, NFA-based OSCs have the potentials to advance further rather than merely "copy and paste" the fullerene's route in the past.

2.3 Perovskite-based tandem solar cells (TSCs)

2.3.1 The concepts

Nowadays, the PCE of single-junction solar cells are quite approaching their theoretical performance ceiling of ~33% PCE based on detailed balance calculation.[6] There are mainly five types of energy loss channels as shown in **Fig. 2.10**:

1) Emission loss. Kirchhoff's law of thermal radiation.
2) Carnot loss. A heat engine operation between the heat source of 5800 K and a solar cell of 300 K
3) Boltzmann loss. Entropy generated when consider the angular inequity of

absorption and emission.

4) Thermalization loss. The heat dissipated during hot carriers cooling after absorbing hv > Eg photons.

5) In-band loss. The coming hv < Eg photons pass through the solar cell.

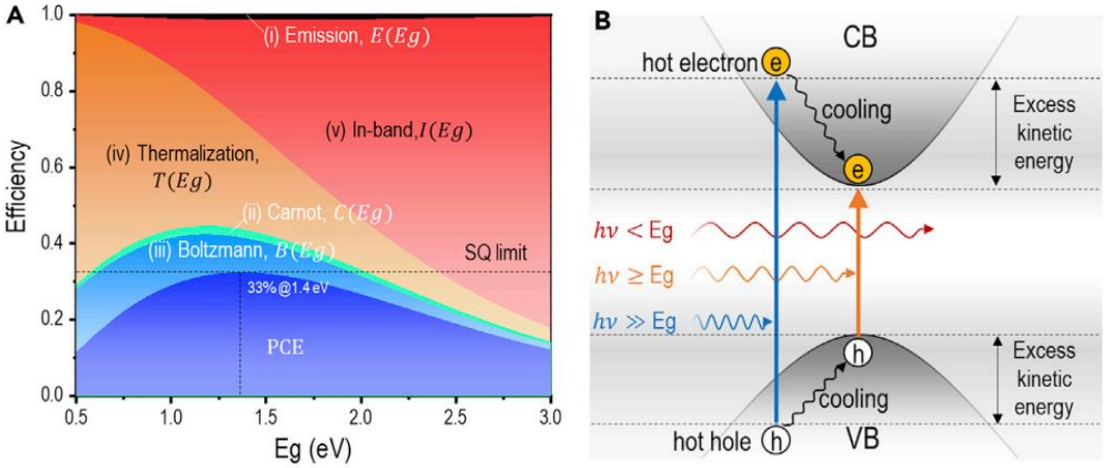


Fig. 2.10 Schematics of energy losses in solar cells.
(a) Intrinsic energy losses in an ideal single-junction solar cell. (b) Relationship between bandgap and incident photon energies. Reproduced with permission from Ref. [344] Copyright © 2022 Elsevier Inc.

It is clearly that thermalization and in-band losses constitute most of the total unabsorbed light energy. To reduce these two losses, photons with higher and lower energy are to be utilized. Therefore, several absorber films with complementary absorption ranges can be stacked to fabricate the multijunction i.e. tandem solar cells (TSCs). In one TSC, the front cell with a larger bandgap absorbs the high-energy photons, while the low-energy photons are captured by the smaller bandgap rear cell. By mitigating the losses of carrier thermalization, the TSCs can deliver an efficiency higher than either a single front or rear cell itself. Based on theoretical estimation, the ceiling PCE of two-junction TSCs could surpass 40%,[194] and the ultimate efficiency achievable is 68% when infinite absorbers are stacked (with no light concentration). In reality, a TSC with two absorbers is more cost-effective and sufficient for most of the

practical needs, therefore TSCs refer to two-junction solar cells specifically in this thesis.

The two absorbers of one TSC are commonly stacked either with a monolithic two-terminal configuration (2T) or stacked mechanically with a four-terminal configuration (4T). In the 2T configuration, two subcells are connected in series by an ICL within one monolithic device. For the 4T configuration, the WBG subcell is only mechanically placed in front of the NBG subcell, while both subcells have their own circuits and are electrically separated. Although the 4T configuration does not require the current matching between two subcells, this design increases fabrication process and cost, which is less attracting for the industry. Over the past few years, the p-i-n PSC showing advantages of low-temperature processing, low parasitic absorption, and excellent operational stability has become a popular choice as the subcell for the construction of TSCs and achieved remarkable success.

Fig. 2.11 shows the efficiency evolution of three main types of 2T TSCs based on p-i-n PSCs, including perovskite-Si TSCs, all-perovskite TSCs and perovskite-organic TSCs (POTSCs). In this section, the development of all the three types will be reviewed, with a focus on fabrication protocols and the design of ICL. And then the perspectives of three different TSC routes are also discussed. While this thesis focuses on the 2T configured POTSCs, it is noted that three types of perovskite-based TSCs share lots of similarities among each other e.g. design of interconnecting layers, optimization of WBG perovskite. Moreover, perovskite-Si and all-perovskite TSCs are two fast-growing regions with much more published studies, implying that there are a lot of lessons for POTSCs to learn and develop. Therefore discussion will be firstly started

with the perovskite-Si and all perovskite TSCs before discussing the POTSCs.

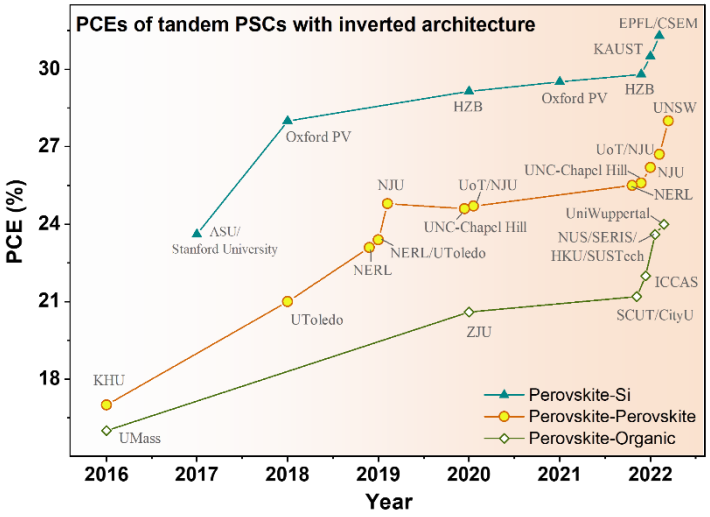


Fig. 2.11 Evolution of three types of p-i-n perovskite-based TSCs

2.3.2 Main types of perovskite-based TSCs

2T Perovskite-Si TSCs

With the fast development in the past several decades, silicon solar cells become the most mature photovoltaic technology and dominate the commercial photovoltaic market, which probably will last for another ten years or more. Since the champion PCE of silicon solar cells reaches 26.81%,[195] efficiency enhancement in silicon solar cells becomes very difficult with a small marginal benefit against vast research investment. Therefore, the low-cost perovskite materials with tunable bandgap attracted communities' attention to fabricating perovskite-Si TSCs. The first perovskite-Si TSC was reported by Mailoa et al. in 2015.[196] Although the first perovskite-Si TSC delivered a moderate PCE of 13.7%, this seminal work demonstrates that the design of perovskite-Si TSC is feasible and the perovskite subcell is the efficiency-limiting part for further improvement. In the early years, most of the perovskite-Si TSCs[197–200] employed the n-i-p configuration due to the superior efficiency of n-i-p PSCs against

their p-i-n counterparts. However, these n-i-p devices employed the spiro-OMeTAD as the HTL, which introduced issues of material instability[201,202] and low J_{SC}[203] due to its strong parasitic absorption in the short wavelength range. Owing to these issues of n-i-p structures and the raising of p-i-n PSCs, the perovskite-Si TSCs with p-i-n architecture attract growing attention. To this end, McGehee's group et al. adopted the p-i-n structure in perovskite-Si TSCs for the first time in 2017. To tackle the low J_{SC} of n-i-p TSCs, this work used a functional bilayer consisting of SnO_2 and zinc tin oxide (ZTO) as the buffer layer enabling the sputtering of the transparent ITO electrode. Through this design, parasitic absorption of window layers (i.e. layers that light passes through first before entering perovskite films) was minimized. Also, the bilayer was deposited by either atomic layer deposition (ALD) or pulsed chemical vapor deposition (CVD) that guaranteed a compact, conformal and pinhole-free film, preventing shunt and damp heat damage. For the WBG absorber, the recently developed perovskite with the composition of $Cs_{0.17}FA_{0.83}Pb(Br_{0.17}I_{0.83})_3$ was used due to its more complementary bandgap and much enhanced thermal stability compared with previous $MAPbI_3$. By integrating an infrared-tuned silicon heterojunction bottom cell (SHJ), this work lifted the J_{SC} to 18.1 mA cm^{-2} and achieved a record efficiency of 23.6% at that time.[204]

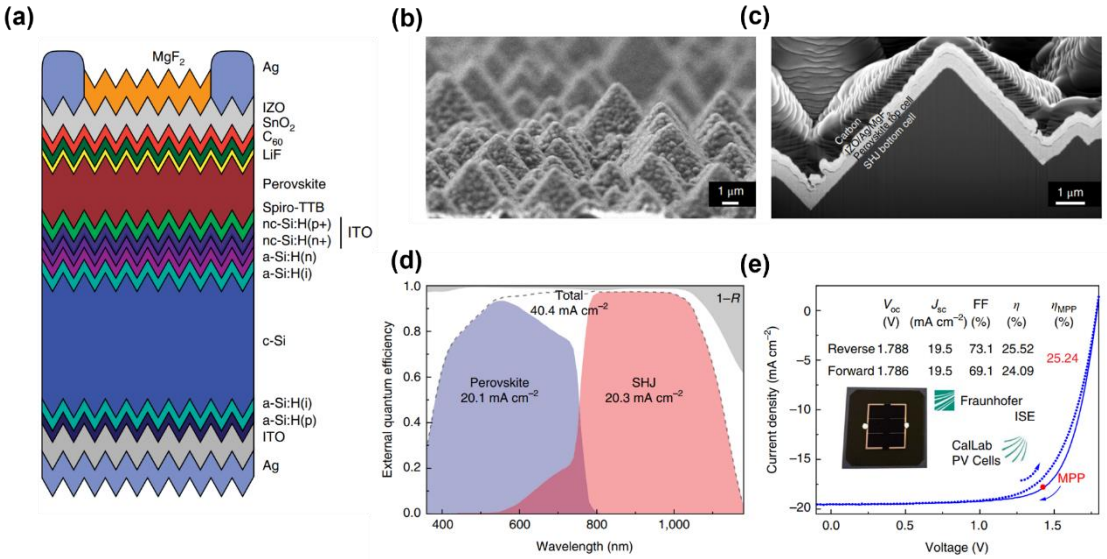


Fig. 2.12 Schematics of a state-of-the-art perovskite-Si TSC.
(a) Schematic of a fully textured monolithic perovskite/SHJ TSC. (b) Top-view SEM images of the perovskite film. (c) Cross-sectional SEM images of the full perovskite top cell prepared on the SHJ bottom cell. (d) EQE spectra and total absorptance (1–R, where R is the reflectance) of the champion TSC. (e) Certified *J–V* curves of the champion device under reverse and forward scans with a scan rate of 100 mV s^{-1}. Reproduced with permission from Ref.[205]. Copyright 2018 Springer Nature.

The efficient fabrication route for perovskite films atop Si substrate is another challenge. In previous works, the front sides of silicon cells were usually polished to be compatible with the crystallization features of perovskite precursor solutions. This inevitably leads to high reflection, low light trapping and increased manufacturing costs. To solve this problem, Ballif's group et al.[205] proposed a hybrid "evaporation + solution" (eva + sol) route to fabricate the perovskite films directly atop silicon pyramidal surfaces (**Fig. 2.12a-c**). In brief, the PbI_2 and CsBr were co-evaporated firstly, followed by the spin-coating of the FAI/FABr mixture, through which the perovskite films can maintain good conformal growth on the micrometer-sized silicon textured surfaces. Since as-fabricated TSCs made full use of the light management in silicon cells, a high J_{SC} of 19.5 mA cm^{-2} and a record PCE of 25.5% were yielded (**Fig. 2.12d,e**).

Later, Sargent et al.[206] and Huang et al.[207] successfully demonstrated that perovskite

films could be solution-processed directly atop non-polished silicon pyramidal surfaces using either spin-coating or blading techniques, and achieved the PCE of 25.7% and 26.2% respectively. Inspired by the idea of making use of the texture, Becker's group et al.[208] reported a gentle designed nanotextured surface recently. This nanotexture distinctly reduced the reflection loss while enabling excellent perovskite film formation. This design integrated the advantages of both polished surfaces and micrometer-sized textured surfaces, and was responsible for minimizing J_{SC} loss and increasing V_{OC} respectively, finally leading to the PCE of 29.80% certified. These indicate that the fabrication of perovskite films on textured substrates is no longer the most challenging factor.

The optimization of perovskite-Si TSCs architectures motivates increasing attention to another performance-limiting factor i.e. the WBG perovskite subcells. To optically complementary with the silicon subcell, a WBG perovskite with 1.67-1.75 eV is desired.[209] Finely tuning perovskite bandgaps through compositional engineering without introducing stability issues is challenging. Instead of engineering the cation components, Kim et al.[210] developed a 2D-3D mixed perovskite (1.68 eV) using an anion mixture of thiocyanate (SCN) with iodine. Through careful anion engineering, optimal WBG perovskite treated by PEA($I_{0.25}SCN_{0.75}$) produced a PCE of 20.7% with a V_{OC} larger than 1.2 eV. Also, passivated by the 2D phase, as-prepared perovskite single cells can retain 80% of initial PCE after more than 1000 h continuous illumination. Based on this treatment, the champion perovskite-Si TSC achieved 26.7% PCE with a J_{SC} of 19.2 mA cm^{-2}, a V_{OC} of 1.756 V, and a FF of 0.792 with negligible hysteresis. In the meantime, Xu et al.[211] extended the traditional WBG perovskite double-halide composition using I and Br into a triple-halide composition including Cl.

Thanks to the ability of Cl to reduce defect density, the triple-halide WBG perovskite observed much enhancement in photocarrier lifetime and mobility by a factor of 2. The incorporation of Cl also suppressed the light-induced phase segregation at 100-sun illumination, ensuring long-term operational stability. By combining these WBG perovskites with silicon subcells, a PCE of 27.1% (steady-state PCE at maximum power point of 27.04%) was obtained. In addition to the bulk perovskite materials, there are also massive imperfections existed at both surfaces/interfaces of perovskite films, rendering severe local non-radiative recombination and poor charge carrier extraction.[212] Using a kind of self-assembled, methyl-substituted carbazole monolayer (Me-4PACz) as the HTL, Albrecht's group[213] successfully minimized the non-radiative recombination while keeping efficient hole extraction simultaneously and a high FF of 84% was obtained in the single WBG perovskite cell. By incorporating it with the silicon subcells, a high PCE of 29.15% with an FF of 79.4% was achieved. Notably, Me-4PACz also provided excellent stability that 95.5% of initial PCE was retained after 300 h operation under illumination. Recently, the same group further lifeted the PCE certified record to 32.5% by further minimizing voltage loss to 0.4 V and thereby obtaining a high Voc of 1.28 V in the 1.68 eV perovskite subcell. [214]

The representative state-of-the-art perovskite-Si TSCs are summarized in **Table 2.5**. To further increase the performance, there are several points to consider:

1) efficient WBG perovskite with smaller voltage losses. The solutions could be e.g. effective passivation of bulk and surface defects, fine bandgap tune strategies, powerful and stable charge carrier extraction materials.
2) designed silicon textured surfaces for the 'trade-off' requirements of reducing reflection and growing high-quality perovskite films.

3) novel transparent conductive electrode to minimize the parasitic absorption and maintain good conductivity.

Table 2.5 Summary of representative 2T perovskite-Si TSCs with p-i-n configuration. Values in the brackets are certified.

WBG/front cell	ICL	NBG /rear cell	Front/rear surface	V_{OC} (V)	J_{SC} (mA cm^{-2})	FF (%)	PCE (%)	Year	Ref.
$Cs_{0.05}(FA_{0.77}MA_{0.23})_{0.95}Pb(I_{0.77}Br_{0.23})_3$	IZO	SHJ	Polished/textured	1.98	20.24	81.18	(32.5)	2023	[214]
$Cs_{0.18}FA_{0.82}Pb(I,Br)_3$	ITO	SHJ	Textured	1.91	20.47	79.8	(31.25)	2023	[215]
$Cs_{0.05}FA_{0.8}MA_{0.15}Pb(I_{0.755}Br_{0.255})_3$	IZO	SHJ	Textured	1.92	19.7	80.7	30.5 (29.3)	2022	[216]
$Cs_{0.05}(FA_{0.77}MA_{0.23})_{0.95}Pb(I_{0.77}Br_{0.23})_3$	ITO	SHJ	Textured	1.90	19.45	80.9	29.8	2022	[208]
$Cs_{0.05}(FA_{0.77}MA_{0.23})_{0.95}Pb(I_{0.77}Br_{0.23})_3$	ITO	SHJ	Polished/textured	1.90	19.26	79.5	29.2[a]	2020	[213]
$Cs_{0.1}FA_{0.2}MA_{0.7}Pb(I_{0.85}Br_{0.15})_3$	ITO	SHJ	Textured	1.92	18.95	78.5	28.6	2022	[217]
		Topcon	Textured	1.8	19.2	81.8	28.2	2022	[218]
				1.80	19.8	78.7	28.0	2018	[219]
$(Cs_{0.22}FA_{0.78}Pb(Cl_{0.03}Br_{0.15}I_{0.85})_3$	ITO	Topcon	Polished/textured	1.79	19.68	78.3	27.6	2022	[220]
	Si:H(n+)/ Si:H(p+)	SHJ	Textured	1.81	19.78	76.9	27.5	2021	[221]
$Cs_{0.22}FA_{0.78}Pb(I_{0.85}Br_{0.15})_3$	ITO	SHJ	Polished/textured	1.86	19.23	76.2	27.3 (27.2)	2022	[222]
$FA_{0.78}Cs_{0.22}Pb(I_{0.85}Br_{0.15})_3$ + 3mol% $MAPbI_3$	ITO	SHJ	Polished/textured	1.89	19.1	75.3	27.1	2020	[211]
$(FA_{0.65}MA_{0.2}Cs_{0.15})Pb(I_{0.8}Br_{0.2})_3$	ITO	SHJ	Polished/textured	1.76	19.2	79.0	26.7 (26.2)	2020	[210]
$Cs_{0.1}MA_{0.9}Pb(I_{0.9}Br_{0.1})_3$	ITO	SHJ	Textured	1.82	19.2	75.3	26.2	2020	[207]
$Cs_{0.05}MA_{0.15}FA_{0.8}PbI_{2.25}Br_{0.75}$	InOx	SHJ	Textured	1.78	19.3	75.4	25.7[a]	2020	[206]
	SiCx(n) /Si:H(p+)	Topcon	Textured/polished	1.74	19.5	74.7	25.4	2019	[223]
		SHJ	Textured	1.79	19.5	79.1	25.2[a]	2018	[205]
$Cs_{0.17}FA_{0.83}Pb(Br_{0.17}I_{0.83})_3$	ITO	SHJ	Polished/textured	1.65	18.1	79.0	23.6	2017	[204]

2T All-Perovskite TSCs and ICLs

Due to the nature of tunable bandgaps, different perovskites with complementary absorption ranges can be combined to fabricate all-perovskite TSCs. Compared with other perovskite-based TSCs, all-perovskite TSCs can retain and make full use of the merits of perovskites e.g., high efficiency, low cost, solution-processability and good flexibility.

Although the early all-perovskite TSCs were designed with the n-i-p configuration,[224,225] most of the high-efficiency TSCs have been fabricated in the p-i-n geometry, mainly due to two reasons: 1) efficient NBG perovskite cells are mainly in p-i-n type to avoid the oxidation of Sn induced by the p-dopant e.g. lithium in the spiro-OMeTAD[226]; 2) p-i-n perovskite devices are catching up with the n-i-p counterparts.[227,228] Different from perovskite-Si TSCs where the NBG silicon absorber has the fixed bandgap of ~1.1 eV, the compositions and bandgaps of WBG and NBG absorbers in all-perovskites TSCs can be engineered to cater to each other, which provides a wide range of material combinations. The optimal bandgap combinations between WBG (1.7~1.8 eV) and NBG (1.0~1.2 eV) perovskites have been estimated elsewhere to guide the TSC design.[194] Due to the fact that the classic Pb-based perovskite cannot be tuned to below 1.48 eV while the Sn-based materials are notoriously air-sensitive, the fabrication of stable and efficient NBG perovskite becomes the main challenge. With the ideal 1.2 eV NBG $FA_{0.75}Cs_{0.25}Sn_{0.5}Pb_{0.5}I_3$, the first representative p-i-n all-perovskite TSCs was fabricated by Snaith et al. in 2016.[229] Through a precursor-phase antisolvent immersion technique, the precursor complex is firstly formed due to retarded crystallization in a DMF/DMSO mixture solvent, followed by an antisolvent bath and gentle annealing for complete crystallization. As-

prepared materials were highly crystalline, uniform, smooth and dark, delivering a PCE of 14.8% and a V_{OC} of 0.74 V (with bandgap ~1.2 eV). Combining with a 1.8 eV perovskite in the construction of WBG perovskite top cell (PCE of 9.5%), the TSC delivered a notable PCE of 17.0% with a J_{SC} of 14.5 mA cm^{-2}, a V_{OC} of 1.66 eV and an FF of 0.70, exceeding either individual subcells. To meet the requirement of current matching between two subcells, the NBG perovskite should be thick enough to absorb sufficient infrared light. However, limited by the suitable fabrication and consequential bulk material imperfections, it is difficult to grow thick NBG perovskite without sacrificing FF or V_{OC}. To tackle this issue, Yan et al.[230] developed a strategy of incorporating chlorine into $(FASnI_3)_{0.6}(MAPbI_3)_{0.4}$ and successfully fabricated 750 nm thick perovskite films with good quality (**Fig. 2.13**). The 2.5% chlorine incorporation was found to segregate onto and passivates grain boundaries, resulting in enlarged grain with good crystallinity and reduced trap densities. These enabled fewer charge carrier scattering at grain boundaries and ionized defects, and therefore charge carrier transportation and extraction were facilitated. The reduced electronic disorder and suppressed non-radiative recombination guaranteed a good perovskite film and the NBG PSC obtained a high PCE of 18.1% with a V_{OC} of 0.841 V. Based on this efficient NBG subcell, the TSC obtained a total PCE of 21.0% with a V_{OC} of 1.922 V.

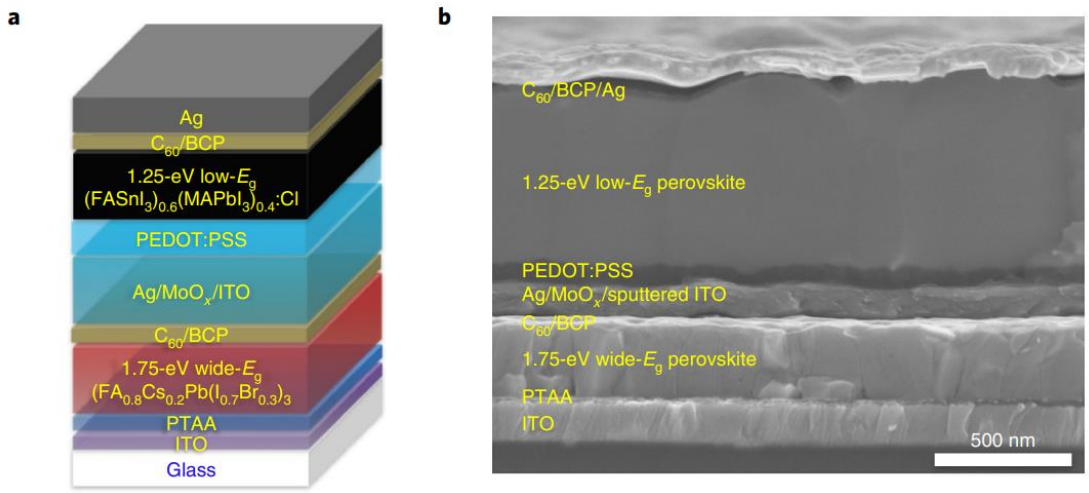


Fig. 2.13 Device structure for all-perovskite TSCs.
(a) Schematic diagram of and **(b)** Cross-sectional SEM image of the full cell.
Reproduced with permission from ref.[230] © The Author(s), under exclusive licence to Springer Nature Limited 2018

Following the idea of improving Sn-based perovskites, Zhu et al.[231] proposed the incorporation of another additive i.e. guanidinium thiocyanate (GuaSCN) into $(FASnI_3)_{0.6}(MAPbI_3)_{0.4}$, which presented a strong passivation ability. The treated perovskite showed reduced defect densities by a factor of 10, resulting in a long carrier lifetime > 1 microsecond and diffusion length > 2.5 micrometers. Such a treatment ensured the perovskite film with superior quality up to 1 micrometer thickness, providing sufficient infrared absorption and achieving a high J_{SC} of 30.5 mA cm^{-2} and the PCE exceeded the threshold of 20% for the first time to 20.2%. The final all-perovskite TSC also achieved a high PCE of 23.1%. Later, reductive zwitterionic antioxidant[232] and metallic Sn powder[124] have been separately used by Tan's group et al. to inhibit Sn^{2+} oxidation. The PCE of as-treated NBG cell and all-perovskite TSC were successfully enhanced to 21.7% and 24.8% respectively. Since the widely used surface passivators like PEA are partially adsorbed on the surface defective sites at perovskite crystallization temperatures, leading to the fact that a certain amount of grain surfaces are left un-passivated. To enhance the passivator adsorption on perovskite

surfaces, Tan et al.[130] reported a new ammonium cation, 4-trifluoromethyl-phenylammonium (CF3-PA), to passivate the NBG Pb-Sn perovskite. The theoretical calculation and experiments confirmed that CF3-PA noticeably suppressed the defects owing to the strongest binding energy with acceptor-type defects on the perovskite grain surface and increased Sn vacancy formation energy (**Fig. 2.14**). This effective passivator enabled much enhanced J_{SC} of 33 mA cm^{-2} due to the sufficient infrared light absorption from 1.2 micrometers thick absorber and a high PCE of 22.2% was measured. The final TSC hit an outstanding PCE of 26.7%, which, for the first time, surpassed the best PCE of single-junction PSCs.

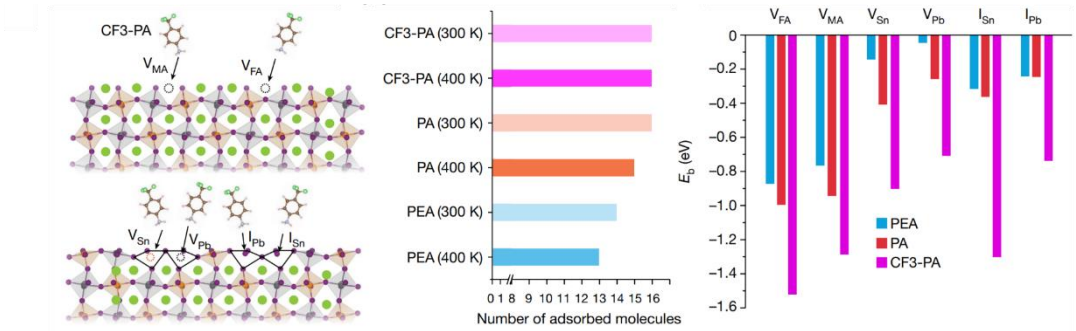


Fig. 2.14 Interaction between the passivator and NBG perovskite films.
(left) Schematic diagram of the interaction between CF3-PA with the defects in the perovskite film. (mid) The number of adsorbed molecules for CF3-PA, phenylammonium (PA) and PEA at 300 and 400 K. (right) The binding energy (E_b) between passivators and different acceptor-like defects. Reproduced with permission from ref.[130]. Copyright 2022 Springer Nature.

In addition to the improvement in the absorbers, copious efforts have also been put into the ICLs. It is noted that the achievement on ICLs is highly transferable between all-perovskite TSCs and POTSCs due to their similar device structures and fabrication routes. A typical ICL consists of several parts: ETL, HTL and recombination layer (RL)/tunnelling layer in most cases, which makes the design of ICLs an interactive and sophisticated engineering. Generally, the ICLs should meet the constraints from three aspects, e.g., electrics, optics and mechanics, plus practical processing compatibility.

The main role of ICLs in 2T TSCs is to electrically connect both subcells in series, which requires the annihilation of opposite charge carriers that occurs at ICLs. However, ETLs usually possess low work function while HTLs possess high work function, leading to an energy barrier for direct carrier transport and a parasitic p-n junction formed to ruin the TSCs' V_{OC}. To address this issue, there are two concepts of solutions: a) forming a tunnelling junction; b) forming a RL. In the former case, both sides of the small p-n junction are heavily doped, for narrowing the width of the depletion region thin enough to enable tunnelling through. This strategy has been widely applied in Ⅲ-Ⅴ group TSCs as the ease realization of degenerate doping in corresponding materials, which however is not applied to perovskite-based TSCs. Then perovskite researchers look into the second strategy where an ICL is constructed using a RL and a sandwiched structure of ETL/RL/HTL has been widely adopted in perovskite- and organic-based TSCs. Another requirement of ICLs is to be highly optically transparent, especially in the NIR region, to enable sufficient low-energy photons to pass through and arrive at the rear absorbers. Thirdly, ICLs should provide outstanding mechanical connections between two subcells. For example, ICLs should be compact enough to be physical barriers to solvent permeation and ion migration from the rear cells into the front cells. In particular, due to that both subcells in all-perovskite TSCs use similar strong polar solvents, it sets a higher standard of compactness to prevent solvent from dissolving the underlying layers. Therefore, the quality of ICLs impacts, and even determines, the performance and long-term stability of TSCs. To date, transparent conductive oxides (TCO) and metals are two dominant options for RLs in p-i-n TSCs, as summarized in **Table 2.5** and **Table 2.6**.

TCOs e.g.,, indium tin oxide (ITO), indium-doped zinc oxide (IZO), and aluminum-

doped zinc oxide (AZO), have inherent high transparency and conductivity, making them very compatible being the RLs. To produce a dense and compact film, the target TCO material will be magnetically sputtered with high energy, which may damage the underlying layers. Therefore, a dense and compact buffer layer is needed in advance to shield the sputtering damage. As the buffer layer also need to meet the three constraints applied to the ICLs, this inevitably introduces further complexity and uncertainty. In the first representative all-perovskite TSC,[229] Snaith's group demonstrated a sophisticated TCO-based ICL consisting of PCBM/SnO_2/zinc-tin-oxide (ZTO)/ITO/PEDOT:PSS. In this stack, SnO_2 (4 nm) /ZTO (2 nm) was deposited using the ALD technique as the buffer layer, followed by the sputtering of ITO with 100 nm. The dense ICL allowed for directly spin-coating of aqueous PEDOT:PSS on top. No distinct hysteresis was observed in the *J–V* curves of TSC, while the mismatched J_{SC} from two subcells meant there was plenty of room to further optimize. The small voltage loss of the TSC (defined as the difference between V_{OC_tandem} and the sum of V_{OC_front} and V_{OC_rear}) of 0.2 V and the FF of 0.70 demonstrated the effectiveness of carrier transportation and recombination within this ICL. Generally, this ICL fulfilled the basic duties and provided a good example of ICL design. Replacing the ALD-grown SnO_2, Yan's group[230] demonstrated the role of MoO_x used in ICLs. The multilayer Ag (1 nm) /MoOx (3 nm) /ITO (120 nm) was sandwiched between the ETL and HTL. In this stack, both ultrathin Ag and sputtered ITO were used together as the recombination sites, while MoO_x had a dual role of a buffer layer for preventing sputtering damage and a spacer to separate Ag from ITO (otherwise the silver oxide may form). With this ICL, the TSC voltage loss was reduced to a negligible value of ~0.07 V, and the FF reached 78.1%, proving it was an effective design. Due to the concern of rear cell solvent permeation, the sputtered TCOs have to be thick enough (~100 nm), which inevitably

increases the parasitic absorption and probably leads to shunting between subcells. Reducing the thickness of TCOs can be realized by sharing their responsibility of preventing solvent permeation e.g., by strengthening the ALD-grown dense films. In another work, Snaith's group[227] used the dense ALD-grown AZO film (25 nm) as the buffer layer followed by sputtering a thin layer of IZO with only 5 nm as the RL. This thin bilayer combined the merits of strong resistance to solvent permeation and high transparency. It is worth mentioning that the thin TCO made the ICL much less brittle and therefore the flexible devices can be made. In fact, the ALD-grown film can be further thinned to ~10 nm while still being effective solvent barriers.[233]

Although TCOs can almost meet the requirements from electrical and optical considerations, the high energy sputtering processing is usually needed which to some extent limits the wider applications. In contrast, ultrathin metal layers can be deposited through thermal evaporation at low temperatures, guaranteeing a less damaging fabrication process. The ultrathin metal layers (~1 nm) e.g., Au, have both good conductivity and transparency. Combined with the ALD-grown dense films, the metal-based RLs are expected to construct the qualified ICLs. Since SnO_2 has excellent electron extraction ability and is also ALD-grown friendly, SnO_2/Au becomes a competitive candidate for ICLs of all-perovskite TSCs. Note that a layer of C60 or PCBM is usually needed in advance of SnO_2 for two reasons: 1) ALD process starts with nucleation at substrates where PCBM surfaces have more suitable nucleation sites than bare perovskite surfaces; 2) water is widely used as oxidant during ALD process which is harmful to perovskite. The concept of SnO_2/Au-based ICL was realized by Tan's group in 2019.[124] Using the C60/SnO_2/Au/PEDOT:PSS as the ICL, the TSC generated a high PCE of 24.8%, a high FF of 81.0% and a negligible voltage loss of

0.06 V, demonstrating the huge success of this ICL. In the following years, a number of all-perovskite TSCs have adopted this concept as the ICLs and achieved high PCEs up to 26.7%, proving its wide applicability.[129,130,231,232]

Despite the success of ETL/RL/HTL sandwiched ICL concept, the TSC community is constantly pursuing simplifying the ICL structures to shorten the manufacturing time and lower the cost. In this regard, a pioneer work by Huang et al. on C60/$SnO_{1.76}$ set a good example.[126] In this work, through the precise control over the ALD process parameters e.g., pulse time, reaction time and temperature, the $SnO_{1.76}$ was intentionally left incomplete oxide and therefore possessed the ambipolar transport property (**Fig. 2.15**a). Owing to the incomplete oxidation status, a high density of Sn^{2+} existed in $SnO_{1.76}$ formed mid-gap states, enabling the extraction ability of holes from the rear cells. Also, the C60 layer was unintentionally n-doped by the iodine ions from adjacent perovskite materials, thereby forming the Ohmic contact with $SnO_{1.76}$ (**Fig. 2.15**b). This ingenious ICL obtained a PCE of 24.6% with a high FF of ~80% and a small V_{OC} loss of ~0.1 V, indicating that the bilayer ICLs, and even monolayer ICLs, become feasible in the future and point the direction of enhancing ICL fabrication efficiency (**Fig. 2.15**c).

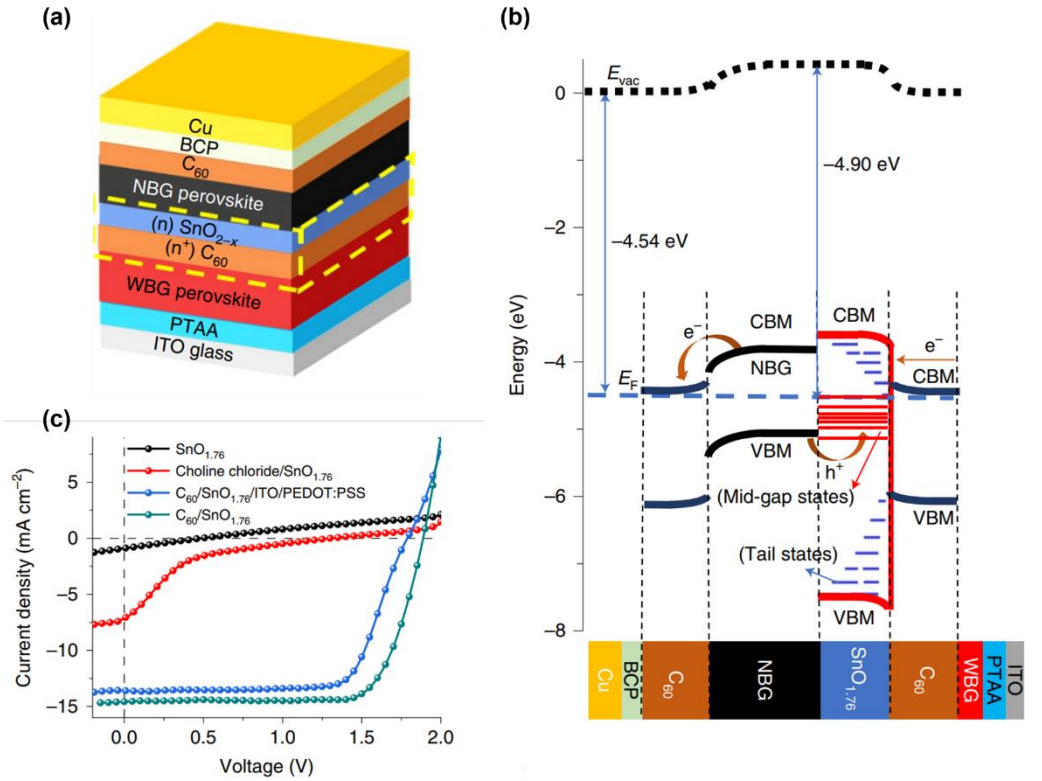


Fig. 2.15 Working mechanism of the ICL of C60/$SnO_{1.76}$.
(a) Schematic of the device architecture with simplified ICL highlighted by the yellow-dash rectangle. (b) *J–V* characteristics of the TSCs with various ICLs. (c) Energy-level scheme for the C60/$SnO_{1.76}$/NBG/C60 layers in all-perovskite TSCs. Reproduced with permission from ref.[126]. Copyright 2020 Springer Nature.

In summary, the all-perovskite TSCs can be further improved as follow:

1) efficient NBG PSCs with good stability. The poor resistance to the ambient environment not only limits the efficiency of NBG but also impedes the mass production at the industrial level.

2) Simpler and more efficient ICL design and manufacture. Generally, the fabrication of ICLs is still waiting for further simplification. Spatial-ALD is one possible direction to speed up the time-consuming ALD process. The research into monolayer ICL using ambipolar materials would be the goal.

3) efficient WBG PSCs with small voltage losses. Similar to perovskite-Si TSCs, the enhancement of TSCs hugely depends on the minimization of WBG voltage loss.

Table 2.6 Summary of representative 2T all-perovskite and POTSCs with p-i-n configuration. Values in the brackets are certified.

Front contacts	WBG/front cell	ICL	NBG/rear cell	Rear contacts	V_{OC} (V)	J_{SC} (mA cm^{-2})	FF (%)	PCE (%)	Year	Ref.
ITO/NiO_x/SAM	$FA_{0.8}Cs_{0.2}Pb(I_{0.62}Br_{0.38})_3$	C60/SnO_2/Au/PEDOT:PSS	$FA_{0.7}MA_{0.3}Pb_{0.5}Sn_{0.5}I_3$	C60/BCP/Cu	2.13	16.4	80.3	28.5 (28.0)	2023	[234]
ITO/NiO_x/VNPB	$FA_{0.8}Cs_{0.2}Pb(I_{0.62}Br_{0.38})_3$	C60/SnO_2/Au/PEDOT:PSS	$FA_{0.7}MA_{0.3}Pb_{0.5}Sn_{0.5}I_3$	C60/BCP/Cu	2.03	16.5	79.9	26.7 (26.4)	2022	[130]
ITO/NiO_x/VNPB	$DMA_{0.1}FA_{0.5}Cs_{0.4}Pb(I_{0.75}Br_{0.25})_{2.95}Cl_{0.05}$	C60/SnO_2/Au/PEDOT:PSS	$MA_{0.3}FA_{0.7}Pb_{0.5}Sn_{0.5}I_3$	C60/BCP/Cu	2.05	16.0	80.1	26.2	2022	[129]
ITO/PTAA	$FA_{0.6}Cs_{0.4}PbI_2Br$	C60/SnO_2/graphene oxide/PEDOT:PSS	$Cs_{0.2}FA_{0.8}Pb_{0.5}Sn_{0.5}I_3$ + BaI_2	C60/BCP/Cu	2.03	15.8	79.4	25.6	2022	[235]
ITO/MeO-2PACz	$FA_{0.7}Cs_{0.3}PbI_{2.1}Br_{0.9}$	LiF/C60/SnO_x/Au/PEDOT:PSS	$(FASnI_3)_{0.6}(MAPbI_3)_{0.4}$	C60/BCP/Ag	2.12	15.0	80.1	25.5 (24.3)	2022	[236]
ITO/PTAA	$FA_{0.8}Cs_{0.2}Pb(I_{0.6}Br_{0.4})_3$	C60/SnO_2/Au/PEDOT:PSS	$FA_{0.7}MA_{0.3}Pb_{0.5}Sn_{0.5}I_3$	C60/BCP/Cu	1.97	15.6	81.0	(24.8)	2019	[124]
ITO/NiO_x	$FA_{0.8}Cs_{0.2}Pb(I_{0.6}Br_{0.4})_3$	C60/SnO_2/Au/PEDOT:PSS	$FA_{0.7}MA_{0.3}Pb_{0.5}Sn_{0.5}I_3$	C60/SnO_2/Cu	2.01	15.5	79.3	24.7 (24.2)	2020	[232]
ITO/PTAA	$FA_{0.6}Cs_{0.4}Pb(I_{0.65}Br_{0.35})_3$	C60/$SnO_{1.76}$	$FA_{0.5}MA_{0.45}Cs_{0.05}Pb_{0.5}Sn_{0.5}I_3$	C60/BCP/Cu	2.03	15.2	79.7	24.6	2020	[126]
ITO/MeO-2PACz	$FA_{0.8}Cs_{0.2}Pb(I_{0.5}Br_{0.5})_3$	PCBM/AZO-NP/SnO_x/InO_x/MoO_x	PM6:Y6:PCBM	C60/BCP/Ag	2.15	14.1	78.0	24.0 (23.1)	2022	[237]
ITO/NiO_x/BPA	$FA_{0.75}Cs_{0.25}Pb(I_{0.6}Br_{0.4})_3$	C60/BCP/IZO/MoO_x	PM6:Y6:PCBM	PNDIT-F3N/Ag	2.06	14.8	77.2	23.6 (23.0)	2022	[238]
ITO/PTAA	$FA_{0.8}MA_{0.15}Cs_{0.05}Pb(I_{0.85}Br_{0.15})_3$	C60/BCP/Ag/MoO_x/ITO/PEDOT:PSS	$(FASnI_3)_{0.6}(MAPbI_3)_{0.4}$	C60/BCP/Ag	1.94	15.0	80.3	23.4	2019	[231]

ITO/poly-TPD	$FA_{0.6}DMA_{0.1}Cs_{0.3}Pb(I_{0.8}Br_{0.2})_3$	LiF/C60/PEIE/AZO/IZO/PEDOT:PSS	$FA_{0.75}Cs_{0.25}Sn_{0.5}Pb_{0.5}I_3$	C60/BCP/Ag	1.88	16.0	77.0	23.1	2019	[239]
ITO/2PACz	$FA_{0.6}MA_{0.4}Pb(I_{0.6}Br_{0.4})_3$	C60/BCP/Ag/MoO_x	PTB7-Th:BTPV-4CleC9	PDINN/Ag	1.88	15.7	74.6	22.0	2022	[240]
ITO/poly-TPD	$MA_{0.96}FA_{0.1}PbI_2Br(SCN)_{0.12}$	PCBM/BCP/Ag/MoO_x	PM6:CH1007	PFN-Br/Ag	1.96	13.8	78.4	21.2	2022	[241]
ITO/PTAA	$FA_{0.8}Cs_{0.2}Pb(I_{0.7}Br_{0.3})_3$	C60/BCP/Ag/MoO_x/ITO/PEDOT:PSS	$(FASnI_3)_{0.6}(MAPbI_3)_{0.4}$	C60/BCP/Ag	1.92	14	78.1	21.0	2018	[230]
ITO/NiO_x	$FA_{0.8}MA_{0.02}Cs_{0.18}PbI_{(0.6}Br_{0.4})_3$	C60/BCP/Ag/MoO_x	PM6:Y6:PC71BM	TPBi/Ag	1.90	13.1	83.1	20.6 (19.5)	2020	[242]
ITO/NiO_x	$FA_{0.83}Cs_{0.17}Pb(I_{0.5}Br_{0.5})_3$	PCBM/SnO_2/ZTO/ITO/PEDOT:PSS	$FA_{0.75}Cs_{0.25}Sn_{0.5}Pb_{0.5}I_3$	C60/BCP/Ag	1.66	14.5	70	17.0	2016	[229]
ITO/PEDOT:PSS	$MAPbI_3$	PCBM/C60-SB/Ag/MoO_3	PTB7-Th:PC71BM	C60-N/Ag	1.63	13.1	75.1	16.0	2016	[243]

2T Perovskite-Organic TSCs (POTSCs)

Benefiting from the progress of NFA with narrow bandgaps[244] as the rear subcell, the past several years have witnessed rapid advances in high-efficiency monolithic POTSCs. This type of TSC shares a high similarity in device structure with the all-perovskite TSC, only replacing the NBG perovskite rear cell with the NBG organic rear cell, enabling that the lessons learned from each other is usually transferable e.g. the design of ICLs. This replacement provides the design of TSCs with more freedoms and flexibility, as the orthogonal solvents are used in two subcells which relieves the concerns on solvent permeation in all-perovskite TSCs. By taking advantage of this unique feature, the WBG perovskite and NBG organic bulk heterojunction (BHJ) can be even contacted directly without the ICLs inserted thus forming the so-called perovskite-organic bilayer integrated cells. This type of hybrid cell is another promising topic in recent years while it is beyond the scope of this review. The interested readers are advised to read the information elsewhere.[245] **Table 2.6** summarizes the high-efficiency p-i-n POTSCs reported in recent years. Compared with the all-perovskite TSCs, it is clear that POTSCs show general inferior PCEs, which mainly result from the lower J_{SC} and FF. Considering that the NBG rear cell is the only different part, the development of organic light-absorbers highly determines the overall TSC performance.

In 2015, Yang's group reported a pioneer work where an organic BHJ of PBSeDTEG8:PCBM was used as the infrared absorber and worked with $MAPbI_3$ to construct the TSC.[246] The mismatched bandgap combination between two subcells led to the distinct absorption overlap. Also, since the absorption coefficient of organics was lower than that of perovskites, the NBG organic subcell was placed in front of the WBG

perovskite subcell for absorbing more light and matching the current. This stack order however obstructed the sufficient absorption of high-energy photons by the WBG perovskite subcell and therefore further decreased the total J_{SC} attainable. Although the final TSC obtained a PCE of 10.23% with a J_{SC} of 10.05 mA cm^{-2}, this work paves an avenue that POTSC can deliver further high PCEs with more reasonable structures if efficient NBG organic absorbers are synthesized. Given that the organic subcell is the performance-limiting factor, Russell's group optimized it in both BHJ composition and stack order.[243] Interestingly, despite that the PCE of the organic subcell had a small increasement (from Yang' work 7.03% to this work 9.7%) while the same perovskite was used, the PCE of TSC saw a large increment (from Yang's work 10.23% to this work 16.0%), together with the enhancement of J_{SC} to 13.1 mA cm^{-2}, implying the contribution and importance of organic subcells on TSC performance. Since then, the efficiency gap between all-perovskite TSCs and POTSCs is increasingly widening due to the skyrocketing development of NBG Pb-Sn perovskites.

The development of POTSCs waited for more efficient NBG organic absorbers, and the successful application of NFA in OSCs has brought a new round of breakthroughs. In 2020, the PM6:Y6:PCBM, a star NFA-based BHJ, was used as the NBG absorber in the POTSC by Yang's group.[242] Thanks to the NBG absorber's strong light-harvesting ability, the inter-subcell current matching was easily fulfilled through thickness optimization guided by the device simulation. More importantly, both the FF and V_{OC} of NFA-based organic subcell benefited from a much-improved film morphology and reduced non-radiative recombination, providing more efficient carrier dissociation and transportation. The big breakthrough in organic subcells led to the enhancement in V_{OC}

and FF of TSC to 1.902 V and 83.1%, respectively, and final PCE exceeded the 20% milestone for the first time. Based on this star NFA-based BHJ as the NBG absorber, He's group[238] and Riedl's group[237] had further optimized the WBG subcells and ICL, and successively lifted the record PCE of POTSCs to 23.6% and 24.0% respectively. Despite the success achieved by the PM6:Y6:PCBM, the NFA in this BHJ absorber i.e. Y6 possesses a bandgap of ~1.4 eV, which is larger than the optimal 1.15 eV[240] to pair with the typical WBG perovskite with bandgaps around 1.75 eV. The nonideal bandgap combination between WBG and NBG leads to the inefficient absorption of incident light and therefore lower Jsc. To tackle the issue, another NFA, BTPV-4Cl-eC9, with 1.22 eV bandgap was synthesized by Meng's group.[240] As a result, the NBG single cell delivered an ultrahigh J_{SC} of 28.6 mA cm^{-2}. Based on this efficient NFA organic cell, the TSC eventually achieved a PCE of 22.0% with the highest J_{SC} of 15.7 mA cm^{-2} among all POTSCs to date, which is also comparable with that of all-perovskite TSCs. The main PCE deficit resulted from the low V_{OC} of this new NFA-based NGB subcell which provided room for future enhancement.

Since the debut of NFA, the POTSCs saw rapid development in the past several years and are still in the close running after their all-perovskite counterparts. In the near future, the advance of POTSCs will still rely on the progress of NBG OSCs as they are the limiting subcells. Specifically, the organic absorbers with more suitable (narrow) bandgap with strong abilities of light absorption, exciton dissociation, and carrier transportation are expected. With the understanding deepening into the working mechanism of NFA-based absorbers, device engineering and material innovation, the PCE of single-junction OSCs is expected to surpass 20% or even higher soon. And the

competitiveness between all-perovskite and POTSCs will continues. For simplicity, the potential advantages of POTSCs are summarized below.

Compared to the perovskite-Si TSCs, POTSCs have the following advantages:

- Much easier to tune the bandgap for complementary light absorption.
- Share the similar device structure for PSCs and OSCs, and thus processing routes that simplifies the fabrication.
- Similar solution-processed routes and shorter processing steps against silicon production make the POTSCs competitive economically given that the complete industrial chain is established.
- POTSCs are compatible with flexible substrates which is difficult to silicon.

Compared to the all-perovskite TSCs, POTSCs have the following advantages:

- OSC and PSC use orthogonal solvents that much relaxes the burden for ICLs.
- All-perovskite TSCs rely on Sn-containing perovskite as the narrow bandgap absorber which is oxidatively unstable that strongly limits the overall stability. In comparison, UV light as one of the most threatening factors for OSCs can be absorbed firstly by the front WBG PSCs, thereby protecting the rear OSCs. Recently, OSCs with 17.0% can have a T90 more than 1300 h under 65 degree thermal stressing, which is yet reported for highly efficient Sn-based PSCs.[247]

2.3.3 Design criteria for TSCs

This section summarizes the key information introduced in **Section 2.3.1-2.3.2** and provides practical guidance for designing a perovskite TSC with 2T configuration that

will be referred in this thesis. In general, there are three main points to consider: optical, electrical and mechanical.

Optical

Firstly, two subcells should absorb complementarily over the solar spectrum. Usually WBG is responsible for high energy photons (close to blue) while NBG is responsible for low energy photons (close to red). Based on calculation, a PCE of 45.8% can be achieved when pairing a 1.6 eV WBG with a 0.95 eV NBG, as shown in the **Fig. 2.16**.[248] In reality, the thickness of each absorber can be varied in order to control the subcell photocurrent generation, therefore this provides extra flexibility for subcell pairing. In practice, an optical modelling method based on transfer matrix algorighm is widely used to account for the optical interference effect within the thin film layered stacks which will be introduced in **Section 3.4**.[249,250] The calculated results demonstrate the absorption distribution through the layered stacks and thereby provide guidance in thickness optimization. Limited by the practical issues, however, the highly efficient NBG cells are difficult to make below 1.2 eV bandgap.[130] Thus, a NBG with 1.2-1.3 eV with a WBG with 1.7-1.8 eV are commonly used in fabricating TSCs, particularly for all-perovskite TSCs and POTSCs. Given that subcells are in-series connected in 2T configured TSCs, current matching should be meet due to the Kirchhoff's law. So to avoid current loss, the thickness of each subcell should be adjusted in order to generate similar current output. Additionally, parasitic absorption and reflection loss are also required to be minimized. Thereafter, ICLs should be as transparent as possible in order that sufficient light pass through and reach the NBG subcells. As shown in **Table 2.6**, ultrathin Au or Ag layers with 1 nm thickness have been widely used for efficient all-perovskite TSCs and POTSCs. Note that as metal has high reflecitivity, there are

increasingly interests to replace ultrathin metal layers with transparent conducting oxides (TCOs) e.g. InOx and IZO to further minimize the reflection loss.[237,238]

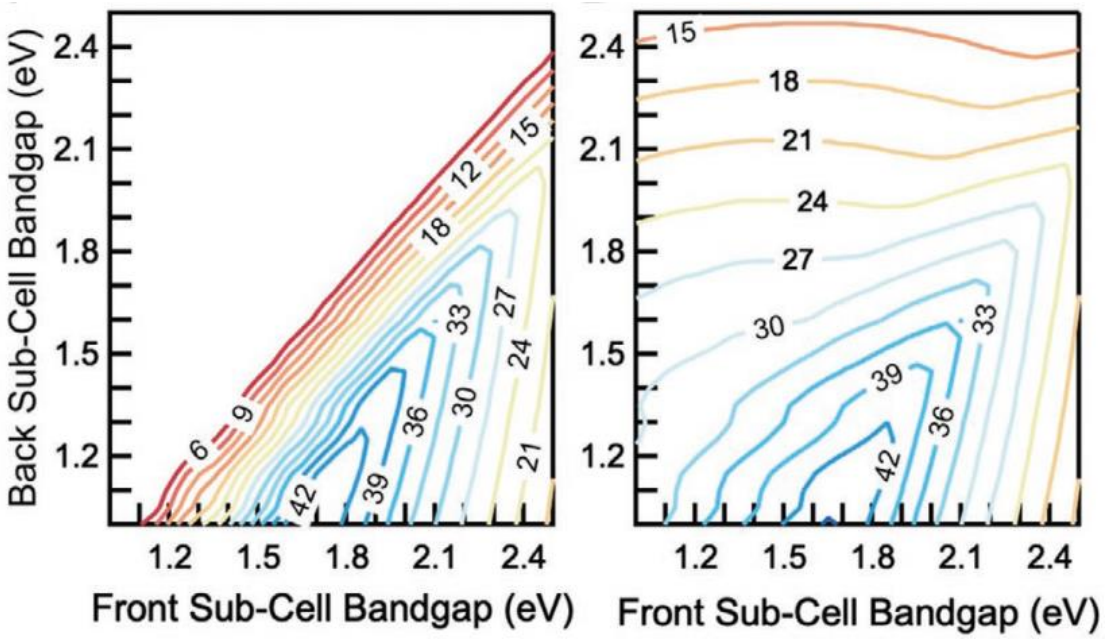


Fig. 2.16 Relationship between bandgap combinations of two subcells and simulated efficiency. (left) with fixed thickness. (right) with variable thickness. Reproduced with permission from Ref. [248]. Copyright © 2017 American Chemical Society

Electrical

After picking absorbers with suitable bandgaps, next step is to consider the electrical aspect. In 2T configured TSCs where subcells are in-series connected, proper design on ICLs is needed to electrically connect both subcells. In the 2T TSC, ICLs should extract carriers with opposite charges generated from both subcells (Ohmic contact) and provide sites for them to recombine efficiently (high recombination rates). For this purpose, ICLs suppose to have high vertical conductivity (small vertical resistance for efficient carrier recombination) and low lateral conductivity (no shunt path, no leakage current) to avoid low FF or S-shaped kink. Two main routes of ICLs are proposed in 2T TSCs. Firstly, a tunnel junction as the ICL can be formed via heavily doping the p-n

junction. The high doping narrows the depletion region to several nanometers, allowing the charge tunnelling occurs. Note that tunnelling-based ICLs are more commonly utilized for III-V TSCs where it is easier to satisfy the condition of degenerate doping to achieve atomically sharp homojunctions through epitaxial growth via high-vacuum deposition techniques, which is difficult for transrporting layers for PSCs. Secondly, a recombination layer can also be used as the ICL. In this case, a layer of TCO or ultrathin metals with excellent conductivity are usually deposited between two subcells. It is noted that the choice of materials should take the trade-off between optical and electrical requirement into account. As summarized in **Table 2.5** and **Table 2.6**, the widely used TCOs include IZO, ITO, InOx, ZTO, $SnO_{1.76}$, and Ag and Au are the representatives of metal-based recombination layers.

Mechanical

Last but not the least, fabricating 2T TSC should consider the mechanical aspects. Firstly, the processing of latter layers should not damage the previous layers, which usually refer to e.g. high annealing temperature, high energy sputtering without buffer protection. The ICLs can be deposited through solution-processing, thermal evaporation, sputtering and ALD. Moreover, some materials can be deposited by more than one method. For example, Al-doped zinc oxide (AZO) can be processed by spincoating in the form of nanoparticle dispersion[237], by sputtering[251] or by ALD[252]. Film qualities and properties prepared by different routes can vary widely, therefore it is necessary to choose the proper fabrication route. Secondly, ICLs should be compact and impermeable to prevent the solvent permeation downwards during the latter layer processing, which is even paramount for solution-processed all-perovskite TSCs as the deposition of rear perovskitse may dissolve the front perovskites. Applying unusual

solvents beyond the common DMF and DMSO[253] and thick TCO layers[229] as ICLs are two proved solutions at the expense of less efficiency and increased parasitic absorption, respectively. In contrast, the commonly used solvents used for perovskites e.g. dimethylformamide (DMF), dimethyl sulfoxide (DMSO) are orthogonal with those used for organic films e.g. chlorobenzene, giving rise to much reduced burden in designing ICLs for POTSCs and offering more flexibilities in materials selections and combination.

3. Methods

3.1 Materials

Table 3.1 below summarizes the materials used in the experimental works. All reagents and solvents were purchased commercially as analytically pure and used without further purification unless stated.

Table 3.1 Materials used in the experimental chapters.

Acronym	Full name	Supplier
NiO_x	Nickel oxide	Liaoning Youxuan Co., Ltd
MeO-2PACz	[2-(3,6-dimethoxy-9H-carbazol-9-yl)ethyl]phosphonic Acid	TCI Co., Ltd, Japan
2PACz	[2-(9H-Carbazol-9-yl)ethyl]phosphonic Acid	TCI Co., Ltd, Japan
PTAA	Poly[bis(4-phenyl) (2,4,6-trimethylphenyl)amine] (M_w~13000)	Xi'an Polymer Light Technology Corp.
PbI_2	Lead iodide	TCI Co., Ltd, Japan
$PbBr_2$	Lead bromide	TCI Co., Ltd, Japan
FAI	Formamidinium iodide	Greatcell Solar
MAI	Methylammonium iodide	Greatcell Solar
MABr	Methylammonium bromide	Greatcell Solar
RbI	Rubidium iodide	Alfa Aesar
CsI	Cesium iodide	Sigma Aldrich
$[BMP]^+[BF_4]$	1-butyl-1-methylpiperidinium tetrafluoroborate	Sigma Aldrich
PEAI	Phenylethylammonium iodide	Xi'an Polymer Light Technology Corp.
PM6	PM6	1-Material Inc.
Y6	Y6	1-Material Inc.
PFNBr	Poly[9,9-bis[3-(ethyldimethylammonio)propyl]-9',9'-dioctyl[2,2'-bi-9H-fluorene]-7,7'-diyl dibromide], M_w~22000	Organtec Ltd
PCBM	[6,6]-phenyl-C_{61}-butyric acid methyl ester	Nano-C Tech USA
C60	Fullerene	Advanced Election Technology Co., Ltd
BCP	Bathocuproine	Advanced Election Technology Co., Ltd, Jilin OLED Company

Yb	Ytterbium	Kurt Lesker (Shanghai) Trading Company Inc
MgF_2	Magnesium fluoride	Alfa Aesar
DMF	Dimethylformamide	Acros
DMSO	Dimethyl sulfoxide	Acros
IPA	Isopropanol	Acros
Anisole	Anisole	Acros, Macklin
CB	Chlorobenzene	Acros
Toluene	Toluene	Sinopharm Chemical Reagent Co., Ltd

3.2 Solar cells preparation

Perovskite precursor solution

The WBG perovskite precursor solution for the composition $FA_{0.83}Cs_{0.17}Pb(I_{0.6}Br_{0.4})_3$ was prepared by mixing PbI_2 (0.56 M), FAI (1.16 M), $PbBr_2$ (0.84 M), and CsI (0.24 M) in a mixed solvent of DMF/DMSO (4/1, v/v), and the resulting precursor solution was stirred at 50℃ for 5 h before use. For the NBG perovskite, the perovskite used is $Rb_{0.05}Cs_{0.05}MA_{0.05}FA_{0.85}Pb(I_{0.95}Br_{0.05})_3$. The perovskite precursor solution was prepared by mixing CsI (19.5 mg), RbI (15.9 mg), MABr (8.4 mg), FAI (219.5 mg), PbI_2 (656.9 mg), and $PbBr_2$ (27.5 mg) were dissolved in 1 mL mixed solvent of DMF:DMSO (4/1, v/v) and the resulting precursor solution was stirred at 50℃ for 2 h before use.[1] For the MBG perovskite, the perovskite composition is $(Cs_{0.05}FA_{0.85}MA_{0.10})_{0.95}Pb(I_{0.85}Br_{0.15})_3$. The perovskite precursor solution was prepared by mixing PbI_2 (1.28 M), FAI (1.21 M), MABr (0.16 M), $PbBr_2$ (0.22 M), and CsI (0.07 M) in a mixed solvent of DMF/DMSO (4/1, v/v), and the resulting precursor solution was stirred at 70℃ for 2 h before use.

Organic precursor solution

For the NBG organic precursor solution, PM6:Y6 = 1:1.2 by weight was added in choloroform or CB with a concentration of 7 mg/ml referring to PM6 with 0.5 % v/v CN (Chloronaphthalene) additive. The organic solution was stirred at 50℃ for 2 h before use.

PSC fabrication

Before device fabrication, the pre-patterned ITO or FTO substrates were ultrasonically cleaned using an aqueous detergent solution, deionized water, acetone, and IPA for 20 min. Subsequently, the as-cleaned ITO and FTO substrates were treated with UV-ozone for 10 min.

For the WBG perovskites with different geometries used in Chapter 4, the PTAA solution (2 mg/ml in toluene) was spin-coated on the as-cleaned ITO glass substrates at 5000 rpm for 30 s with a ramping rate of 2000 rpm s^{-1}, and they were annealed at 120 °C for 10 min to form the hole transport layer. For the mountain-type film, 75 μL of PFN-Br solution (1mg/ml in methonal) was spin-coated on hole transport layer at 5000 rpm for 30 s with a ramping rate of 2000 rpm s^{-1} before depositing perovskite solution. For the hill-type film, an additional step of 90 μL of DMF was spin-coated on PFN-Br layer at 5000 rpm for 30 s with a ramping rate of 2000 rpm s^{-1}. For the flat-type film, 90 μL of DMF was spin-coated on PTAA layer at 5000 rpm for 30 s with a ramping rate of 2000 rpm s^{-1} without PFN-Br. Afterwards, the perovskite precursor solution was spin-coated on the modified hole transport layer by a two-step program: 1000 rpm for 10 s with a ramping rate of 1000 rpm s^{-1}, and 5000 rpm for 35 s with a ramping rate of 1000 rpm s^{-1}. During the two-step spin-coating program, 200 μL of anisole was poured

on the center of the spinning substrate at 5 s prior to the end of the whole program. The samples were immediately annealed at 100 °C for 20 min to form the perovskite films.

For the WBG perovskites used in Chapter 5 and 6, 15 mg mL^{-1} NiO_x nanoparticle in the mixed solvent of IPA: deionized water (1:3) solution was spin-coated onto ITO substrates at 3,000 r.p.m. for 30 s (with a ramping rate of 1,000 r.p.m. s^{-1}), and as-formed films were heated at 150°C for 30 min in air. The subsequent overlayers were deposited after the substrates cooled down to room temperature. The following operations were all carried out in an N_2-filled glovebox (with H_2O and O_2 concentrations of < 0.1 ppm). Before depositing the perovskite layer, the NiO_x film was modified by the self-assembling monolayer of 2PACz and MeO-2PACz. The solutions of 2PACz and MeO-2PACz with the same concentration (0.5 mg mL^{-1} in ethanol) were mixed with the volume ratio of 1:1, and then the mixed solution of 2PACz and MeO-2PACz was spin-coated onto the NiO_x film at 3,000 r.p.m. (with a ramping rate of 1,000 r.p.m.s^{-1}) for 30 s followed by annealing at 100°C for 5 min. When the films cooled down to room temperature, the perovskite precursor solution was deposited onto the substrates by a consecutive two-step program at 1,000 rpm for 10 s with a ramping rate of 1,000 r.p.m.s^{-1} and 5,000 r.p.m. for 35 s with a ramping rate of 1000 r.p.m. s^{-1}. During the second step, 300 μL-anisole doped with the ionic liquid ($[BMP]^+[BF_4]^-$, 0.01 mg mL^{-1}) was poured on the center of the spinning substrates at 5 s before the end of the whole program. Then the samples were immediately transferred to the hotplate, annealing at 100°C for 30 min. For the post-treatment of the wide-bandgap perovskite films, 200-μL of PEAI (5 mg mL^{-1} in IPA) and 100-μLof MAI (5 mg mL^{-1} in IPA) were mixed in 705-μL of a mixed solvent of DMF/IPA (5/700, v/v) to obtain 1,005-μL of post-treatment solution. Then 50-μL of post-treatment solution was dynamically spin-

coated on top of the perovskite film after the perovskite film, followed by annealing at 100°C for 5 min.

For the MBG perovskite, 2 mg mL^{-1} PTAA (in toluene) solution was spin-coated onto ITO substrates at 5,000 r.p.m. for 30 s (with a ramping rate of 2,500 r.p.m. s^{-1}), and as-formed films were heated at 120°C for 10 min. The subsequent overlayers were deposited after the substrates cooled down to room temperature. Then, the PEAI solution (10 mg mL^{-1} in IPA) was spin-coated onto the PTAA-coated substrates at 5,000 r.p.m. for 30 s (with a ramping rate of 2,500 r.p.m. s^{-1}), and then the samples were heated at 100°C for 5 min. Subsequently, the perovskite films were spin-coated onto the substrates by a two-step program at 2,000 r.p.m. for 10 s (with a ramping rate of 200 r.p.m. s^{-1}) and 6,000 r.p.m. for 30 s (with a ramping rate of 1,000 r.p.m. s^{-1}), respectively. During the second step, 100 μL-CB was poured on the center of the spinning substrates 16 s before the end of the whole program. Then the samples were immediately transferred to the hotplate, annealing at 105°C for 30 min.

For the NBG perovskite, the MeO-2PACz (0.5 mg mL^{-1}, in ethanol) solution was spin-coated onto the pre-cleaned FTO substrates at 3,000 r.p.m. for 30 s and annealed at 100°C for 10 min in an N_2-filled glove box. The perovskite films were prepared according to the previous work.[254]

After the deposition of perovskite films, for the WBG perovskties with different geometries and NBG perovskites, the PCBM solution (20 mg mL^{-1} in CB) was spin-coated on top of the perovskite layer at the speed of 1,000 r.p.m. for 30 s (with a ramping rate of 200 r.p.m. s^{-1}). For the WBG and MBG perovskites used in Chapter 5 and 6, C60

(35 nm) was thermally evaporated in a vacuum chamber with a base pressure of < 4×10^{-4} Pa. Then for the devices with the BCP interlayer, BCP (1 mg/ml in ethanol) was spin coated on the film at 5000 rpm for 30 s with a ramping rate of 2000 rpm s^{-1}. For other devices, the Yb_2O_3 buffer layer (1.5 nm) was obtained by the thermally evaporated Yb in the vacuum chamber. The thermal evaporation rate for the metal ytterbium is 1 Å/s. The device fabrication is done in a N_2 glovebox (with H_2O and O_2 concentrations of < 0.1 ppm). Finally, a 100-nm thick Cu electrode was thermally evaporated onto the samples in the vacuum chamber (<4×10^{-4} Pa) through a metal shadow mask with an aperture area of 10.3 mm^2. The aperture mask area for the photovoltaic performance tests is 9 mm^2. Besides, for the WBG and MBG devices, MgF_2 (100 nm) was deposited on the glass side of the ITO substrate as the anti-reflection coating, while for the NBG devices, MgF_2 (125 nm) was deposited on the glass side of the FTO substrate.

OSC fabrication

For the single junction OSCs, MoOx (10 nm) was deposited on the cleaned-ITO substrates. The organic PM6:Y6 precursor solution was dynamically spin-coated (2000 rpm, 60 s) on the top of the MoOx layer, followed by the annealing of 85 °C for 5 min. After cooling, PFN-Br (0.5 mg mL^{-1}, in methonal) was spin-coated (2500 rpm, 30 s). In the end, Ag (100 nm) was thermally evaporated as the cathode.

POTSC fabrication

For the POTSCs, main steps followed the WBG PSC fabrication route expect the concentration of perovskite precursor solution was made to 1 M. After the deposition

of Yb_2O_3 (1.5 nm), Au (1 nm) and MoO_x (10 nm) were subsequentially thermal evaporated. Then the steps followed the OSC fabrication route.

3.3 Thin films and solar cells characterations

Photovoltaic performance characterizations

The J–V characteristics were performed in the ambient air using a Keithley 2400 Source Meter under AM 1.5G illumination with a Xenon-lamp solar simulator (XES-40S1, SAN-EI). Before the measurement, the light intensity of 100 mW cm^{-2} was calibrated using a standard monocrystalline silicon solar cell with a KG-5 filter. The steady-state/stablized power output (SPO) were performed in the ambient air by holding the devices at the fixed voltage of the maximum power point (MPP) under the simulated AM 1.5 G light at 100 mW cm^{-2} recorded by a Keithley 2400 Source Meter.

The EQE of devices were measured in the air with a Newport QE Test Model 77890 (Newport Co. Ltd.) during illumination with monochromatic light from a Xenon lamp. For the EQE of subcells of POTSCs, a Xeon light source was used as bias light, a 550 nm short-wave filter was used to saturate the WBG perovskite cell and a 850 nm long-wave filter was used to saturate the NBG organic cells. The EQE measurement were measured by Bin Liu (SUSTech), Peng Chen (PKU) and Xin Jiang (ICCAS)..

Electroluminescence performance characterizations

EQE_{EL} was carried out at room temperature (297 K) in a N_2 glovebox. A Keithley 2400 Source Meter and an integration sphere (CME-LP38) coupled with a spectrometer (Flame, Ocean Optics) were used for the measurements. The device was placed on top

of the integration sphere, and only forward light emission can be collected. The devices were swept from zero bias to forward bias. The EL tests were measured by Maotao Yu and Peng Chen, PKU. To calculate the Quasi Fermi-level Splitting (QFLS) from EQE_{EL}, the following approach follows the report by Rau et al[255]. Briefly the black body photon flux is

$$\phi_{\mathrm{BB}} = \frac{1}{4\pi^2\hbar^{3^2}} \frac{E^2}{\exp\left(\frac{E}{k_{\mathrm{B}}T}\right) - 1} \qquad (Equation\ 3.1)$$

with ħ Plank's constant, k_B Boltzmann constant and T temperature. Assuming that the perovskite solar cell is at 300 K in thermal equilibrium with its environment, the dark radiative recombination current is:

$$J_{\mathrm{em,0}} = q \int EQE_{\mathrm{PV}}(E)\phi_{\mathrm{BB}}(E)dE = J_{\mathrm{rad,0}} \qquad (Equation\ 3.2)$$

with EQE_{PV} the photovoltaic *external* quantum efficiency of the perovskite solar cell and $J_{\mathrm{em,0}}$ the current giving rise to emission, which also defines the dark radiative recombination current at $V = 0$. In this case, $J_{\mathrm{rad,0}}$ has been calculated using the Shockley-Queisser approach for each different bandgap.[6] From that, the radiative limit of the QFLS ($\mathrm{QFLS_{rad}}$) (EQE_{EL} = 1) can be calculated with the following equation:

$$\mathrm{QFLS_{rad}} = \frac{k_{\mathrm{B}}T}{q} \ln\left(\frac{J_{\mathrm{G}}}{J_{\mathrm{rad,0}}} \cdot 1\right) \qquad (Equation\ 3.3)$$

where J_{G} is the generation current under illumination, approximated to the short circuit current J_{sc} of each bandgap.

Stability assessment

For the thermal stability test, all encapsulated devices were protected using glass covers sealed by epoxy resin, and then placed on a hotplate at 85°C in the dark in a N_2 glovebox.

The thermal stability for the tandem cells were tested by holding on a 65℃ hot plate in the dark in a N_2 glovebox without encapsulation. Photovoltaic performances were regularly measured when cooled down to room temperature. For the operational stability test, the encapsulated PSCs were continuously illuminated using white LED at 100 mW cm^{-2}. Test for NBG PSCs was in an N_2 atmosphere at ~40 ºC (illuminated heating); test for WBG PSCs was in ambient air with ~ 40 ºC (illuminated heating) and ~70% relative humidity. No UV filters or cooling setups applied for the tests above. For the NBG PSCs, the PCBM layer was replaced by C60 (35 nm) in the thermal stability and operational tracking tests. Storage stability for tandem cells were stored in N_2 atmosphere without encapsulation.

Absorption spectroscopy characterization

The UV-vis absorption spectra for thin films and layer stacks were recorded by a spectrophotometer (UH4150, Hitachi, Japan) with the background noise subtracted before testing. Based on the measured spectrum, an optical bandgap can be estimated using the following relation

$$\alpha\,(\mathrm{E}) \;=\; \mathrm{A}\,(\mathrm{E} - \mathrm{E}_g)^{1/2} \qquad (Equation\ 3.4)$$

where α(E) is the absorption coefficient, A is the constant for material. Based on this relation, E_g can be determined from the Tauc plot by plotting (αhν)2 against E in eV.[256] The Eg is estimated from the extrapolation of the linear region to the energy-axis intercept.

Time-resolved photoluminescence (TRPL) spectroscopy

The TRPL spectroscopy measurements were performed using time-correlated single photon counting by an Edinburgh Instruments FLS1000 photoluminescence spectrometer (Edinburg, UK). The pulsed laser with the excitation wavelength of 450 nm was used as the excitation source. The decay curves were fitted according to the formula $y = A_1 exp(-x1/\tau 1) + A_2 exp(-x2/\tau 2) + B$. Carrier lifetimes are calculated by the formula: $\tau_{ave} = \sum A_i \tau_i^2 / \sum A_i \tau_i$.

Photoelectron spectroscopic measurement

Thermo Scientific ESCALAB Xi^+ system was used to acquire the X-ray photoelectron spectroscopy (XPS), ultraviolet photoelectron spectroscopy (UPS), and the reflection electron energy loss spectroscopy (REELS) spectra. The apparatus was equipped with a monochromated Al target X-ray (1486.7 eV) and He UV light (22.12 eV) as the XPS and UPS excitation sources, respectively. The magnetic immersion lens was employed to enhance the collection of the photoelectron for XPS measurement. A −10.0 V bias was applied between samples and the spectrometer for UPS measurement. The pass energy was set as 20.0 and 1.0 eV, and the scanning step was set at 0.05 eV per step and 0.02 eV per step for XPS high-resolution and UPS spectra, respectively. An Ar ion raster size of 5 mm was applied to ensure the uniform region for XPS and UPS measurements. XPS and UPS spectra were recorded in the center of the sputtering spot. The data analysis was conducted by using the Avantage software package. REELS measurements were performed using a 1 keV electron beam with a pass energy of 6 eV. Argon-2000-atom gas cluster ion beam (GCIB) sputtering was performed using a cluster size of 2000 at 4 keV energy to obtain the depth profile data. All samples were transferred into the analysis chamber via a vacuum transfer module avoiding exposure to the air. Unless otherwise stated, the depth profiles were carried out by the GCIB sputtering technology,

with the parameters of 2000-cluster sizes at 4 keV ion energy. Ar^+ ion sputtering was used as a supplement to etch the hard materials, such as metal electrodes. The XPS, UPS and REELS were performed by Juntao Hu, Yunnan University. Nan Chen, Yunnan University also contributed into UPS measurement. **Fig. 3.1** demonstrates a typical UPS spectra where the work functions and valence band maximums (VBM) can be extracted with linear extrapolations of the secondary electron cutoffs and the leading edge of the valence band, respectively. Then the conduction band minimums (CBM) are determined if the material bandgap is known.

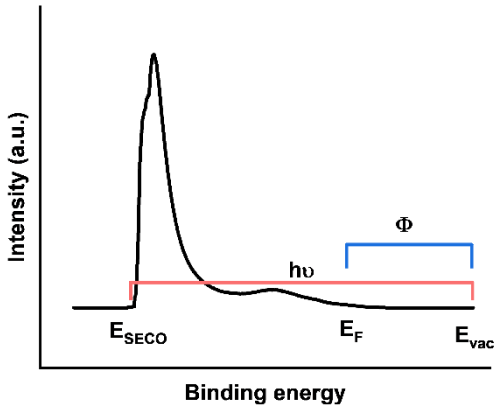


Fig. 3.1 A schematic for UPS spectra.

hν for the excitation energy, SECO for Secondary electron cut-off, E_F for Fermi energy, E_{VAC} for vacuum level, Φ for work function.

X-ray diffraction (XRD) characterization

The crystallographic information was characterized by the XRD instrument (D8 Discover, Burker) using 40 kV, 40 mA radiation (Cu Kα, λ = 0.15406 nm). Grazing incidence wide-angle X-ray scattering (GIWAXS) measurements were conducted at the BL17B1 beamline of Shanghai Synchrotron Radiation Facility (SSRF). The wavelength of X-ray was 1.240 Å with the grazing incident angle of 0.4 degree, and the

scattering intensity was detected by a PILATUS 2M detector. GIWAXS were performed by Shunde Li, PKU.

Scanning electron microscopy (SEM)

The field-emission scanning electron microscope (FE-SEM) was used to investigate the top-view and cross-sectional morphology with an accelerating voltage of 10 kV (Hitachi U8010). The SEM were performed by Peng Chen, Xiaoyu Yang and Hongyu Xu, PKU, and Juntao Hu, Yunnan University.

Atomic and Kelvin probe force microscopy (AFM, KPFM)

AFM topography of the perovskite surfaces was acquired by a scanning probe microscopy system (Veeco Innova SPM) under the tapping mode. The Kelvin probe force microscopy (KPFM) measurement was carried out in room dark conditions to quantify the surface potential variation in various surface terminations (Cypher VRS, Oxford Instruments). The AFM and KPFM were performed by Qiuyang Li, PKU. To characterize the surface potential using KPFM,[257] the following relation is used:

$$eV_{probe} = -eV_{CPD} = \Phi_{probe} - \Phi_{sample} \qquad (Equation\ 3.5)$$

where V_{probe} refers to the applied external bias, V_{CPD} refers to contact potential difference (CPD) between probes and samples, Φ_{probe} and $and\ \Phi_{sample}$ refer to the work function of probe tip and sample, respectively. When the probe tip is close enough to the sample, the electrical contact forms via tunnelling, where the Fermi levels will align through the electron current flow and upon equilibrium the applied bias has the same magnitude as the CPD with opposite direction. Thereby the work function of sample can be determined as the applied bias and the work function of probe tips are

known. As the work function of probe remains the same, the increase in the surface potential indicates the work function of sample decrease, implying the surface is more n-type as the Fermi level gets closer to the conduction band.

Transmission electron microscopy (TEM)

High-resolution transmission electron microscopy (HRTEM) and annular dark-field scanning transmission electron microscopy (ADF-STEM) images have been obtained by using a JEM-2100F field emission gun microscope with a 0.19 nm point-to-point resolution at 200 kV equipped with Energy disperse X-ray (EDX) detectors. Images have been analysed by means of Gatan Digital Micrograph software. To reduce the electron dose during the HRTEM characterization, the total electron beam exposure time was limited within 5 s. The TEM were measured by Juntao Hu, Yunnan University. The EDX were measured by Jingjing Wu, Yanping Sui and Pengyi Tang, SIMIT, Chinese Academy of Sciences.

3.4 Optical simulation

Modelling and numerical simulation methods have been regarded as powerful tools and integral parts to provide guidance in the device design and optimization, which is of importance for both single junction and TSCs. This section gives a brief introduction of optical simulation theory and method. The initial simulation code is taken from the publication[250] and massively modified for using in this thesis.

One main purpose of optical modelling is to calculate light absorption within the solar cells. For the traditional technologies e.g. silicon solar cells, a bulk semiconductor

material is used, of which the thickness is much larger than the wavelength of incident light in the interested spectrum. In this case, the light intensity experiences an exponential decay when propagating within the layers, which is described using a Beer-Lambert law as

$$\mathrm{I}(x) = I_0 \exp(-\alpha \mathrm{x}) \qquad (Equation\ 3.6)$$

where $I(x)$ is the light intensity at position x, I_0 is the incident light intensity, and α is the absorption coefficient. It is clear that the absorption is proportional to the intensity, which is a good assumption for bulk materials.

For thin film solar cells e.g. PSCs and OSCs, however, the Beer-Lambert law does not hold as they are so thin that the thickness is comparable to (normally less than) the incident light wavelength. Therefore the light can transmit through the absorber and reflect at the back opaque electrode, giving rise to strong interference and consequential non-monotonously changed internal intensity distribution. In 1999, Perttersson et al. applied the optical transfer matrix method (TMM) to describe light intensity distribution inside the OSCs, based on a one-dimensional model of several assumptions: all layers are isotropic and homogeneous; all interfaces are flat and parallel; the incident light is plane wave normal to the device substrate.[258]

The TMM is based on Fresnel equations as shown in **Fig. 3.2**.[259] A single-junction solar cell is modelled as a multi-layered structure (j = 0, 1, 2, …, m) between two semi-infinite layers (j = 0, j = m + 1) for thick substrate and air respectively. The optical properties of each layer are described by two optical constants i.e. refractive index n and extinction coefficient κ. Considering the thickness range of thin film solar cells, the light propagation can be treated coherently. When incident light transmits through from

left side, the reflected light (R) are generated at each interface, and the corresponding forward and backward optical electric fields are denoted as E_j^+ and E_j^- respectively. Due to the coherence, the interference effect occurs when the forward and backward waves with the same wavelength meet, indicating the TMM nature of wavelength-dependent. The light behavior at the interface between layer j and k can be described by a 2x2 matrix i.e. interface matrix I_{jk} containing the complex Fresnel coefficients, while another layer matrix L_j is used to describe light absorption and phase shift when propagating through the layer j. By considering all the layers and interfaces, the total transfer matrix S is generated to relate the electric field between the substrate (j = 0) and the air (j = m + 1). For an arbitrary point x in one layer j, the local electric field is the summation of two components:

$$E_j(x) = E_j^+(x) + E_j^-(x) \qquad (Equation\ 3.7)$$

By taking into account that transmission, reflection and two boundary conditions, the distribution of electric field $E_j(x)$ within one layer j can be derived. Afterwards, the time-averaged absorbed energy intensity i.e. energy dissipation $Q_j(x)$ per unit volume is calculated via $E_j(x)$ based on the concept of Poynting vector:

$$\mathrm{Q_j(x)} \propto \left|\mathrm{E_j(x)}\right|^2 \qquad (Equation\ 3.8)$$

For a working solar cell, the incident light includes the whole solar spectrum, so the actual energy dissipation $Q(x)$ is obtained by integrated over the interested wavelength range, usually from 350 nm to 900 nm as the strong absorption of glass substrate below 350 nm:

$$Q_j(x) = \int_{spectrum} Q_j(x,\lambda)\mathrm{d}\lambda \qquad (Equation\ 3.9)$$

Then the exciton generation profile can be derived from the energy dissipation, which

can be further integrated over the full wavelength range for the total exciton generation profile:

$$G_j(x,\lambda) = \frac{1}{\hbar\omega} Q_j(x,\lambda) \qquad \text{(Equation 3.10)}$$

$$G_j(x) = \int_{\text{spectrum}} G_j(x,\lambda)\,d\lambda \qquad \textit{(Equation 3.11)}$$

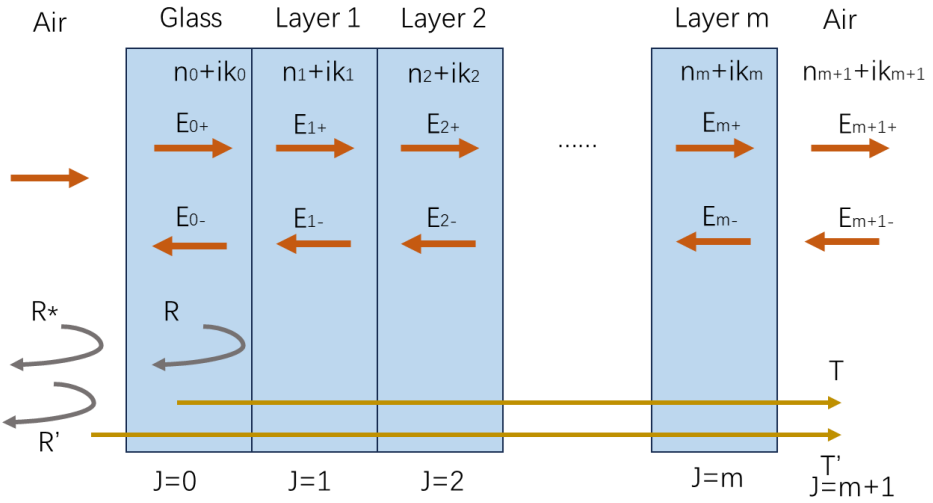


Fig. 3.2 Schematics of layered stacks described by transfer matrix method.

4. Geometric manipulation for efficient WBG PSCs

This chapter is adapted from the paper below, which is in preparation and will be submitted for publication.

Yun Xiao,[#] Fan Xu,[#] Xiaoyu Yang,[#] Peng Chen, Maotao Yu, Shunde Li, Qiuyang Li, Hongyu Xu, Lichen Zhao, Lei Li, Tinglu Song, Bin Liu, Rui Zhu and Henry J. Snaith.

Geometric Manipulation for Efficient Wide-Bandgap Perovskite Solar Cells.

[#]These authors contributed equally.

4.1 Abstract

WBG PSCs are essential candidate to pair with other NBG photovoltaic technologies for monolithic TSCs. Although substantial progress has been made in enhancing Voc, the significant FF deficit still limits the efficiency of WBG PSCs. Here, by manipulating the geometrical morphology of WBG perovskite films, a champion FF of 0.83 has been achieved in the hill-type PSCs with the best efficiency of 18.03% with a 1.77 eV bandgap perovskite. A moderate geometric fluctuation was proven to contribute to the electron extraction at the top interface of the WBG perovskite film. In addition, *in-situ* crystallographic and surface characterizations were employed to reveal the retarded crystallization kinetics of the hill-type perovskite, leading to the profitable geometrical morphology and enhanced device performance. It is anticipated this geometric manipulation strategy can contribute to the fabrication of efficient WBG PSCs for TSCs.

4.2 Introduction

WBG PSCs have attracted tremendous focus because of their great potentials as the sub-cell of TSCs.[121,204,227,229] So far, the efficiencies of all-perovskite and perovskite-Si TSCs have impressively reached 28.0% and 32.5%, respectively. [1,260] However, the performance of perovskite-based TSCs is still largely constrained by the WBG perovskite subcells because of the Voc loss and FF deficits.[149,211,261,262] Previous literatures suggest that the V_{OC}

loss is mainly due to the non-radiative recombination in the perovskite bulk and especially at the interfaces.[212,262–264] To enhance the V_{OC} of WBG PSCs, various strategies have been attempted, such as defect passivation at perovskite surface/bulk,[125,130,141,238] forming a 2D/3D perovskite heterostructure,[265,266] changing precursor compositions and anti-solvent conditions.[267–269] On the other hand, the FF of a solar cell device could be the most difficult and complicated parameter to be manipulated, as it can be influenced by multuplex factors e.g. charge recombination in the bulk and interfaces, poor contact between transporting layers and perovksites, leakage around the device edge.[270,271] Therefore, it is long challenging to improve the FF of WBG PSCs.

This work aims to make efficient WBG PSCs via a geometric manipulation strategy that improves both the carrier extraction and film quality. By controlling the film formation process, perovskite films with various geometric morphologies, i.e. mountain, hill and flat, were prepared. The geometric sizes and features were investigated by atomic force microscopy (AFM) and scanning electron microscopy (SEM). The photovoltaic performance of WBG PSCs indicates that hill-type devices showed the highest PCE and FF of 18.0% and 0.83 respectively using a 1.77 eV bandgap perovskite, which are much higher than mountain- and flat-type cells. Moreover, the hill-type perovskite film exhibits clearly slowed crystallization rates compared to the flat one, as revealed by the *in-situ* grazing-incidence wide angle X-ray scattering (GIWAXS) measurements, resulting in the

acquired profitable geometrical morphology and enhanced device performance. The results show that geometric manipulation strategy could be utilized to achieve efficient WBG PSCs.

4.3 Geometric manipulation

Perovskite films with different geometric features were prepared according to steps in **Section 3.2**, and were first characterized via microscopes. Based on their 3D topography results (**Fig. 4.1a**), the films were categorized into three types of flat, hill and mountain, respectively. The flat-type film shows a surface root mean square (RMS) of 19.7 nm, with no obvious bumpy region observed. The hill-type film exhibits a rougher surface (RMS=96.5 nm) than the flat one, with modest hilltops. In contrast, the film of mountain geometry exhibits the highest RMS of 255.7 nm with distinct amplitudes. The AFM topography results correspond well with the cross-sectional SEM images (**Fig. 4.1b**). In addition, no pinhole was detected at the perovskite films. It is noted that the film thickness are different for three types although the exact same precursor concentration was used. The possible explanation to this phenomenon may be attribuetd to the different wettability or viscosity as the results of the different routes to form three type films.

To investigate the effect of perovskite geometry on the deposition of ETLs, the PCBM as

the ETL were deposited on the top of three-type perovskite films, respectively, and top-view SEM images were provided. As illustrated in **Fig. 4.1c**, both flat and hill-type perovskite films are fully covered by PCBM layers, while only the valley parts of the mountain-type perovskite are partially covered, leaving a bare mountain top. The comparison suggests that PCBM layers can form comformal contact with the flat and hill-type perovskite films.

The schematic device models of three type films are presented in **Fig. 4.1d** . Apparently, the contact area between the perovskite layer and the ETL greatly increases when employing the hill and mountain geometries. Note that a large contact area between the perovskite layer and the ETL has been reported to improve the electron extraction, which is beneficial for achieving charge carrier balance in solar cells.[269,272,273] However, overlarge mountains with high surface roughness may further cause the poor coverage of the PCBM layer, which may induce undesired contact and thereby result in interfacial recombination that eventually deteriorates device efficiency.[274] Therefore, it is implied the hill geometry among the three types might be the optimal one for WBG PSCs.

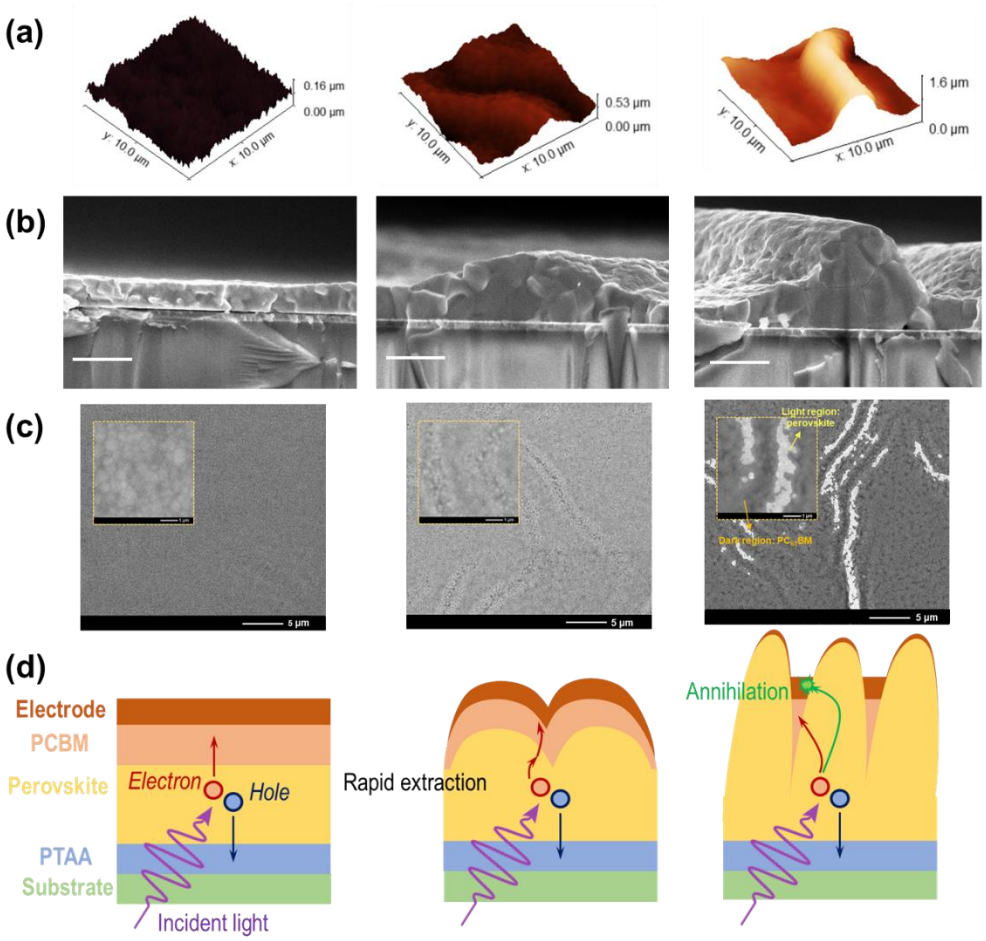


Fig. 4.1 Geometric morphology of perovskite films. Left: flat; Middle: hill; Right: mountain. **(a)** 3D topography results of perovskite films with different geometric features. The AFM were performed by Qiuyang Li, PKU. **(b)** Cross-sectional SEM images for perovskite films. Scale bar: 1μm. **(c)** Top-view SEM images of perovskites covered with additional PCBM as electron transporting layer, with white lines corresponding to the bared mountain top. Inset yellow rectangle: zoom-in image. The SEM were taken by Peng Chen, Xiaoyu Yang, Hongyu Xu, Peking University. **(d)** Schematic illustrations of the charge transport process in WBG PSCs with different geometric features.

4.4 Device performance with different geometries

In order to evaluate the effect of geometry on the device performance, full WBG PSCs were fabricated. The box charts presented in **Fig. 4.2a-d** compare photovoltaic parameters

of PSCs with mountain, hill, and flat geometries. The hill-type PSCs exhibited an average PCE of 17.3%, which is higher than that of flat- (14.6%) and mountain-type (13.9%) devices. Remarkedly, the hill-type cells showed a much better FF (0.83) than the other two types of devices (0.76 for flat and 0.68 for mountain), which indicates that the film geometry could significantly affect the device FF. Moreover, the hill-type PSCs demonstrate an enhancement in Voc (**Fig. 4.2c**), which can be ascribed to the efficient electron extraction and consequently suppressed interfacial recombination. It is noted that the various geometries have modest influences over Jsc (**Fig. 4.2d**). This can be possibly explained by that the geometries are formed at the back contact sides which have trivial contribution to the light trapping.[269]

The J-V curves for the champion devices of three geometries are shown in **Fig. 4.2e**, with the flat-, hill- and mountain-type PSCs exhibited PCE of 15.4%, 18.0% and 15.0%, respectively. Other PV parameters are summarized in **Table 4.1**. It is observed that among three types of geometry, the hill-type PSCs exhibited the best FF, V_{OC} and PCE. **Fig. 4.2e** inset demonstrates the steady-state power output (SPO) of hill-type PSCs tracking at the maximum power point under one sun illumination for 180s. External quantum efficiency (EQE) spectra and integrated Jsc of PSCs with different geometries are shown in **Fig. 4.2f**. It is observed that the integrated Jsc for mountain- and hill-type cells are slightly higher than that of the flat device. Some studies argued that the slight enhancement in Jsc could

be attributed to the formed geometries which possibly function as the textures and affect the light path,[275,276] while it may be also related to the thickened absorber films among three types (**Fig. 4.1b**). **Fig. 4.2g** summarizes the FF and Voc from the representative 1.75~1.8 eV WBG PSCs reported in the literatures. Remarkably, the hill-type WBG PSC in this work exhibited a well-balanced high FF and Voc among the statistics.

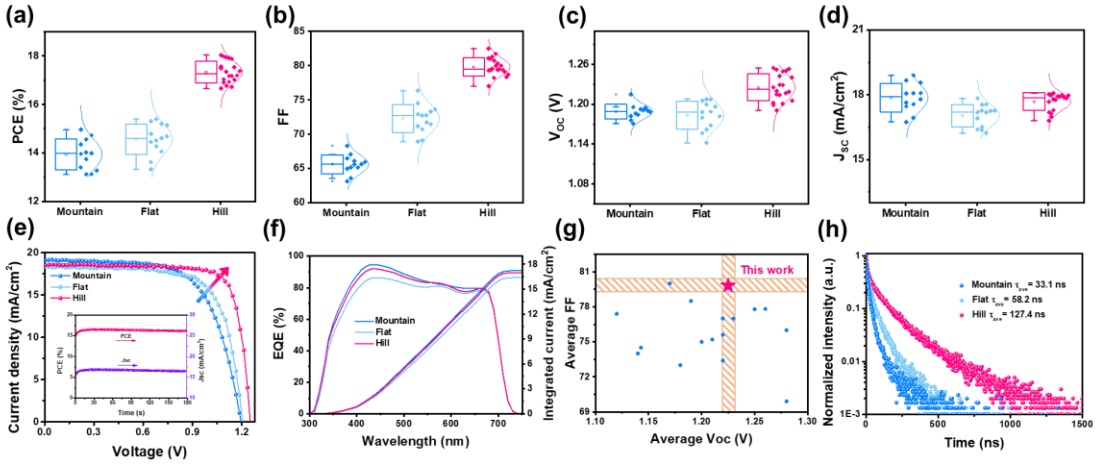


Fig. 4.2 Device performance of PSCs with different geometries.

(a-d) Statistics charts of PCE, FF, V_{OC}, and J_{SC} of mountain, flat, and hill WBG PSCs. **(e)** J-V curves for the best performance of mountain, flat and hill devices (inset: steady-state photocurrent measurement at the maximum power point of hill-type PSCs). **(f)** EQE measurements and the integrated J_{SC} of three type PSCs. The EQE were measured by Bin Liu, SUSTech. **(g)** Literature comparison between this work (denoted with a star) and other WBG PSCs with bandgap between 1.75 and 1.80 eV. **(h)** Time-resolved photoluminescence spectra of three type perovskite films on a ITO/PTAA glass substrate.

Table 4.1 Photovoltaic parameters of champion mountain-, flat- and hill-type WBG PSCs. Average values and standard deviations are based on 12, 12 and 20 devices for each.

Geometric type	Voc (V)	FF	Jsc (mA cm^{-2})	PCE (%)
Mountain	1.19 ± 0.01 (1.20)	0.65 ± 1.34 (0.65)	17.87 ± 0.63 (19.2)	13.9 ± 0.60 (15.0)
Flat	1.18 ± 0.02 (1.20)	0.72 ± 1.99 (0.75)	17.04 ± 0.49 (17.3)	14.6 ± 0.57 (15.4)
Hill	1.23 ± 0.02 (1.25)	0.80 ± 1.27 (0.80)	17.68 ± 0.39 (17.9)	17.3 ± 0.30 (18.0)

Moreover, the time-resolved photoluminescence (TRPL) measurements were carried out to study the non-radiative recombination loss in these films.[277] As shown in **Fig. 4.2h**, the data were fitted by a two-component exponential function. Different lifetime τ were then calculated and summarized in **Table 4.2**. The average carrier lifetime (τ_{ave}) of mountain-, flat- and hill-type films were determined to be 33.1 ns, 58.2 ns and 127.4 ns, respectively. This trend is consistent with one previous study which demonstrated that the hill sites with fewer defect density can extend carrier lifetime.[269] In addition, it is believed that the surface geometries is associated with the compressive stress relaxation.[268] Also it has been shown that, within certain range, increasing compressive strain could be beneficial to carrier transport.[278] Taking all these into account, it is speculated that the hill type perovskite with modest strain would not cause severe nonradiative recombination whereas facilitates the carrier transport while the flat and mountain type perovskites are out of the trade-off range.

Table 4.2 Fitted data for TRPL measurements.

Geometric type	A1	τ_1 (ns)	A2	τ_2 (ns)	τ_{ave} (ns)
Mountain	0.10	63.2	0.72	13.6	33.1
Hill	0.32	147.9	0.49	18.1	127.4
Flat	0.17	85.6	0.53	19.3	58.2

Next, the X-ray diffraction (XRD) measurement was conducted. As illustrated in **Fig. 4.3**, no new peaks or phase is found for the three types of films, indicating that the geometric manipulation has little effect on the perovskite composition.

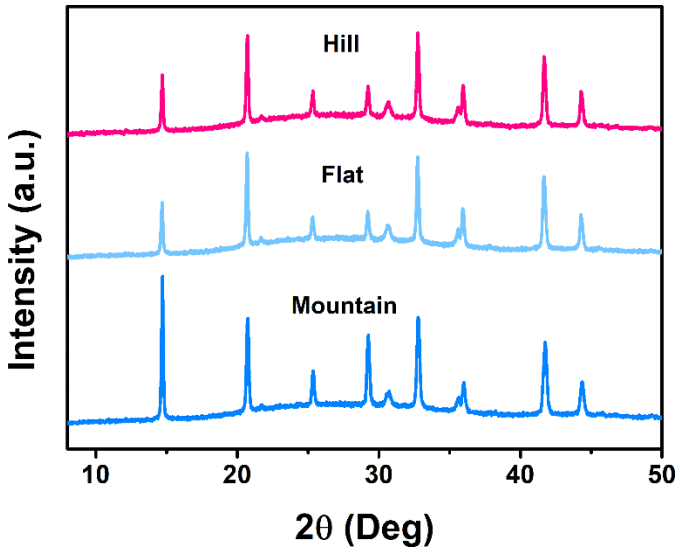


Fig. 4.3 XRD results of mountain, flat and hill perovskite thin films.

The Ultraviolet-visible (UV-vis) absorption results (**Fig. 4.4**) suggest that the film geometry will not vary the absorption onset while the geometries have slight enhancement in light absorption which could be attributed to either geometric textured morphology or thickened absorber films as discussed above (**Fig. 4.1b**).

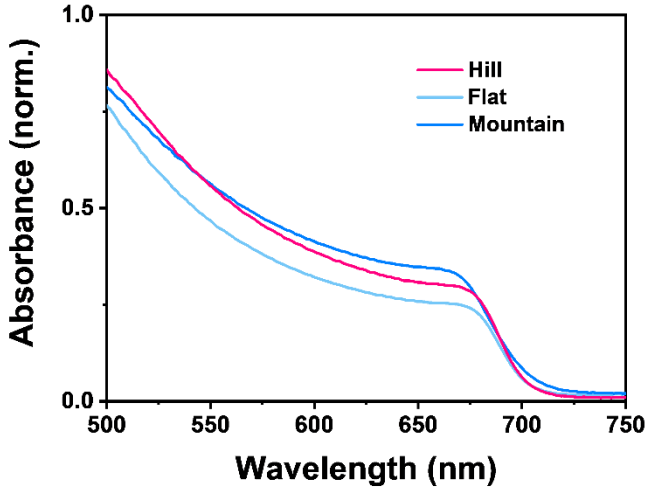


Fig. 4.4 UV-vis absorption results of mountain, flat and hill perovskite films.

4.5 Mechanism

The *in-situ* GIWAXS was employed to investigate the film crystallization kinetics, and the comparison was presented between the flat and hill perovskite films as they show better overall performance than the mountain type film, as shown in **Fig. 4.5a-b**. In the initial stage before 40s, the two type films present similar halo features from the as-cast precursor sol-gel colloids at low q values with peak around 4-5 nm^{-1}. While the antisolvent was dripped at 41s on the sol-gel colloids for both types, the flat and hill perovskites demonstrated distinct difference. The intense scattering features associated to the ordered perovskite phase are immediately formed in the flat type film, indicating the immediate collapse of the sol-gel colloidal state upon the addition of antisolvent and the fast crystallization process via phase transition.[279,280] In sharp contrast, this abrupt phase

transition is not found in the hill type film where the longevity of the sol-gel disordered state is extended by extra ~10s, exhibiting a slowed crystalization kinetics. The key GIWAXS profiles at specific times (t=40, 41s, 42s, 50s, 70s and 80s) are extracted in **Fig. 4.5c-d** . When reaching 41s, the arc at q=5 nm^{-1} vanished and two main new peaks at q=10.3 nm^{-1} and 14.6 nm^{-1} appeared in the flat-type film, which indicate the formation of perovskite crystalline phase. In contrast, no such peak occurred in the hill film until 50s.

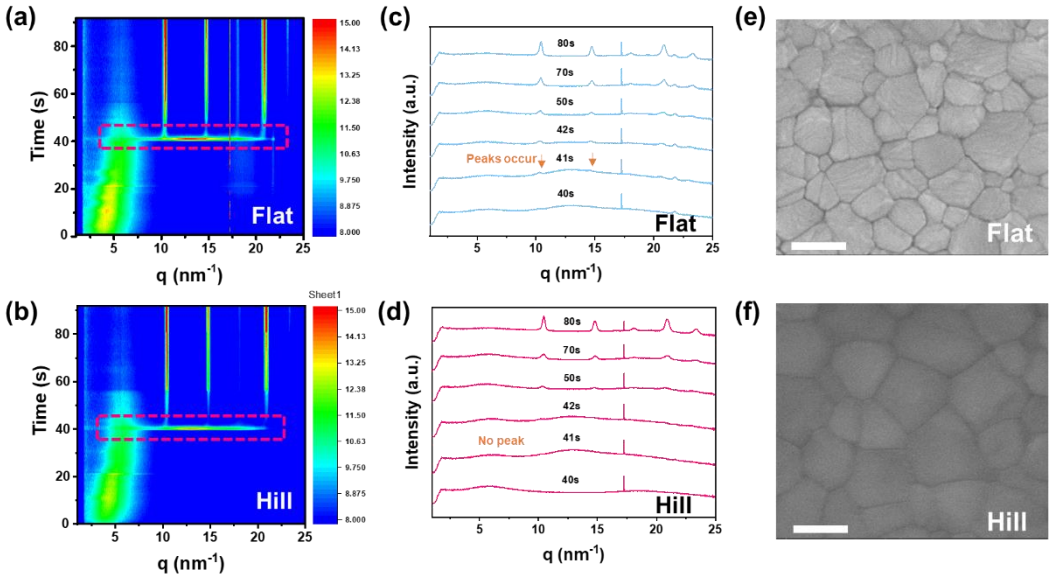


Fig. 4.5 Exploring the effects of geometric manipulation.

(a,b) Time-resolved GIWAXS intensity maps and **(c,d)** intensity profiles showing the structural evolution for **(a, c)** flat and **(b, d)** hill perovskite films. The red rectangles highlight the addition of antisolvent. The GIWAXS was performed by Shunde Li, Peking University. SEM images for **(e)** flat and **(f)** hill perovskite films. Scale bar: 300 nm. The SEM was performed by Peng Chen, Peking University.

It has been suggested that the quality of perovskite film is highly related to the crystallization kinetics.[268,279,281] As the antisolvent approach promotes the rapid

heterogeneous nucleation with high density of nucleation sites, as-induced crystal growth period is usually short, resulting in the polycrystalline perovskite films with small grain size, poor crystallinity and high densities of disorder.[282] In addition, the fast crystallization process brings the uncontrolled local microstrain.[283] It has been widely shown that the improved optoelectronic properties, in different perovskite compositions, are correlated to suppressed microstrain.[283–286] Thus it is clear that a slow crystallization process is desired for obtaining high-quality perovskite films. The SEM images (**Fig. 4.5e,f)** also demonstrate that the larger grain size is obtained in the slowed crystallization process. Technically, it also broadens the processing window of perovskite and facilitates the reproducibility. As described in the **Section 3.2**, the hill geometric morphology is related to the introduction of PFNBr on the top of HTL, in contrast to the flat type where no PFNBr was applied. It is deduced that the retarded crystallization process is related to PFNBr. As PFNBr is dissolvable in DMF solvent, the nitrogen lone pairs in PFNBr can strongly coordinate with Pb^{2+} via Lewis acid-base interaction when the perovskite precursor solution is deposited, which likely retards the collapse of precursor sol-gel state.[287] Therefore it is concluded that the hill-type perovskite is formed via an extended sol-gel state and a slowed crystallization process in contrast to the flat-type films, which is likely responsible for the larger grain size and longer carrier lifetime in hill-type PSCs.[288]

4.6 Conclusion

In this work, WBG perovskite films with mountain, hill and flat geometries were fabricated. It is found that manipulating the perovskite geometry can affect the device PV parameters, particularly on the FF, via mainly two points: 1) efficient electron extraction due to increased conformal contact area; 2) the slowed crystallization process for perovskite films provides high quality perovskite films with the improved optoelectronic properties. The hill-type WBG PSCs show the overall best photovoltaic performance, with PCE of 18.0% and FF of 0.83 using a 1.77 eV bandgap perovskite. However it is noted that the approach developed in this work with manipulated geometry may introduce the shunt risk when integrating into TSCs where WBG PSCs as the underlying subcells. Especially for POTSCs, the interconnecting layers are usually very thin (several to tens of nm), and the NBG organic absorbers prefer planar surface substrates. Therefore a route fabricating WBG perovskite with more flat morphology would be considered in the fabrication of POTSCs which will be discussed in **Chapter 6**.

5. Efficient and stable PSCs enabled by ytterbium oxide

This chapter is adapted from the paper below, which is in preparation and will be submitted for publication.

Peng Chen[#], **Yun Xiao[#]**, Juntao Hu[#], Deying Luo, Shunde Li, Rui Su, Pietro Caprioglio, Pascal Kaienburg, Xiaohan Jia, Nan Chen, Jingjing Wu, Yanping Sui, Pengyi Tang, Haoming Yan, Tianyu Huang, Maotao Yu, Qiuyang Li, Lichen Zhao, Dengke Wang, Xiaojun Li, Qing Zhao, Qihuang Gong, Zheng-Hong Lu, Henry J. Snaith, Rui Zhu. *Multifunctional ytterbium oxide buffer for perovskite solar cells.*

[#]These authors contribute equally.

5.1 Abstract

The buffer material between the ETL and the metal electrode is key to fabricating highly efficient and stable p-i-n PSCs. In addition to serving electronically for facilitating photocarriers from the ETL to the electrode, the buffer layer should also act as a barrier preventing e.g. the inter-diffusion of harmful species, such as ions, oxygen, moisture, between the electrode and the perovskite absorber. Here, a chemically stable buffer material, ytterbium oxide (Yb_2O_3), is reported for p-i-n PSCs via scalable physical vapor deposition (PVD). The broad applicability of Yb_2O_3 working with WBG, MBG and NBG perovskites has been demonstrated. Moreover, when subjected to thermal stress and light illumination, the Yb_2O_3-based PSCs demonstrate markedly enhanced device stability. This work paves a new avenue for the scalable fabrication of efficient and stable PSCs, pushing this promising photovoltaic technology closer to real-life application.

5.2 Introduction

In recent years, PSCs have witnessed an incredible development, due to the great potentials as the emerging cost-effective photovoltaic technologies.[130,216,254,289,290] Single-junction p-i-n PSCs have enabled the PCE of 25% through surface reaction, comparable to the n-i-p counterparts.[252,254] While the operational stability of p-i-n PSCs has been considerably enhanced *via* strategies such as additive engineering[291] and low-dimensional perovskite

passivation[292], it still remains a major challenge. As introduced in **Section 2.1**, ion migration represents a significant issue that probably leads to wide-range stability issues.[293–295] Electrical bias and illumination-backed ion migration within a perovskite absorber layer can inevitably vary the chemical composition on nano- and micro-scale,[291,293,295] consequently enhancing chemical heterogeneity and non-radiative recombination centers and subsequent initial sites where device degradation occurs.[212,296] In addition, the mobile ions from the perovskite absorber can travel through the ETL and then accumulate at the metal electrode interface, resulting in the corrsion of metal electrodes.[103,297] Another key concern for long-term instability is the metal atom migration from the electrode into the underneath ETLs and perovskite layers.[93,103] Attempting to introduce an effective buffer layer between the ETL and the metal electrode to block atom and ion movement between the perovskite and metal layers (in both directions) is of technological interest in improving overall device performance.[103,298,299] In this case, the buffer layer must form favourable band alignment between the ETLs and metal electrode, ensuring efficient electron collection in PSCs, to collect electrons across the metal electrode interface. The deposition process must not damage the underlying materials such as PCBM and C60, and be conformal with high throughput industrial fabrication. Moreover, an ideal buffer layer can effectively prevent the accumulation of the mobile ions at the metal electrode and inhibit oxygen and moisture permeation from the air. Bathocuproine (BCP) is one of the most widely used buffer material that can be processed with scalable thermal

evaporation within the p-i-n PSCs.[39,44,300,301] Unfortunately, BCP suffers from poor thermal stability under the protocol temperature of 85℃ by International Electrotechnical Commission (IEC), which prevents long-term operational stability.[291,292,302,303] Other commonly used oxides, including ZnO nanoparticles, compact SnO_2 layer, AZO nanoparticles have also been utilized as a buffer in p-i-n PSCs to replace the BCP. Yet, those oxides are either hard for large-scale fabrication or require time-consuming atomic-layer deposition, hindering large-scale practical application.

Herein, an intrinsically stable Yb_2O_3 is demonstrated as the buffer materials for efficient and stable p-i-n PSCs. The Yb_2O_3 buffer was employed into the p-i-n PSCs with a NBG 1.56 eV, a MBG 1.61 eV and a WBG 1.78 eV perovskite PSCs, and yielded a champion PCE of 24.8%, 22.1% and 20.1%, respectively. Compared with using the commonly used BCP, the devices with Yb_2O_3 show comparable efficiency. Moreover, the devices replacing BCP with Yb_2O_3 exhibit enhanced thermal stability when subjected to thermal stress in the dark. In addition, the NBG p-i-n PSC with the Yb_2O_3 buffer layer retains 97% of its initial efficiency in long-term operational stability assessment under continuous light illumination at ~40°C. The improvements in stabilities are attributed to the excellent stability of the Yb_2O_3 buffer layer itself and the role in inhibiting the negative impacts of ion migration in the metallization process. It is worth noting that the Yb_2O_3 buffer layer can be easily

manufactured with thermal PVD, which is promising for scalable processing.

5.3 Properties of ytterbium oxide

Fig. 5.1a illustrates the functions of an ideal buffer layer placed between the ETL and the metal electrode in p-i-n PSCs. From the comparison, the interfacial buffer layer with multifunctional roles is expected to ideally realize both efficient electron collection and to the prevention of cathode metal migration. However, the common buffer layer materials such as BCP and SnOx have proven challenging to meet these functions, hindering the discovery of cost-effective p-i-n PSCs with enhanced device efficiency and stability due to their inherent material properties and manufacturing process.

Ytterbium (Yb) is a common rare-earth element with a large atomic radius of 2.4 angstroms stacked as a face-centered cubic structure. As it is well known that a reaction is thermodynamically favored if the standard molar Gibbs free energy ($\Delta_f G$) is negative, the $\Delta_f G$ of an oxide formation can thus be used to predict whether an oxide is stable when it directly contacts a metal. Compared to other common metal oxides used as the buffer layer in p-i-n PSCs which are known to be reactive,[292,299,303] Yb_2O_3 presents the lowest $\Delta_f G$ of the formation of these oxides (**Fig. 5.1b**), demonstrating the difficulty of being reduced and thereby good chemical stability of Yb_2O_3.[304] In addition, notably, the Yb_2O_3 can be processed using upscaling thermal PVD approaches owing to its low evaporation

temperature of 736 K with a vapor pressure of 1 Pa [e.g., Cu (1509 K), Ag (1283 K), Au (1646 K)] (**Fig. 5.1c**). Moreover, it is noted that the price of Yb is approximately 1/50 of Ag,[305] implying a cost-effective feature. These superior material characteristics make Yb_2O_3 a promising candidate as a new buffer layer for efficient and stable p-i-n PSCs.

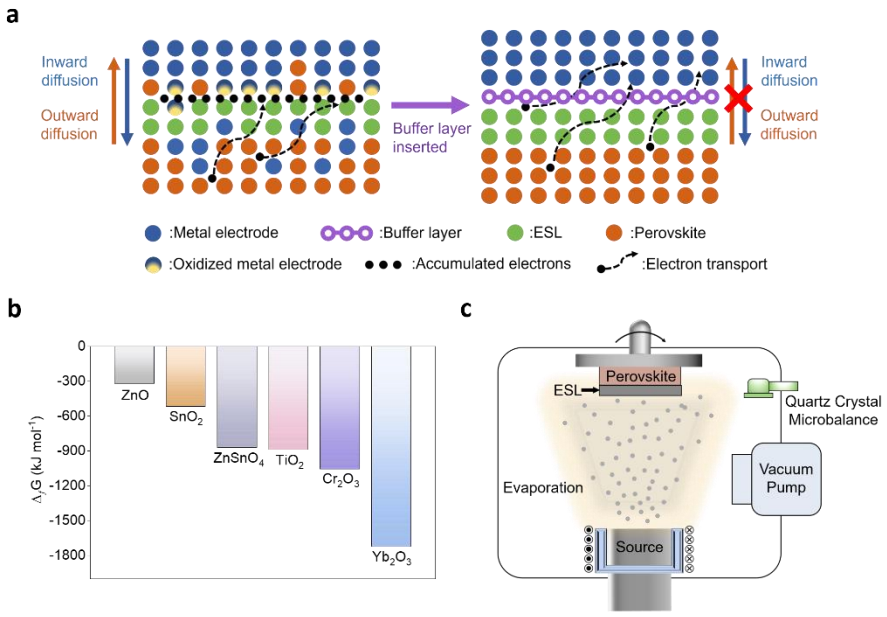


Fig. 5.1 Overview of buffer layers.

(a) Schematic illustration of the functions of an ideal buffer layer between the ETL and the metal electrode, showing suppression of the harmful species movement and the electron recombination. **(b)** Standard molar Gibbs free energy ($\Delta_f G$) of formation at 298.15 K in KJ mol^{-1} of representative metal oxides including ZnO, SnO_2, $ZnSnO_4$, TiO_2, Cr_2O_3, and Yb_2O_3.[345] **(c)** Schematic illustration of the thermally-evaporated deposition process of the Yb_2O_3 film.

To study the crystal structure and chemical and electronic properties of the Yb_2O_3 film, analysis was performed first based on TEM, XRD, and photoemission spectroscopy measurements. Yb_2O_3 was spontaneously formed via natural oxidation once the evaporated

Yb film was placed in an oxygen-rich or low vacuum environment.[306] The pure Yb film without being oxidized was initially investigated. **Fig. 5.2** shows the HRTEM images and the corresponding fast Fourier transform (FFT) patterns of the pure Yb film. The HRTEM images and FFT patterns feature the crystalline structure corresponding to a face-centered cubic system visualized from [011] direction in the red rectangle region.

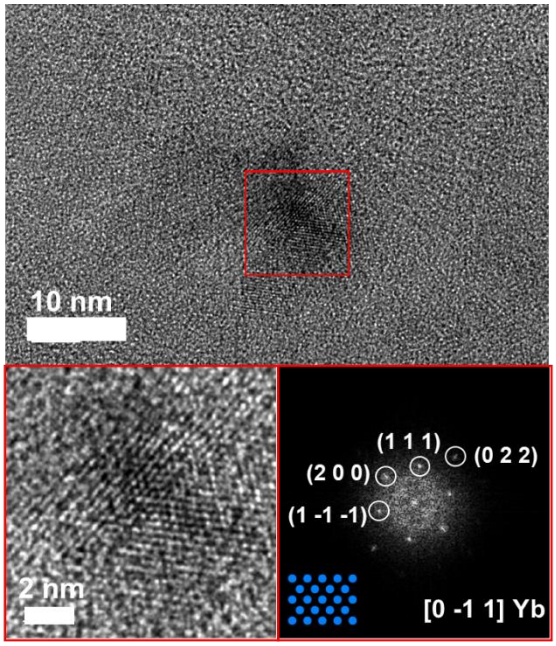


Fig. 5.2 Structural information for pure Yb film.
(a) HRTEM image of the pure Yb film. **(b)** The magnified HRTEM image and **(c)** the corresponding FFT patterns of the red squared area selected in **(a)**. The TEM, was measured by Juntao Hu, Yunnan University.

To examine the properties of as-evaporated Yb film, X-ray photoemission spectroscopy (XPS) was performed (**Fig. 5.3a-c**). Only Yb^{3+} 4d and O 1s signals were observed from the XPS data, suggesting that the evaporated metallic Yb is fully oxidized in the glovebox (O_2, <0.1 ppm). **Fig. 5.3d-e** show the easy and quick oxidation nature of polished ultraclean Yb

surface upon oxygen exposure.

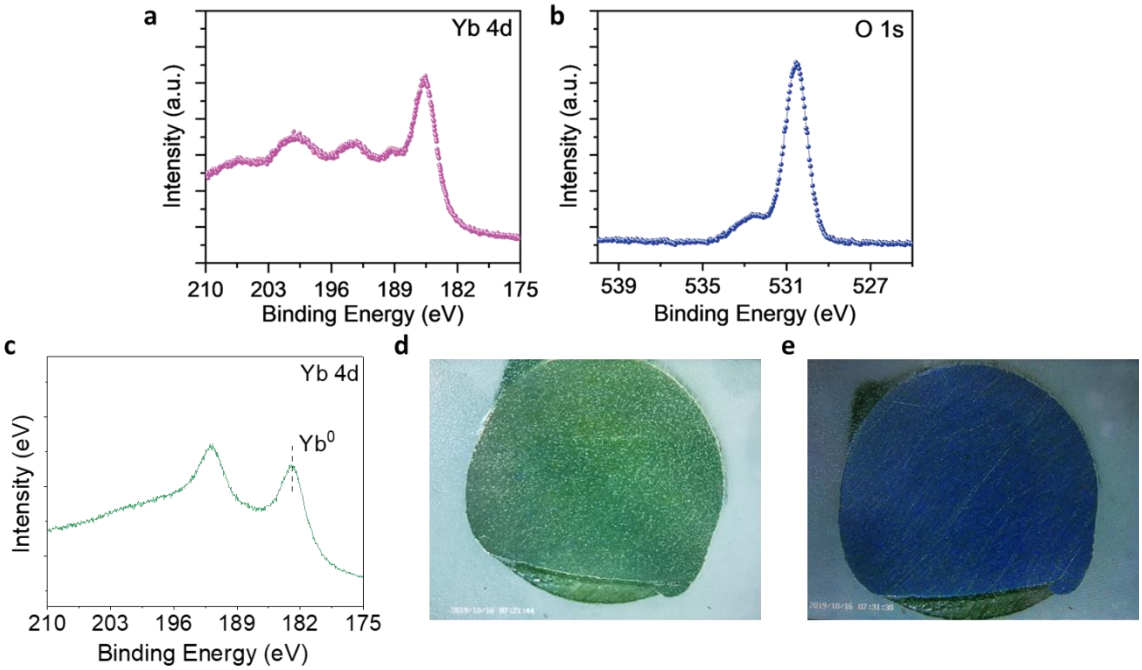


Fig. 5.3 X-ray photoemission spectroscopy (XPS) spectra of the as-evaporated Yb film.
Yb 4d XPS spectrum of **(a)** Yb^{3+} state,[346,347] **(b)** O 1s and **(c)** the Yb bulk etched by Ar ion for 2400s. Photographs of the pristine Yb bulk (diameter ~ 3mm) with **(d)** a naturally oxidized Yb_2O_3 surface and **(e)** the polished Yb bulk in the air. The color change indicates that the refreshed metal Yb surface would quickly react with oxygen upon oxygen exposure, resulting in formed Yb_2O_3 on the surface. The XPS and photographs were performed by Juntao Hu, Yunnan University.

The structural and morphological information of as-formed Yb_2O_3 were studied. The Yb_2O_3 film is amorphous as confirmed by TEM characterizations **(Fig. 5.4a-c**). The EDX chemical composition map for the Yb_2O_3 film suggests that the distribution of both Yb and O elements in the films is spatially homogeneous (**Fig. 5.4d-f**).

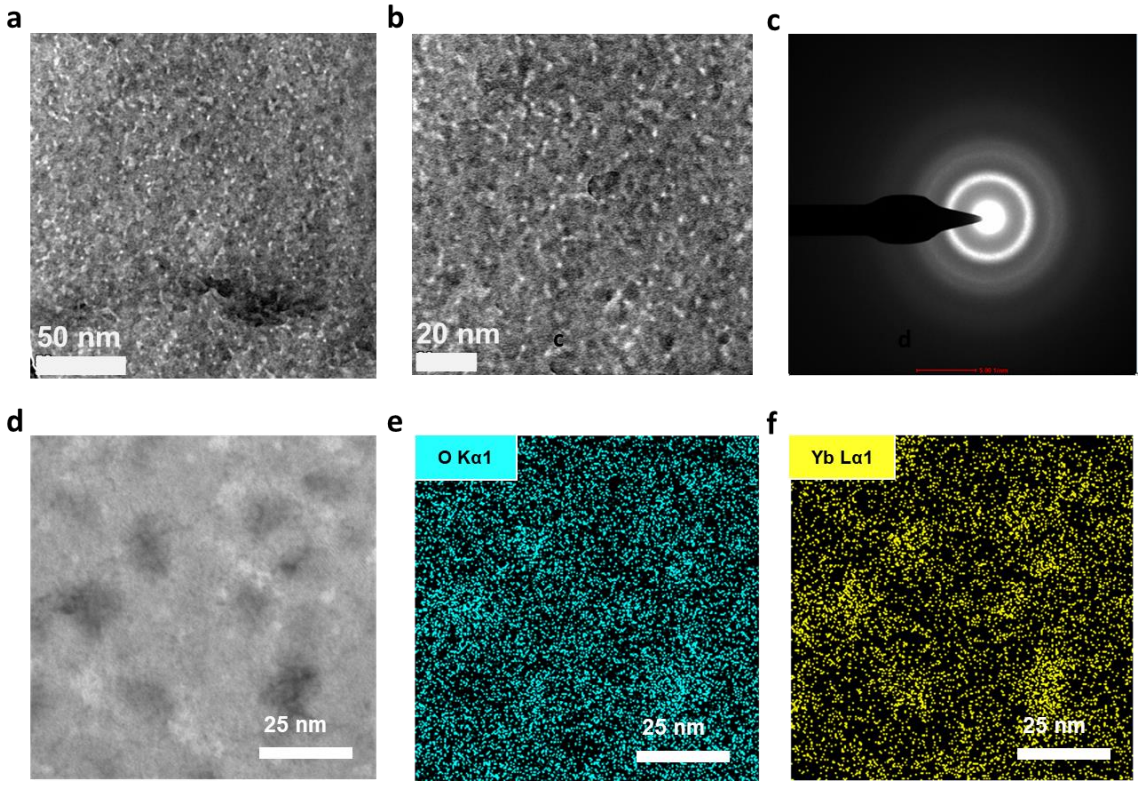


Fig. 5.4 Morphological information for Yb_2O_3 films.

(**a, b**) TEM images of Yb_2O_3 directly deposited on the carbon-supported copper (50 and 20 nm). (**c**) The corresponding FFT pattern indicates that the Yb_2O_3 is in an amorphous crystal structure. **(d)** High-angle annular dark-field scanning TEM (HAADF-STEM) images of the Yb_2O_3 deposited on the C60-coated carbon-supported copper grid. **(e,f)** Corresponding EDX chemical composition maps in a selected region. The TEM were measured by Juntao Hu, Yunnan University. The EDX were measured by Jingjing Wu, Yanping Sui and Pengyi Tang, SIMIT, Chinese Academy of Sciences.

The REELS show the surface bandgap of the Yb_2O_3 is 5.5 eV (**Fig. 5.5a**),[307] which is transparent to visible light wavelengths. The critical information associated with the electronic structure, including work function and valence band maximum, alongside conduction band minimum, proceeds to be quantified by combining UPS analyses (**Fig. 5.5b**) with the REELS data. These results suggest that the Yb_2O_3 film possesses an n-type

nature and has a low work function (**Fig. 5.5c**).

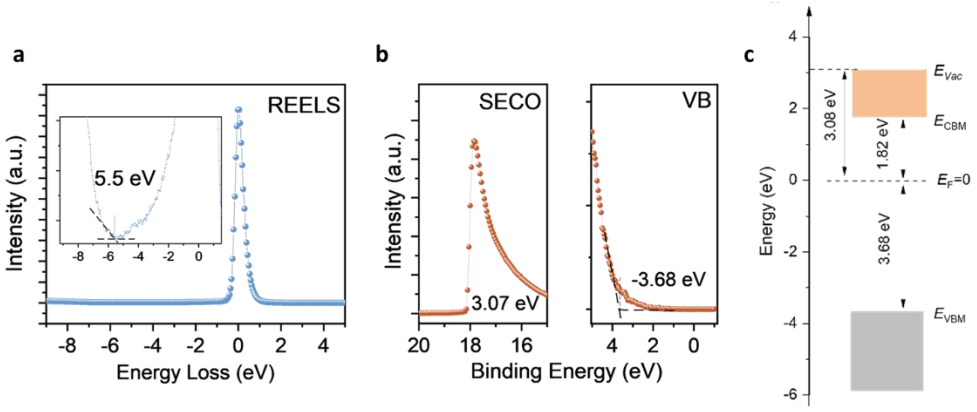


Fig. 5.5 Band structures for Yb_2O_3.

(a) The REELS of the Yb_2O_3 film. The inset shows how the band gap is determined.[348] **(b)** Ultraviolet photoelectron spectroscopy (UPS) spectra of the Yb_2O_3 film. Left, secondary electron cut-off (SECO) spectra. Right, valence band (VB) spectra. **(c)** Energy levels of the Yb_2O_3 film. Key parameters shown are E_{CBM} (conduction band minimum), E_{VBM} (valence band maximum), E_F (Fermi level) and E_{VAC} (vacuum level). The UPS, REELS were measured by Juntao Hu, Yunnan University.

5.4 The roles of ytterbium oxide at the interface

Fig. 5.6 shows XPS data on the variation of chemical constituents in the ETL and its interface with the metal electrode measured from samples (control) substrate/perovskite/C60/Cu and (target) substrate/perovskite/C60/Yb_2O_3/Cu, before and after ageing in the air (relative humidity, 80%) at 80°C for 5 h. A mechanical lift-off step was performed to delaminate the Cu electrode from the rest of the sample stacks[30], where the delaminated Cu is labelled as the "Cu" side, and the other is the "non-Cu" side, as shown in **Fig. 5.7** along with the SEM images of the delaminated surfaces of both control

and target samples. The buried organic C60 layer for the non-Cu side can be measured using gas cluster ion beam (GCIB) sputtering.

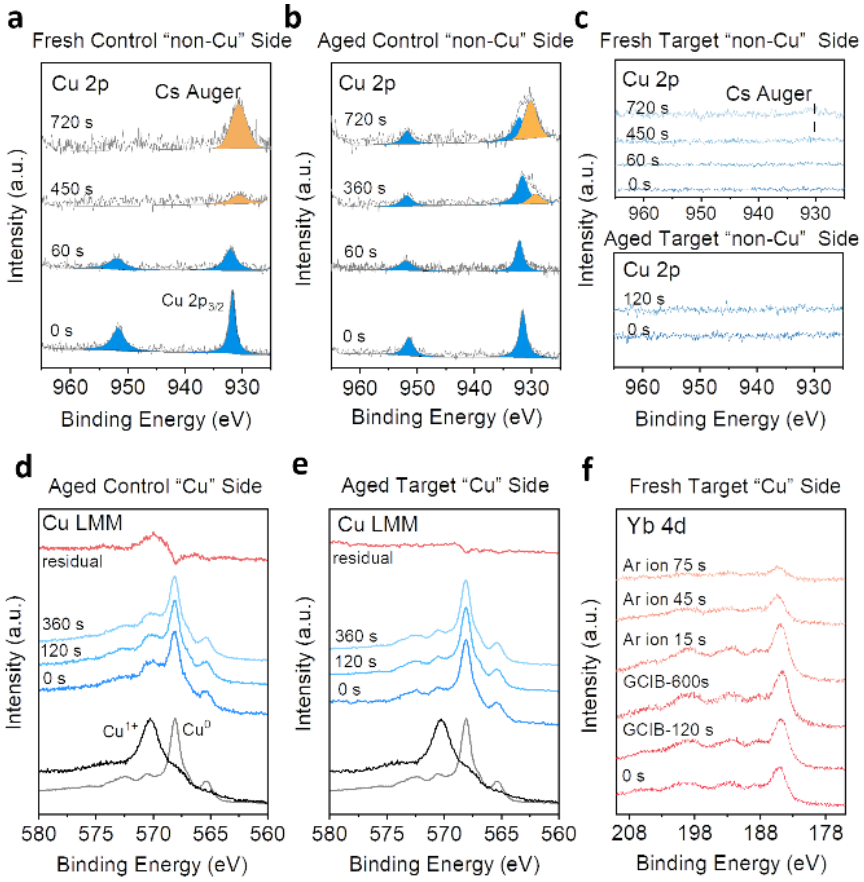


Fig. 5.6 Photoemission spectroscopy of the lift-off samples.

Cu 2p XPS depth profiling using GCIB sputtering (The sputtering rate for organic films is about 0.05 nm s^{-1} using *N,N′*-bis-(1-naphthyl)-*N,N′*-diphenyl-1,1' -biphenyl-4,4' -diamine (NPB) as the reference) detected at the non-Cu side of **(a)** the fresh control (without the Yb_2O_3) sample and **(b)** the aged control sampl`e without the Yb_2O_3 (after annealing at 80°C in the air for 5 h). Control: substrate/perovskite/C60/Cu. **(c)** Cu 2p XPS depth profiling detected at the non-Cu side of the fresh (up) and the aged (bottom) target samples (after annealing at 80°C in the air for 5 h). Cu LMM Auger spectra were detected at the aged Cu side of **(d)** the aged control sample and **(e)** the aged target sample (after thermal annealing at 80°C in the air for 5 h). The spectra difference (red line) [the as-delaminated spectrum (0 s, blue line) minus Cu^0 reference spectrum (black line)] is used to analyze chemical states.[296,304] Target: substrate/perovskite/C60/Yb_2O_3/Cu. **(f)** Yb 4d XPS depth profiling using GCIB/Ar ion sputtering measured at the non-Cu side of the fresh target sample with the Yb_2O_3. The XPS was performed by Juntao Hu, Yunnan University.

Fig. 5.6a-b shows the Cu 2p XPS depth profiling of the non-Cu sides before and after ageing. Note that the Cs Auger signal (highlighted in orange color) is used to indicate the perovskite layer. In **Fig. 5.6a,** there is a noticeable decrease in Cu 2p XPS peak intensity of the fresh control sample (i.e. without YbO_x) after the GCIB sputtering for 60. After 450s sputtering, the Cu 2p XPS peak almost disappears while Cs Auger signal is detected, indicating no massive Cu ions diffused into perovskite layers for the fresh control sample. In contrast, Cu 2p XPS peaks and Cs Auger signals are simultaneously detactable after 720s sputtering for the aged control samples (**Fig. 5.6b**), implying that Cu diffusion occurs in the aged control samples. When the Yb_2O_3 buffer layer is deposited between the C60 and Cu, the distribution of the Cu species into the C60 and perovskite underneath is not detected both fresh and aged target samples (**Fig. 5.6c)**. Thus, it is deduced that the Yb_2O_3 layer provides an effective barrier for the Cu migration between the perovskite and metal electrode.

Next, the chemical variation on the delaminated Cu surfaces of both control and target samples was probed by tracking the Cu LMM Auger of the delaminated Cu side. Note that to assist the analysis of the Auger peaks, the raw data has to minus the typical metallic Cu^0 spectrum to show Cu's chemical oxidation states qualitatively.[296,304] It is found that a peak

exists at around 571 eV on the aged control sample without Yb_2O_3 (**Fig. 5.6d-e**). This result indicates that Cu oxidation is happening in the aged control samples. However, the Cu oxidation peak is not observed in the aged target sample with Yb_2O_3 buffer. The chemical state of the Yb_2O_3 remains the same throughout the thickness by the XPS depth profiling (**Fig. 5.6f**). Photographs were taken to directly demonstrate the variation of metallic colors (**Fig. 5.8**).

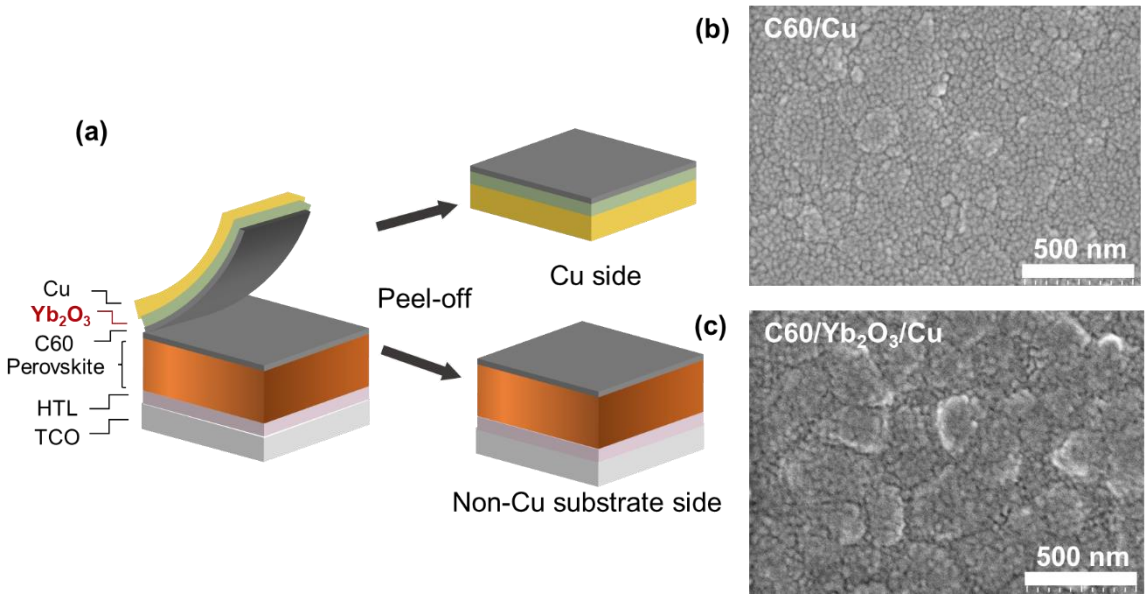


Fig. 5.7 (a) Schematics of lift-off samples. Top-view SEM images of the peeled-off samples: **(b)** C60/Cu and **(c)** C60/Yb_2O_3/Cu.

The SEM images were taken by Juntao Hu, Yunnan University.

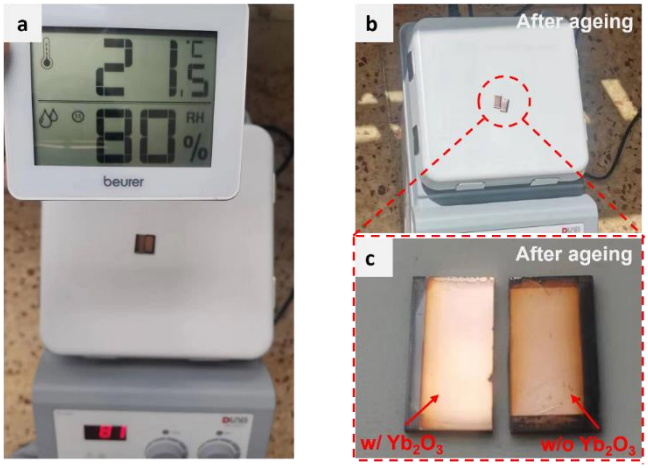


Fig. 5.8 Photographs showing the color variation of devices after the aging.

(a) Photograph of the ageing conditions for the unencapsulated devices with and without the Yb_2O_3 buffer layers. The devices were heated at 80°C in air [relative humidity of 80%]. **(b-c)** Photograph of the devices with and without Yb_2O_3 after ageing of 5 h. Photographs were taken by Juntao Hu, Yunnan University.

The band alignment across the metal electrode interface plays a critical role in efficient electron collection in p-i-n PSCs. Herein, based on the UPS depth profiling analysis on the Cu sides with and without Yb_2O_3, the band alignment across the C60/Cu and C60/Yb_2O_3/Cu interfaces was examined. The occurrence of electronic metal states near the Fermi level edge provides a good indicator for the removal of the organic C60 and C60/Y_2O_3 attached to the Cu electrode, as shown in **Fig. 5.9a, c** (insert). This is thereby used as the interface at which the underlying layer is transitioned to the metal Cu electrode. Then the band alignment across the C60/Cu and C60/Y_2O_3/Cu interfaces is established (**Fig. 5.9b, d**). The UPS spectral data show that band alignment favors electron flow to the metal electrode for both cases.

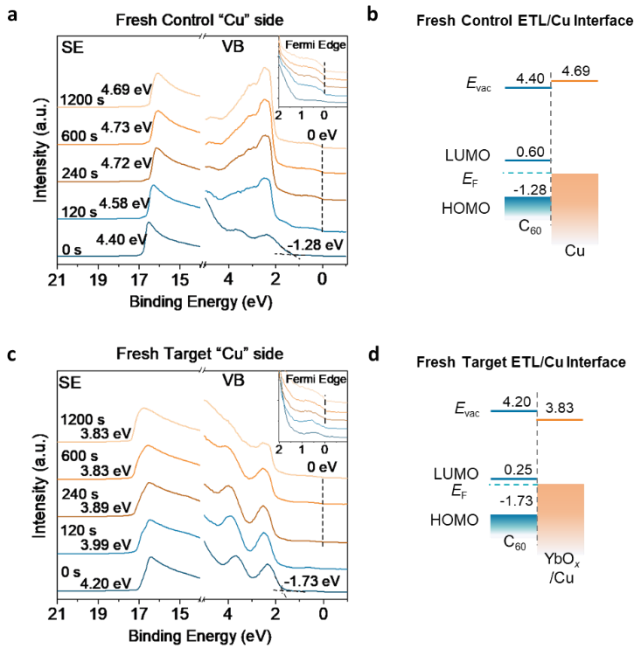


Fig. 5.9 UPS depth profiling was measured at the Cu-electrode side.

(a) the fresh control sample and **(c)** the fresh target sample. Energy band alignments of **(b)** the ETL/Cu interface of the fresh control sample and **(d)** the ETL/Yb_2O_3/Cu interface of the fresh target sample. The key parameters shown are HOMO (the highest occupied molecular orbitals) and LUMO (the lowest unoccupied molecular orbitals). UPS was performed by Juntao Hu, Yunnan University.

5.5 Device performance with universality verification

To assess the impact of the Yb_2O_3 buffer layer on device performance, full devices using perovskites with three different bandgaps were fabricated. The cross-sectional and top-view SEM images for those perovskites used in the devices are shown in **Fig. 5.10.**

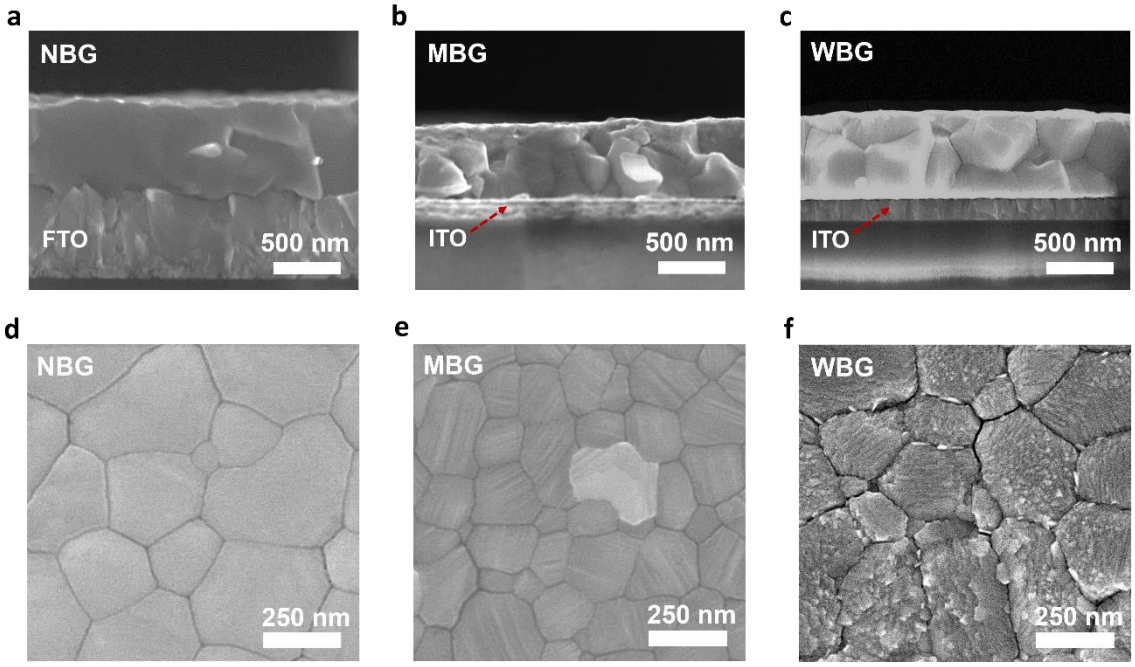


Fig. 5.10 SEM images for NBG, MBG and WBG perovskites.

(a-c) Cross-sectional SEM images of WBG, MBG and NBG perovskites deposited on the substrates used in the real PSCs. NBG: the glass/FTO/MeO-2PACz substrate. MBG: glass/ITO/PTAA substrate. WBG: glass/ITO/NiO_x/MeO-2PACz:2PACz substrate. **(d-f)** The corresponding Top-view SEM images. The SEM images were taken by Peng Chen, Peking University.

Fig. 5.11a displays the UV-vis absorption properties of the perovskites with various bandgaps. Tauc plots analysis was performed to estimate the perovskite bandgaps: 1.56 eV for NBG, 1.61 eV for MBG, and 1.78 eV for WBG perovskite, respectively (**Fig. 5.11b**). TRPL spectra were also measured to display the charge carrier properties in three type perovskite (**Fig. 5.11c**).

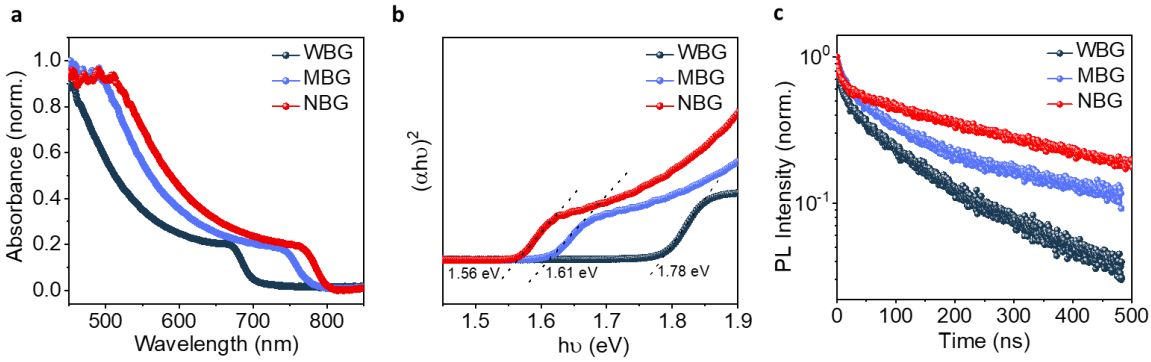


Fig. 5.11 Optoeletronic properties of perovskite films with differenct bandgaps.

(a) UV-vis absorption spectra and **(b)** the corresponding Tauc analyses of the WBG, MBG and NBG perovskites. **(c)** TRPL decays of the NBG, MBG and WBG perovskites deposited on the substrates used in real-world PSCs. NBG samples: glass/FTO/MeO-2PACz/perovskite; MBG samples: glass/ITO/PTAA/perovskite; WBG samples: glass/ITO/NiO_x/MeO-2PACz&2PACz/perovskite.

Fig. 5.12 provides the overall device performance of p-i-n PSCs with the Yb_2O_3 buffer layer in general. The device structure is consisted of substrate/HTL/perovskite/ETL/Yb_2O_3/Cu (**Fig. 5.12**a). The J-V scans, SPO results under AM1.5G irradiance one-sun illumination, and EQE for three bandgaps PSCs are shown in **Fig. 5.12b-d, g**, respectively, along with device parameters summarized in **Table 5.1**. The general device reproducibility regardless of perovskite bandgaps using the Yb_2O_3 buffer is demonstrated in **Fig. 5.12e**. The Voc obtained among three bandgaps are compared with representative reported values in **Fig. 5.12f**, which are close to or even surpass 90% of the radiative limit versus the bandgap energy.

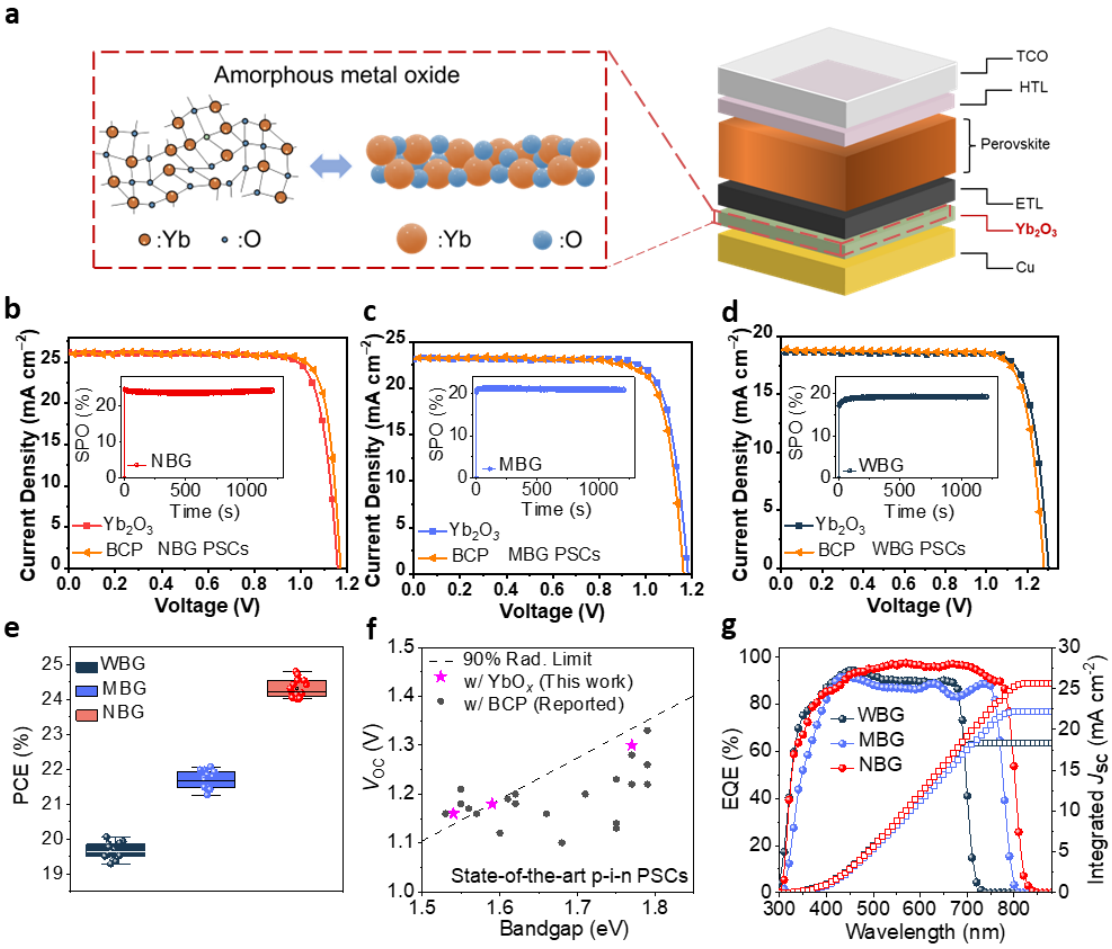


Fig. 5.12 Device structure and performance for NBG, MBG and WBG PSCs.

(a) Device configuration of a typical device with the Yb_2O_3 buffer layer. (**b-d**) The *J*–*V* scans of PSCs with three bandgaps for either Yb_2O_3 or BCP buffer layer and the steady-state power output (SPO) of these devices at the maximum power point under simulated AM 1.5 G illumination (inset). NBG, MBG, WBG. (**e**) PCE distributions for PSCs with NBG, MBG, and WBG bandgaps. The number of devices is 15 for each. (**f**) Comparison of the V_{OC} of state-of-the-art p-i-n PSCs with varied perovskite bandgaps. Note that the data from the literature is based on the p-i-n PSCs with BCP buffer layer. The dashed line represents 90% of the radiative limit with respect to the bandgap energy.[262] (**g**) The EQE spectra of the champion PSCs with NBG, MBG, and WBG perovskites, which were measured by Peng Chen, PKU.

Table 5.1 Summary of photovoltaic parameters for the NBG, MBG and WBG PSCs. Average values and standard deviation are calculated based on 15 devices.

Perovskite	Buffer		V_{OC} (V)	J_{SC} (mA cm^{-2})	FF	PCE (%)
WBG PSCs	Yb_2O_3	Avg	1.30 ± 0.01	18.5 ± 0.18	0.81 ± 1.55	19.7 ± 0.22
		(best)	(1.30)	(18.6)	(0.83)	(20.1)
	BCP	Avg	1.27 ± 0.02	18.5 ± 0.29	0.79 ± 2.00	19.0 ± 0.42
		(best)	(1.30)	(18.6)	(0.83)	(20.1)
MBG PSCs	Yb_2O_3	Avg	1.17 ± 0.01	23.2 ± 0.18	0.80 ± 0.01	21.7 ± 0.28
		(best)	(1.18)	(23.1)	(0.81)	(22.1)
	BCP	Avg	/	/	/	/
		(best)	(1.16)	(23.1)	(0.80)	(21.4)
NBG PSCs	Yb_2O_3	Avg	1.15 ± 0.01	25.9 ± 0.20	0.81 ± 1.02	24.3 ± 0.25
		(best)	(1.16)	(26.1)	(0.82)	(24.8)
	BCP	Avg	1.15 ± 0.01	25.9± 0.19	0.81 ± 1.49	24.4 ± 0.48
		(best)	(1.16)	(26.1)	(0.83)	(25.2)

For the NBG PSC device, a remarkable PCE of 24.8% [a V_{OC} of 1.16 V, a FF of 0.82, and a J_{SC} of 26.1 mA cm^{-2}] and a SPO of ~24.10% are achieved. A statistic analysis of device performances of the p-i-n PSCs with BCP or Yb_2O_3 was compared in **Fig. 5.13**. The comparable device parameters for p-i-n PSCs with BCP and Yb_2O_3 buffer layers indicate that the Yb_2O_3 can functionally replace the commonly used organic BCP.

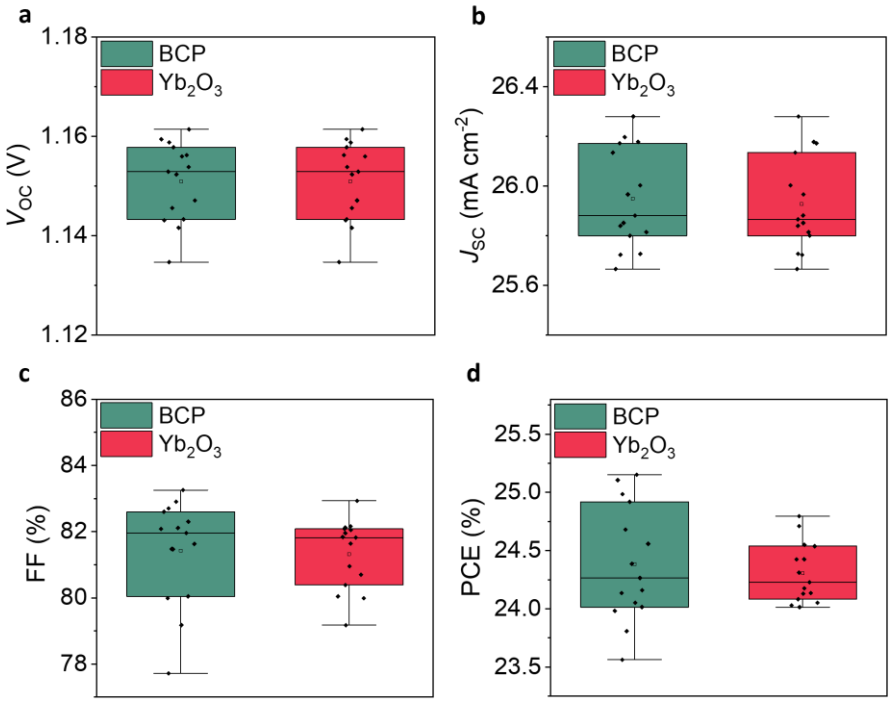


Fig. 5.13 Statistic comparison between NBG PSCs with BCP and Yb_2O_3. Comparison of V_{OC} (**a**), J_{SC} (**b**), FF (**c**), PCE (**d**).

For the MBG and WBG PSCs, a champion PCE of 22.1% (SPO of 20.7%) and 20.1% (SPO of 19.1%) were obtained, respectively. Compared to the WBG PSCs with BCP, the devices with Yb_2O_3 present slightly improved Voc, as shown in **Fig. 5.14**, which may be attributed to the better band alignment that waits for further exploration. Also, the WBG PSC has a V_{OC} of 1.30 V, a FF of 0.82 and a J_{SC} of 18.6 mA cm^{-2}, making it highly promising in TSCs which will be discussed in **Chapter 6**.

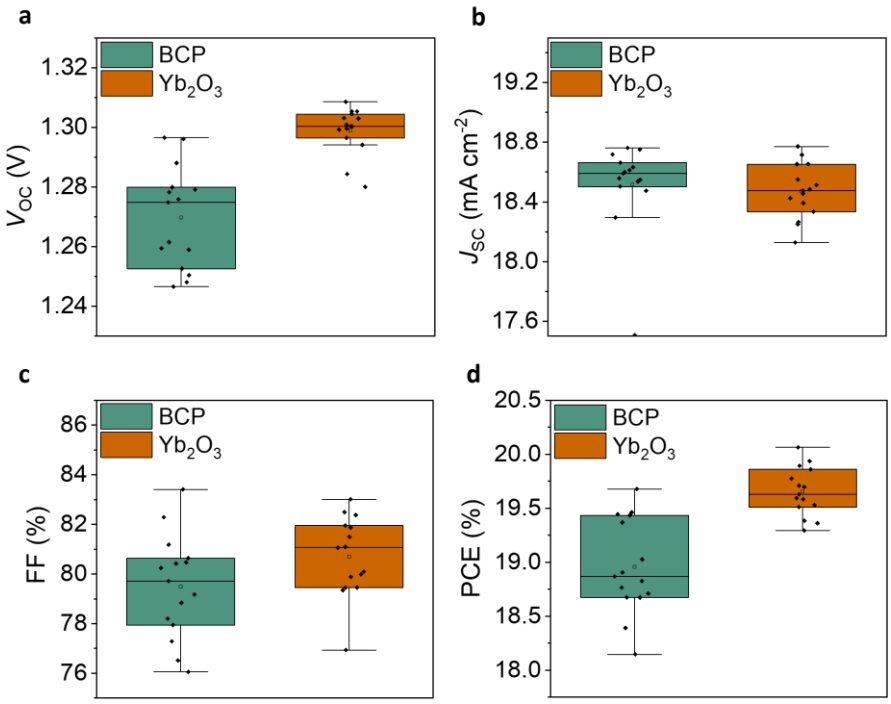


Fig. 5.14 Statistic comparison between WBG PSCs with BCP and Yb_2O_3. Comparison of V_{OC} (**a**), J_{SC} (**b**), FF (**c**), PCE (**d**).

Table 5.2 and **Table 5.3** summarize the representative state-of-the-art p-i-n NBG and WBG PSCs, respectively.

Table 5.2 Summary of representative efficient p-i-n NBG PSCs (1.53–1.56 eV) reported. SC = spin coating, PVD = physical vapor deposition, ALD = atomic layered deposition.

E_g (eV)	Buffer layer	Deposition method	V_{OC} (V)	J_{SC} (mA cm^{-2})	FF	PCE (%)	Ref.
1.56	Bphen	SC	1.16	24.6	0.82	23.3	308
1.56	BCP	SC	1.20	25.2	0.82	24.7	309
1.56	BCP	PVD	1.17	24.1	0.82	23.0	45
1.56	**Yb_2O_3**	**PVD**	**1.16**	**26.1**	**0.82**	**24.8**	**This work**
1.55	BCP	PVD	1.18	25.7	0.82	25.0	310
1.55	BCP	PVD	1.21	24.5	0.82	24.3	292
1.55	SnO_x	ALD	1.17	25.0	0.83	24.3	311

1.55	BCP	PVD	-	-	-	23.6	[292]
1.55	BCP	PVD	1.17	24.1	0.82	22.9	[312]
1.53	BCP	PVD	1.15	26.1	0.85	25.5	[254]
1.53	BCP	PVD	1.15	24.9	0.83	23.9	[49]

Table 5.3 Summary of representative efficient p-i-n WBG PSCs (1.75–1.80 eV) reported.

ALD=atomic layer deposition, PVD=physical vapor deposition

E_g (eV)	Buffer layer	Deposition method	V_{OC} (V)	J_{SC} (mA cm^{-2})	FF	PCE (%)	Ref.
1.79	BCP	PVD	1.26	17.4	0.80	17.7	[129]
1.79	SnO_x	ALD	1.33	17.3	0.84	19.3	[313]
1.79	BCP	PVD	1.26	17.9	0.79	17.8	[238]
1.78	**Yb_2O_3**	**PVD**	**1.30**	**18.6**	**0.83**	**20.1**	**This work**
1.77	BCP	PVD	1.26	18.1	0.80	18.3	[314]
1.77	BCP	PVD	1.22	-	~0.80	~17	[262]
1.77	BCP	PVD	1.28	17.2	0.80	17.7	[315]
1.77	BCP	PVD	1.22	17.0	0.80	16.5	[124]
1.77	BCP	PVD	1.22	17.4	0.82	17.3	[130,232]
1.77	SnO_x	ALD	1.21	17.1	0.77	15.9	[232]
1.75	BCP	PVD	1.32	18.7	0.82	20.3	[114]
1.75	SnO_x	ALD	1.23	17.5	0.80	17.1	[236]
1.75	BCP	PVD	1.14	16.4	0.75	14.0	[230]

As V_{OC} is a key parameter that is related to the non-radiative recombination,[44,212,262,263,316] EQE of EL (EQE_{EL}) analysis are performed for NBG and WBG PSCs to evaluate the Voc loss (**Fig. 5.15**). The EQE_{EL} of 5.12% was obtained for the NBG PSCs with a nearly flat EQE_{EL} for 30−100 mA cm^{-2} injection current. For the WBG PSCs, a peak EQE_{EL} of 0.97% is observed, and the PSCs emit bright red light under a 2.5 V forward bias.

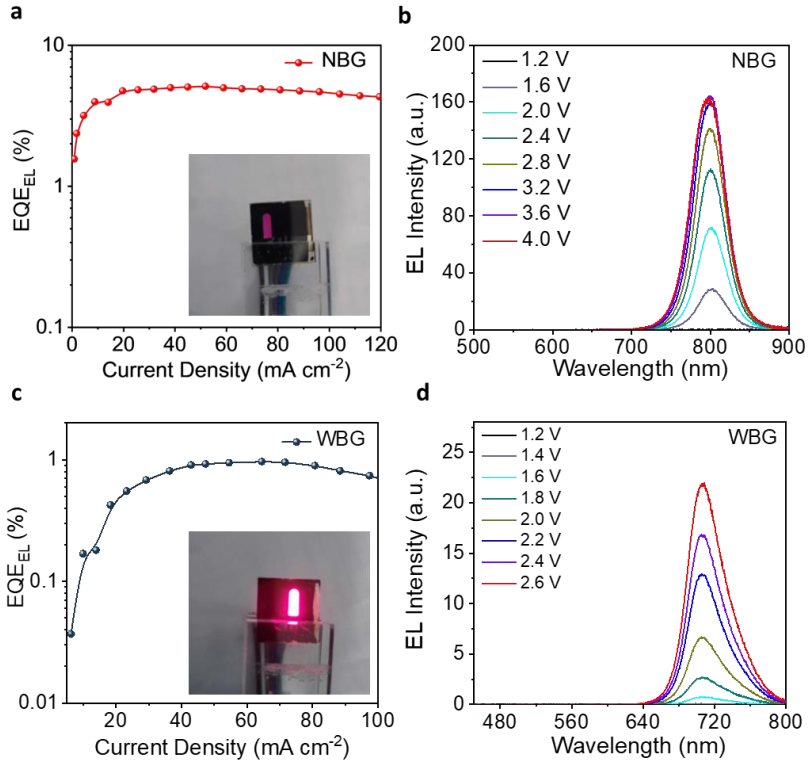


Fig. 5.15 EQE of EL for NBG and WBG PSCs.

The EQE_{EL} as a function of the injected current density for the NBG (**a**) and WBG (**c**) PSCs. Inset: the photograph of the NBG and WBG devices under a bias ~2.5 V. Room-temperature EL spectra of the NBG (**b**) and WBG (**d**) PSCs under the different bias operating as a light-emitting diode (LED). The EL were measured by Peng Chen and Maotao Yu, Peking University.

The calculation of QFLS values provides benchmark for evalutating device performance. Based on the EQE_{EL} values at injection condition equal to one sun illumination, the QFLS values of the perovskite absorber can be extracted (details in **Section 3.3**). The radiative V_{OC} of perovskite absorbers can be calculated using Equation 3.3 (**Section 3.3**).

$$QFLS_{,\mathrm{rad\ WG}} = \frac{k_B T}{q} \ln\left(\frac{J_{SC}}{J_{0,\mathrm{rad}}}\right) = 1.494\ V \qquad \text{(Equation 5.4)}$$

$$QFLS_{,\mathrm{rad\ NG}} = \frac{k_B T}{q} \ln\left(\frac{J_{SC}}{J_{0,\mathrm{rad}}}\right) = 1.279\ V \qquad \text{(Equation 5.5)}$$

By using the EQE_{EL} at the same injection condition as one sun equivalent measured for each different bandgap, it is possible to calculate the device QFLS, hence V_{OC}, with respect to the radiative QFLS potential

$$QFLS_{\mathrm{WG},} = QFLS_{,\mathrm{rad\ WG}} + \frac{k_B T}{q}\ln\left(EQE_{\mathrm{EL,WG}}\right) = 1.298\ eV \quad \text{(Equation 5.6)}$$

$$QFLS_{\mathrm{NG},} = QFLS_{,\mathrm{rad\ NG}} + \frac{k_B T}{q}\ln\left(EQE_{\mathrm{EL,NG}}\right) = 1.159\ eV \quad \text{(Equation 5.7)}$$

The calculated 1.298 eV for WBG PSCs and 1.159 eV for NBG PSCs, respectively, reach the 87% and 90% of corresponding radiative limits, indicating high Voc are achieved which are also in good agreement with that from the J−V scans.

5.6 Device stability and conclusions

To assess the impact of the Yb_2O_3 buffer layer on the device stability, the PSCs with BCP and Yb_2O_3 was firstly tested subjected to thermal stress. For the thermal stability test, all devices were encapsulated using glass covers sealed by epoxy resin. And the encapsulated PSCs were placed on a hotplate (at 85°C) in the dark in a N_2 glovebox. **Fig. 5.16a** compares results for the thermal stability of the NBG PSCs with BCP and Yb_2O_3 buffer layers. The PSCs with the Yb_2O_3 buffer layer exhibit a slight increase in the PCEs initially (<100 h) and retain 98% of its initial PCE (i.e., 21.1%) after the test period of 500 h. By contrast, the NBG PSCs with BCP show a sharp PCE drop upon exerting thermal stress. Only 82% of its initial PCE can be obtained after 500 h. The similar trend for the NBG PSCs is also

observed in the WBG PSCs (**Fig. 5.16b**). However, the WBG PSCs with both BCP and Yb_2O_3 buffer layers degrade at faster rates than those of the NBG PSCs, which is attributed to the inherently poor stability of the WBG perovskite.[317,318] Nonetheless, the WBG PSCs with Yb_2O_3 still retain 80% of its initial PCE after 500 h, whereas the one with BCP drops quickly to 75% in the initial 24 h and retains around 57% of initial performance.

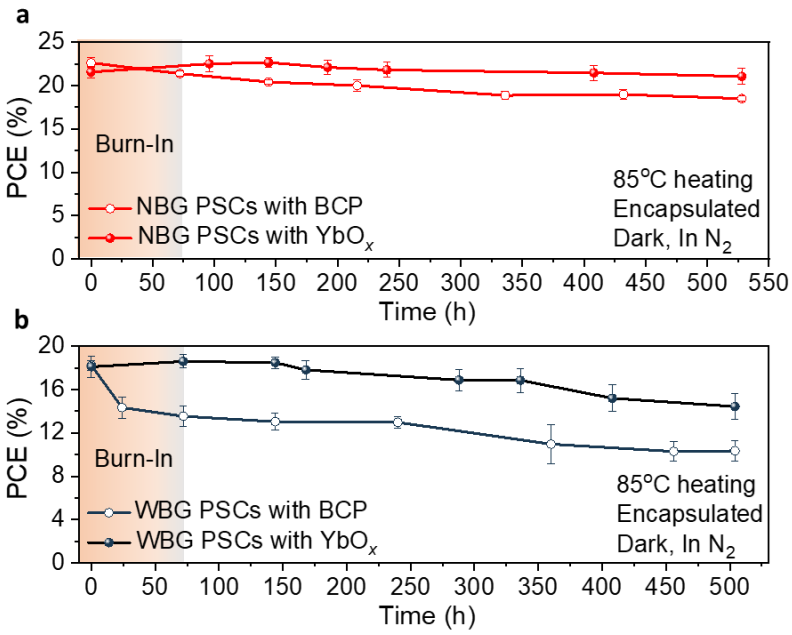


Fig. 5.16 Thermal stability tests for the encapsulated (**a**) NBG and (**b**) WBG PSCs with the BCP or Yb_2O_3 buffer layers in the N_2 glove box under 85°C in the dark.

The KPFM is used to characterize the surface potential. As evidenced in **Fig. 5.17**, the sample shows enhanced surface potential with Yb_2O_3 that further increases after heating. The increase in surface potentials indicates a more n-type nature as introduced in **Section 3.3**, which may facilitate carrier transport, and thereby contributing to the improved PCEs

during the initial ageing period.[48,319]

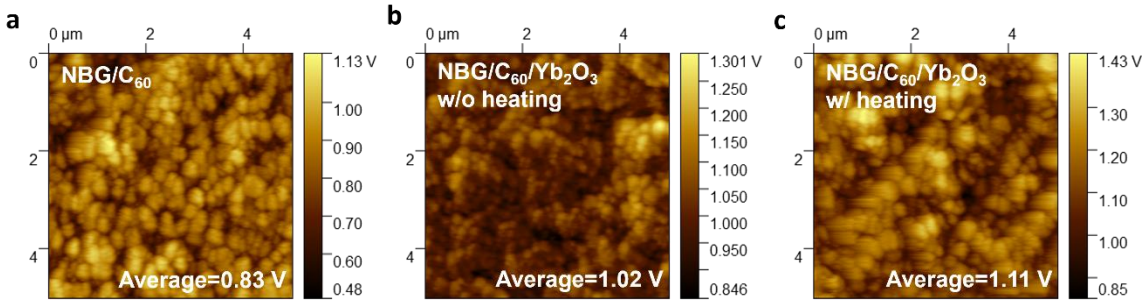


Fig. 5.17 KPFM images showing the surface potential difference.

The NBG/C60 samples (**a**) NBG/C60/Yb_2O_3 samples without heating at 80°C in the ambient environment (**b**) and NBG/C60/Yb_2O_3 samples with heating at 80°C in the ambient environment (**c**) on the FTO/MeO-2PACz substrate. The KPFM were measured by Qiuyang Li, Peking University.

Then the operational stability was also examined for NBG and WBG PSCs with Yb_2O_3/BCP under continous illumination (**Fig. 5.18**). The encapsulated cells were continuously illuminated by a white LED array with an intensity of 100 mW cm^{-2} without any cooling. The most stable NBG PSC with Yb_2O_3 keeps its initial performance for 800 h and still maintains 97% of the initial PCE after 1000 h. In comparison, the NBG PSC with BCP drops quickly to 96% of the initial PCE after 213 h. In light of the temperature under test here is about 40°C, which is lower than the actual outdoor working temperature (especially in summer season),[320] it is reasonable to deduce that the cells with the BCP buffer drop more quickly in the real operational condition than the current testing situation. The WBG PSCs demonstrates much poorer stability than NBG PSCs given the fact that WBG PSCs were tested in ambient air with high relative humidity ~70%. Still, it is clearly

evidenced that the cell with Yb_2O_3 showed improved stability over the one with BCP. The two comparisons indicate that the PSCs with the Yb_2O_3 buffer show more substantial resistance to thermal stress than the BCP ones, which is consistent with the observation above. The rapid thermal degradation in the dark and under light illumination (~40°C by illuminated heating) for the PSCs with BCP is attributed to the inherently thermal instability of the buffer layer in the PSCs, which is largely alleviated in the PSCs with Yb_2O_3 buffer layer.

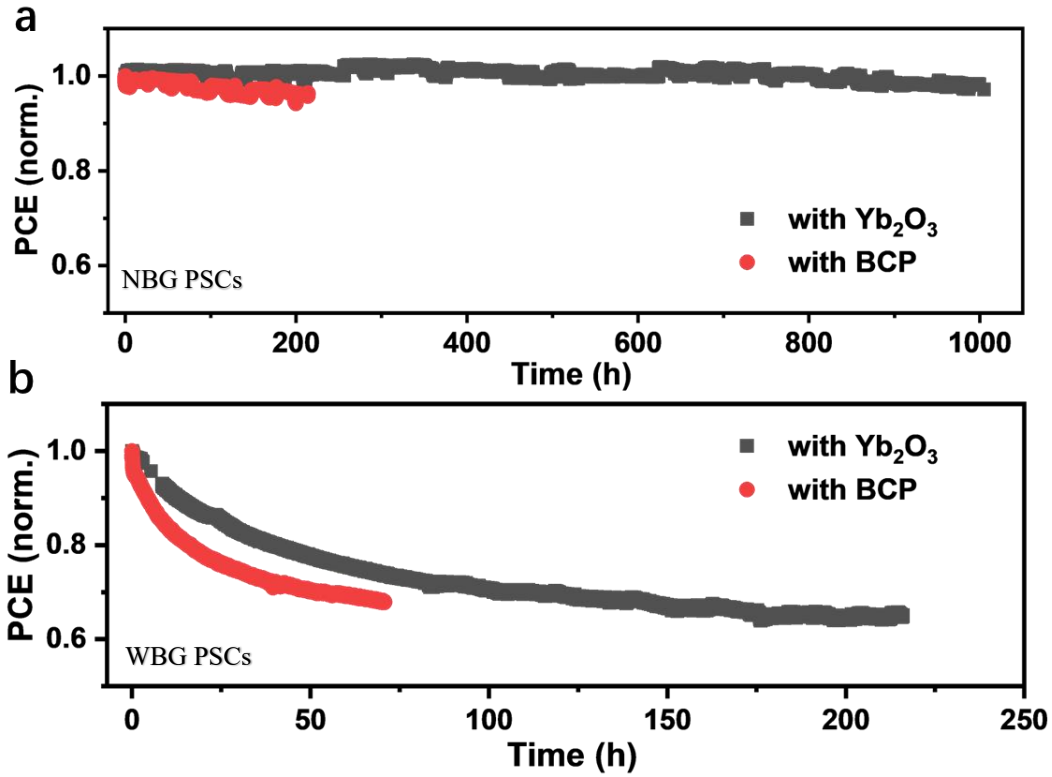


Fig. 5.18 Operational stability test for (**a**) NBG and (**b**) WBG PSCs.

Normalized maximum power point tracking (MPPT) curves of the encapsulated PSC under continuous illumination using white LED at 100 mW cm^{-2}. Test for NBG PSCs was in an N_2 atmosphere at about 40°C; test for WBG PSCs was in ambient air with ~ 40°C and ~70% relative humidity. No UV filters applied.

The chemical inertness of the Yb_2O_3 layer in the PSCs was further demonstrated by tracking the distribution of various chemical constituents when the Yb_2O_3 is directly deposited on the perovskite. As shown in **Fig. 5.19a-b**, it is found that both Pb 4f and I 3d XPS spectra of the control (without Yb_2O_3) and target samples (with Yb_2O_3) show consistent characteristic peaks assigned to I and Pb. However, the XPS intensity of the control sample is relatively higher than that of the target sample. The weak XPS intensity for the target sample results from adding Yb_2O_3, which may fluctuate X-ray absorption by the perovskite absorber. Pb 4f and I 3d XPS spectra vary a little after 25 days, indicating that the Yb_2O_3 is chemically unreactive with the perovskites. This means that out-diffused species from the perovskite absorbers will not react with the buffer layer, as further confirmed by the consistency of Yb 4d signal (**Fig. 5.19c**). Thus, the Yb_2O_3 is chemically inert and responsible for enhanced device stability.

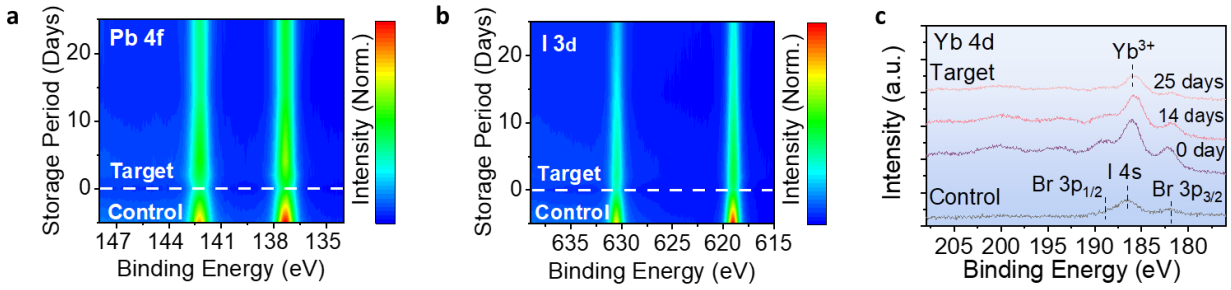


Fig. 5.19 The chemical inertness of the Yb_2O_3 layer in the PSCs.

(a-c) Evolutions of Pb 4f, I 3d, and Yb 3d XPS peaks of perovskite/Yb_2O_3 bilayers (target sample) against storage period in N_2-filled glovebox. Control: perovskite without the Yb_2O_3. The XPS were measured by Juntao Hu, Yunnan University.

In conclusion, this work demonstrates that Yb_2O_3 is able to provide good device performance for three different bandgap perovskites and enhance the device stability, implying its promise for application as the buffer material from various evaluations (**Fig. 5.20** Qualitative comparison for Yb_2O_3, BCP and SnO_x based on literatures.[33,301,321–323]).

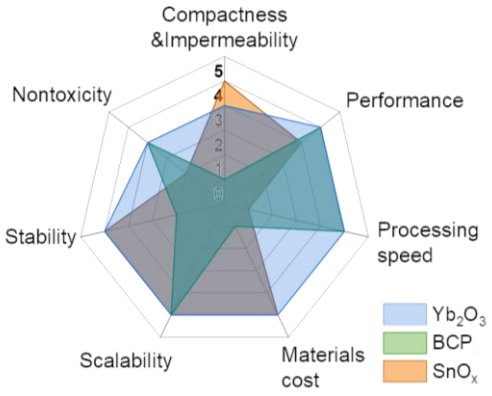


Fig. 5.20 Qualitative comparison for Yb_2O_3, BCP and SnO_x based on literatures.[33,301,321–323]

6. Yb_2O_3-based interconnecting layers for monolithic POTSCs

This chapter is adapted from the paper below, which is in preparation and will be submitted for publication.

Yun Xiao[#], Peng Chen[#], Xiaohan Jia[#], Nan Chen, Deying Luo, Juntao Hu, Hongyu Xu, Congmeng Li, Shunde Li, Xin Jiang, Maotao Yu, Haoming Yan, Haoxin Chen, Bin Liu, Qiuyang Li, Suhas Mahesh, Lei Li, Hui Li, Dengke Wang, Xiaojun Li, Zheng-Hong Lu, Moritz Riede, Rui Zhu, Henry J. Snaith. *Ytterbium Oxide-based Interconnecting Layer for Monolithic Peorvksite-organic Tandem Solar Cells with Small Voltage Loss.*

[#]These authors contribute equally.

6.1 Abstract

Monolithic perovskite-organic tandem solar cells (POTSCs) have attracted increasingly attentions in recent years due to their compatible fabrication routes and advances in single cell efficiencies. To further boost the performance of POTSCs, it is necessary to reduce the voltage losses which mainly arise from WBG cells and ICLs. Here a surface treatment strategy was proposed to passivate the WBG perovskite interface and obtained a PCE over 20% with a Voc over 1.3 V. Next an ICL based on Yb_2O_3 was designed for constructing the monolithic POTSC. The Yb_2O_3-based ICL forms Ohmic contact and possesses high transparency in interested range. Based on the designed ICL, the champion POTSC obtained a PCE of 22.6% and a notable Voc of 2.11 V with a small voltage loss of 0.02 V. Also it is fully thermal-evaporable which is promising for scalable fabrication, providing insights for future ICL design for POTSCs.

6.2 Introduction

In recent years, PSCs have made impressive progress in the PCE, which is comparable to the record of single-junction silicon solar cells and approaching the theoretical SQ limit of 33.7%.[52,324] To further harness the incident light and increase the PCE surpassing the SQ limit, great efforts are dedicated to fabricate TSCs which comprises multiple light absorbers, typically one WBG absorber and one NBG absorber that are responsible for absorbing short-wavelength and long-wavelength photons, respectively. PSCs and OSCs share similar layered device structure and solution-processable fabrication route, making it technically encouraging to fabricate monolithic POTSCs. Furthermore, the solvents used for dissolving perovskite precursors e.g. DMF, DMSO are orthogonal with those used for organic films e.g. chlorobenzene (CB). This feature makes the processing steps less demanding when depositing rear absorbers and

provides more flexibility in ICLs design and fabrication. Historically, the research in POTSCs was dated back to 2015 which obtained a modest PCE of 10.2%.[246] The main loss was attributed to overlapped absorption ranges of two subcells i.e. MBG perovskite and PCBM. Due to the domination of PCBM in early-stage OSCs, the development of POTSCs has been long limited by the unmatched absorption range and less efficient NIR absorption. Recently, the breakthrough in NFA inspired the advance of OSCs since these NFA-based OSCs own NBG of 1.2~1.4 eV with strong absorption in NIR and small voltage loss, Therefore, the lifts in both Jsc and Voc have taken the PCE a major step forward approaching 20%.[2,3] The achievement in OSCs sees the promise in further promoting monolithic POTSCs.

As the monolithic TSCs are connected in series, it is necessary to reduce voltage loss in each component to maximize the total Voc. The large Voc deficit of WBG perovskite is regarded as one challenging factor hindering achieving efficient TSCs, which is mainly attributed to trap-assisted non-radiative recombination in perovskite films and poor heterojunction at the perovskite/charge transporting layers.[263] The Voc deficit in a MBG perovskite can be reduced down to as low as 0.3 eV.[325] In contrast, it is still difficult to obtain a Voc above 1.30 eV in a 1.80 eV WBG perovskites, indicating a Voc deficit greater than 0.5 eV that limiting the overall device performance.

In addition to light absorbers, the ICL also plays a nonnegligible role. As introduced in **Section 2.3.3**, the ICL design should meet the criteria in all three aspects: Ohmic contact, minimal parasitic absorption, and mechanically robust. Typically, the ICLs in perovskite-based TSCs are configured in sandwich stacks: the ETL / charge recombination layer (CRL) / HTL. However the state-of-the-art ICL usually adopt SnO_x

as the ETL which is processed by the time-consuming atomic-layer-deposition (ALD) technique.[124,126] Therefore, the advance in ICL design catering for both performance and technical considerations is necessary.

This work starts with the fabrication of WBG PSCs. As WBG PSCs act as the front cells, their surface roughness will directly affect the quality of the subsequent films e.g. ICLs and NBG subcells. Therefore, for integrating into TSCs in this Chapter, the WBG PSCs with hill-type geometric morphology (**Chapter 4**) have been replaced by the one prepared in **Chapter 5**. In this work, Voc deficit was firstly suppressed through a surface treatment strategy for WBG perovskite leading to the improved surface, boosting the Voc over 1.3 eV with a reduced Voc deficit of 0.46 eV. The champion WBG perovskite cell delivered a PCE over 20% with a Jsc of 18.5 mA cm^{-2} and a FF of 0.83. Taking the WBG perovskite as the front subcell, a facile ICL design was further demonstrated using a 1.5 nm layer of Yb_2O_3 for POTSCs. Yb can be easily thermal-evaporated and oxidized into a metal oxide film, working as the buffer layer. The low work function of Yb_2O_3 enables it to form an Ohmic contact at the ETL/CRL interface, thereby facilitating the electron transport. Then the full POTSC was fabricated in the p-i-n structure as follow: ITO/NiO_x/self-assembled molecules (SAM)/perovskite/**C60/ Yb_2O_3/Au/MoOx**/organic/PFNBr/Ag. A WBG (1.77 eV) perovskite $FA_{0.83}Cs_{0.17}Pb(I_{0.6}Br_{0.4})_3$ and a NBG (1.33 eV) organic blend of PM6:Y6 were used as the front and rear absorbers, respectively. Due to the well matched subcells and effective ICL, the champion POTSC delivered a PCE of 22.6% with an impressive Voc of 2.11 V, a Jsc of 13.6 mA cm^{-2}, a FF of 0.79. The small tandem voltage loss demonstrate that two subcells were efficiently connected where voltage drop in ICL is negligible. Also, as the ICL is fully thermal-evaporated, the processing route can be greatly simplified,

making it strongly competitive in scalable production.

6.3 Surface treatment for WBG perovskite cells

This work started with preparing WBG perovskite absorbers using the composition $FA_{0.83}Cs_{0.17}Pb(I_{0.6}Br_{0.4})_3$ reported in previous work.[121] To passivate the perovskite surface, a mixture of phenethylammonium iodide (PEAI) and methylamium iodide (MAI) was spin-coated atop the annealed perovskite films. The morphology and structural information were firstly checked. The SEM images (**Fig. 6.1a-b**) have clearly shown that the brighter (electron-dense) crystallites have been removed after the treatment. From the XRD results (**Fig. 6.1c**), it is found that the peak at 12.7° corresponding to PbI_2 is no longer visible, indicating most of the excess unreacted PbI_2 has been "digested". Beyond the surface, there is no distinct change in the XRD patterns, implying no structural variation occurs in the perovskite bulk. The UV-vis absorption spectra also confirmed that there is no distinct change in bandgap after the treatment (**Fig. 6.1d**). These results suggests that the surface treatment can effectively polish the perovskite surface while make little change over bulk structure.

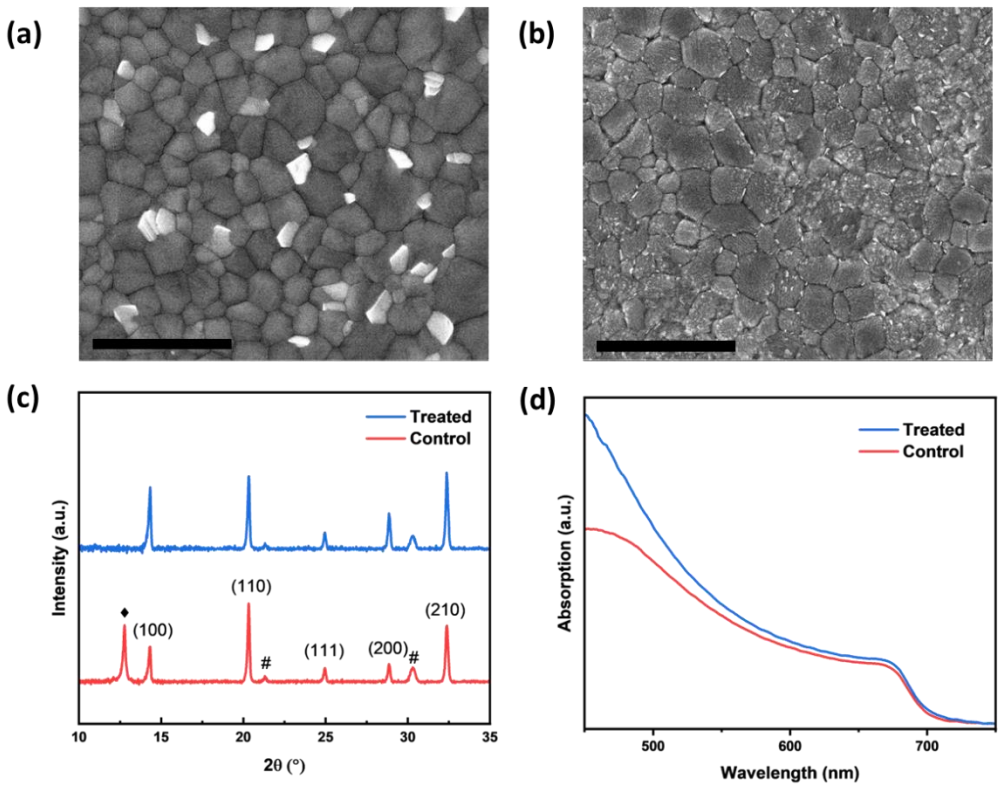


Fig. 6.1 Surface treatment for WBG perovskite.
(a,b) SEM images of perovskite films **(a)** without and **(b)** with surface treatment, scale bar = 1 μm. **(c)** XRD spectra of perovskite films. Indices are for the perovskite phase, and secondary phases are marked: PbI2 with ♦, ITO with #. **(d)** Absorption spectra of perovskite films deposited on quartz substrates.

To assess the effect of the surface treatment on the interfacial passivation, the TRPL decay and EL measurement were performed (**Fig. 6.2**). The TRPL decay demonstrate that treated films exhibit much longer carrier lifetime than the control ones (**Table 6.1**), demonstrating the effective suppression achieved by the surface treatment. From the EL measurement, it is clearly that much higher EL intensities and external radiative efficiency (ERE) were recorded for treated samples than control ones. By passivating the surfaces, the treatment strongly reduces the interfacial loss which thereby contribute to the Voc.

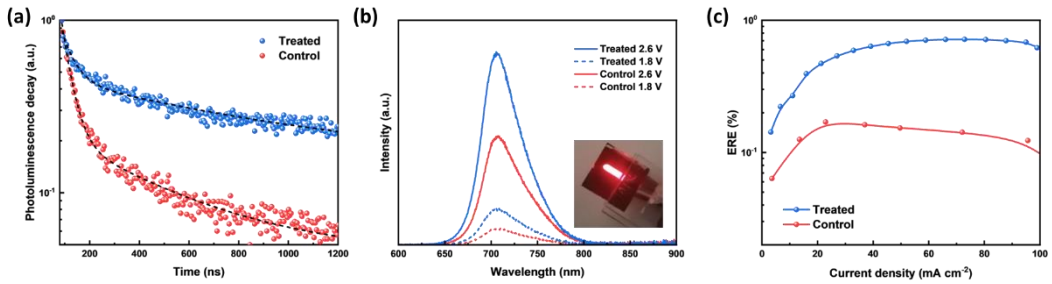


Fig. 6.2 Optoelectronic properties of WBG perovskites.
(a) TRPL decays for perovskite films on ITO substrates. **(b)** EL spectra of perovskite cells under the different bias operating as LED. Inset: the photograph of the treated perovskite cell with a bias ~3 V. The EL were performed by Peng Chen, Peking University. **(c)** ERE versus current density for perovskite cells.

Table 6.1 Lifetime from fitting curves of the TRPL decay measurements according to methods introduced in Section 3.3.

	Sample	A1	τ1 (ns)	A2	τ2 (ns)	τ_{ave} (ns)
Control	ITO/SAM/perovskite	8.05	37.0	0.20	428.7	124.5
Treated	ITO/SAM/perovskite + treatment	2.50	49.4	0.33	848.8	604.2

The effective surface passivation leads to the enhancement in overall device performance (**Table 6.2** and **Fig. 6.3**). From the J-V scan under AM1.5G (100 mW cm^{-2}), it shows that the champion treated cell obtained a PCE over 20%, a Voc over 1.3 V with a small voltage loss of 0.46 V, which are all among the most efficient WBG cells with the similar bandgap (**Table 6.3**). The EQE spectra are consistent with the trend in the J-V scans. These results proved the effectiveness of this treatment strategy in mitigating surface loss of WBG perovskites.

Table 6.2 Device performance of WBG PSCs without and with surface treatment

		Voc (V)	**Jsc (mA cm^{-2})**	**FF**	**PCE (%)**
Control	Best	1.25	17.9	0.78	17.3
	(Average)	(1.23±0.01)	(17.6±0.48)	(0.73±0.04)	(15.9±1.10)
Treated	Best	1.30	18.5	0.83	20.1
	(Average)	(1.29±0.01)	(18.3±0.55)	(0.79±0.02)	(18.6±0.96)

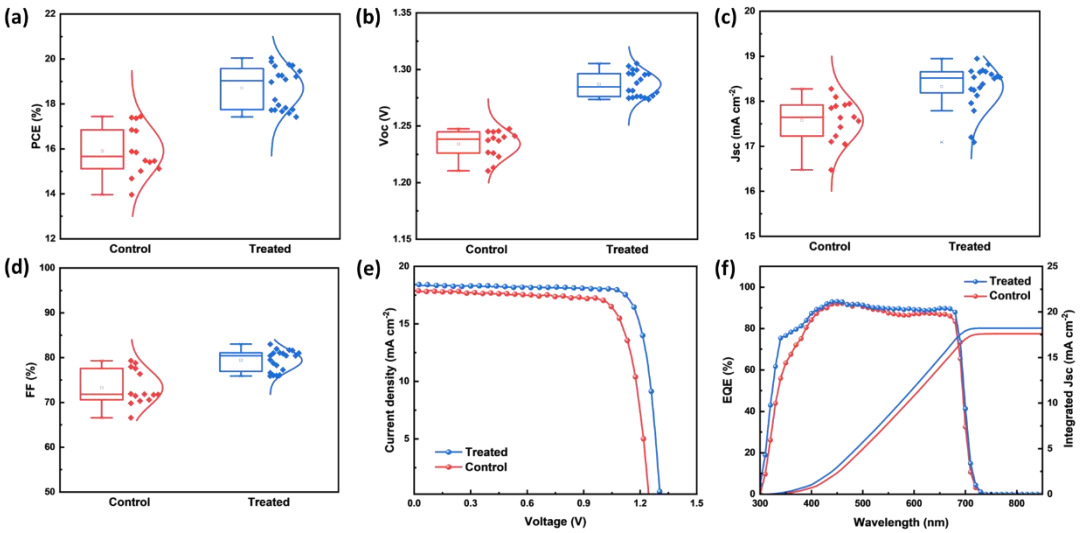


Fig. 6.3 Device performance comparison between control and treated WBG PSCs.
(a-d) Device performance parameters statistics of WBG PSCs. **(e)** J-V scans for WBG PSCs under AM1.5G 100 mW/cm^2. **(f)** EQE spectra for WBG PSCs. The EQE were performed by Bin Liu, Southern University of Science and Technology.

Table 6.3 Summary of representative state-of-the-art p-i-n WBG (1.75~1.80 eV) PSCs in the literature.

V_{OC} (V)	J_{SC} (mA cm^{-2})	FF	PCE (%)	Voc loss (V)	Year	Ref.
1.22	17.0	0.80	16.5	0.55	2019	124
1.24	17.9	0.82	18.2	0.51	2019	125
1.21	17.1	0.77	15.9	0.56	2020	232
1.23	16.5	0.79	16.0	0.55	2020	126
1.26	17.9	0.79	17.8	0.53	2022	127
1.34	15.6	0.81	16.8	0.51	2022	237
1.26	18.6	0.79	18.6	0.49	2022	128
1.26	17.4	0.80	17.7	0.54	2022	129
1.22	17.4	0.82	17.3	0.54	2022	130
1.32	18.7	0.82	20.3	0.43	2022	114
1.33	18.1	0.84	20.2	0.46	2022	113
1.30	18.5	0.83	20.1	0.47	2023	**This work**

6.4 Design of NBG organic cells and ICLs

Based on the enhanced WBG perovskite cells, next step moved onto the design of NBG cells and ICLs for the fabrication of full POTSCs (**Fig. 6.4a**). The choice of NBG absorber should take two factors into account: strong light absorption in NIR range and small voltage loss. To pair with the 1.77 eV perovskite, a NBG organic blend of PM6:Y6 with a bandgap of 1.33 eV is chosen.[326] The organic absorber is consisted of a polymer PM6 as the donor and a non-fullerene small molecular Y6 as the acceptor, which has been widely proved to be efficient and reliable. It has two absorption peaks in 550-850 nm corresponding to PM6 and Y6 respectively,[160] ensuring the complementary absorption of low energy incident photons (**Fig. 6.4b**).

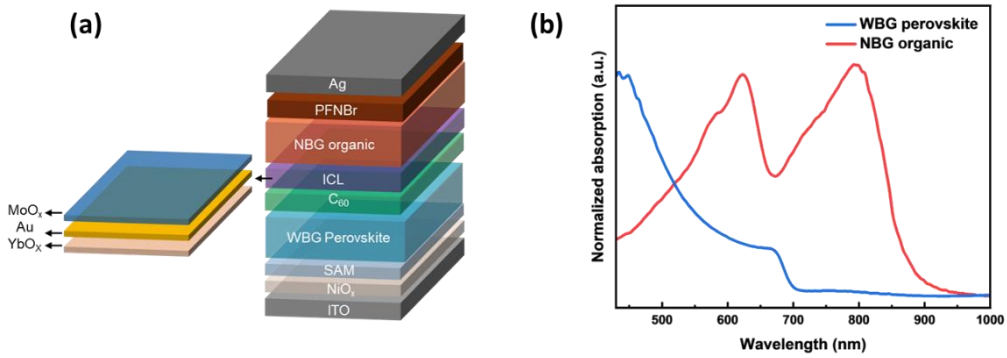


Fig. 6.4 (a) Schematics of a POTSC. **(b)** Absorption spectra of perovskite and organic films.

The organic cells were fabricated with a device structure of ITO/MoOx/PM6:Y6/PFNBr/Ag and achieved a high Voc of 0.85 V. Statistics of device parameters are presented in **Fig. 6.5** along with WBG perovskite cells for comparison.

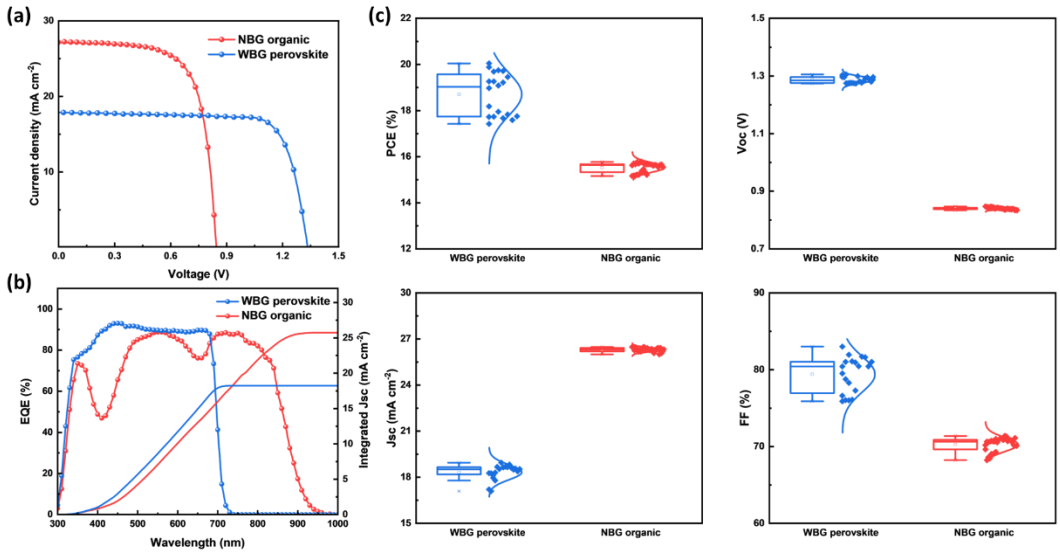


Fig. 6.5 Device performance of perovskite and organic subcells.
(a) JV curves under AM1.5G 100 mW/cm^2. **(b)** EQE spectra. **(c)** Device performance parameters statistics. The EQE of NBG organics were measured by Xin Jiang, Institute of Chemistry, Chinese Academy of Science.

As guided by **Section 2.3**, to connect the two subcells into one monolithic device, the design of ICLs should stress on both the functionality (i.e. electrical and optical considerations) and practicality (i.e. challenges encountered during the processing). The electrical consideration requires materials with suitable energy levels and high conductivity so that electrons and holes can be effectively extracted here and annihilated quickly. The optical consideration refers to the "relative transparency" i.e. materials should be highly transparent in interested range in order to enable sufficient photons to pass. Last but even more important is that the processing of the latter layers shall not damage the former layers e.g. high-energy bombardment and solvent dissolving. Furthermore, stable and cost-effective materials and facile processing methods are preferred. Based on these factors, several commonly used ICLs with different CRLs were compared (**Fig. 6.6a**). The one solely employ sputtered AZO as the CRL demonstrates severe S-shaped J-V curve due to the misaligned energy levels and thereby non-Ohmic contact within the ICL stack. Replacing the AZO with Au can

mitigate the S-kink, while the low Voc and FF are attributed to the insufficient charge extraction and recombination. The joint deposited Au and sputtered AZO together work as a promising CRL, however the complicated processing steps adds extra practical difficulties and burden. Here the ICL was designed based on a 1.5 nm Yb_2O_3. This ICL can be fully thermal-evaporated which is time-saving and cost-effective, providing much convenience in real processing. In **Section 5.3**, it is confirmed that metallic Yb can be easily oxidized into Yb_2O_3 during the evaporation process, implying no extra oxidization step is needed. The J-V scans on the ICL diode samples confirmed that the deposition of Yb_2O_3 enables the Ohmic connection (**Fig. 6.6b**). Moreover, the ICL is highly transparent over the NIR range, guaranteeing the adequate photons reaching the NBG organic cells (**Fig. 6.6c**).

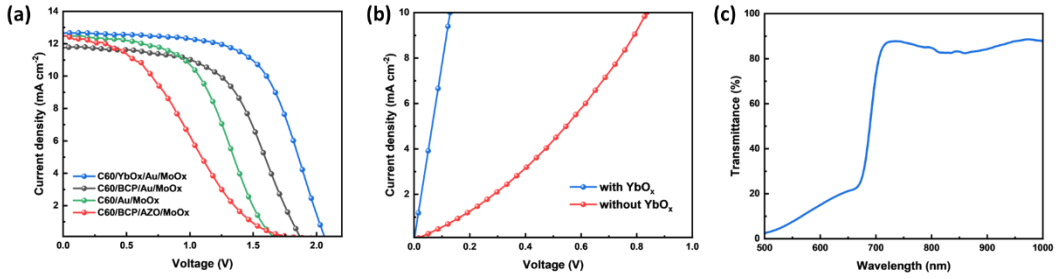


Fig. 6.6 Properties of Yb_2O_3-based ICL.
(a) J-V curves of several POTSC with different ICLs. **(b)** J–V characteristics of the diode devices with the structure of ITO/C60/(Yb_2O_3)/Au/MoOx/Ag. **(c)** Transmittance spectra of a half tandem stack: ITO/NiOx/SAM/PVSK/C60/ Yb_2O_3/Au/MoOx.

Next the possible working mechanism of this ICL is discussed. It is noted that the evaporated 1 nm Au tends to form islands rather than continuous film, which is insufficient to cover the whole Yb_2O_3 layer. Therefore, it is speculated that it is the joint Yb_2O_3/Au layer working together as the CRL between C60 and MoOx. From the UPS spectra, Yb_2O_3 has a low work function of 3.48 eV, which contributes to the total work function of Yb_2O_3/Au to 4.58 eV (pure Au has a work function of 5.1 eV) (**Fig. 6.7a**).

The possible mechanism of the ICL is depicted in **Fig. 6.7b**.

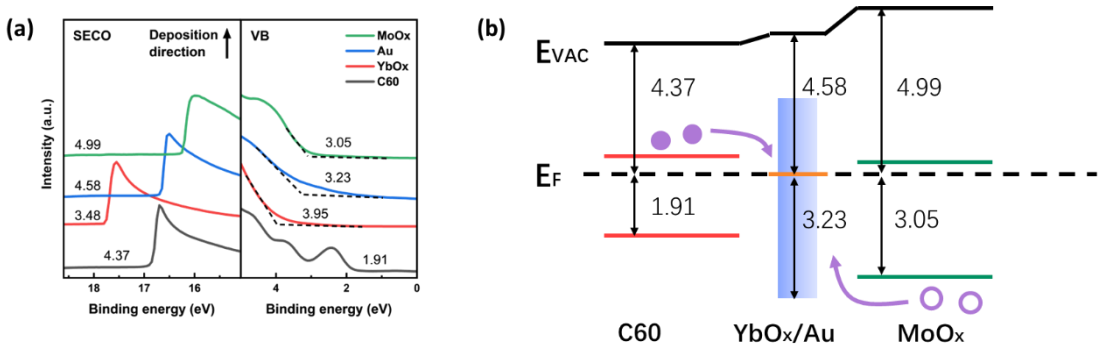


Fig. 6.7 ICL working mechanism.
(a) UPS spectra of ICL component along the deposition direction. Left panel: secondary electrons cut-off (SECO). Right panel: valance band (VB) edge. The bandgaps of C60 and MoOx refer to the literature Ref.[349] and Ref.[350], respectively. The bandgap of Yb_2O_3 is measured using the reflection electron energy loss spectroscopy (REELS) as shown in **Fig.4.5. (b)** Schematics of ICL working mechanism. E_F=Fermi energy. E_{VAC}=vacuum level.The UPS was measured by Nan Chen, Yunnan University.

6.5 Device performance of POTSC

With the Yb_2O_3-based ICL, the device configuration is confirmed as follow: ITO/NiOx/SAM/WBG perovskite/C60/ Yb_2O_3/Au/MoOx/NBG organic/PFNBr/Ag. To maximize the overall performance of POTSC, it is necessary to consider the well-balanced light absorption in both WBG and NBG subcells. Here the TMM modeling was used to simulate the photon distribution and absorption within the device and thereby provide information guiding the device fabrication.[327] The key information used in the simulation is summarized in **Table 6.4**.

Table 6.4 Key parameters and sources used in optical simulation.

Materials	Thickness (nm)	Ref.
ITO	100	[328]
NiOx	30	[329]
WBG perovskite	50-400	This work
C60	40	[330]
Yb_2O_3	1.5	This work
Au	1	[331]

MoOx	10	332
NBG organic	50-200	333
PFN-Br	5	334
Ag	100	335

As the two subcells are connected in series in which the Jsc of POTSC depends on the current-limiting subcell, it is thereby necessary to balance the photocurrent in both sides. **Fig. 6.8a** presents the relation between two absorber thicknesses and Jsc of POTSC. It is found the optimal thickness for perovskite and organic absorbers is 150-250 nm and 150-180 nm, when the maximized Jsc is ~14 mA cm^{-2}. To analyse the photon absorption distribution within the device, **Fig. 6.8b** was calculated based on a 260 nm perovskite and 180 nm organic absorber. It is noticed that most of visible photons are absorbed by the WBG perovskite while NIR photons are absorbed by the NBG organic layer. There is a small fraction of visible photons at 550-700 nm overlapped in both perovskite and organic absorption range, which is consistent with the EQE results (**Fig. 6.9b**) and accounts for the Jsc loss. Guided by the optical simulation results the POTSC with optimized absorber thicknesses was fabricated, as shown in **Fig. 6.8c**.

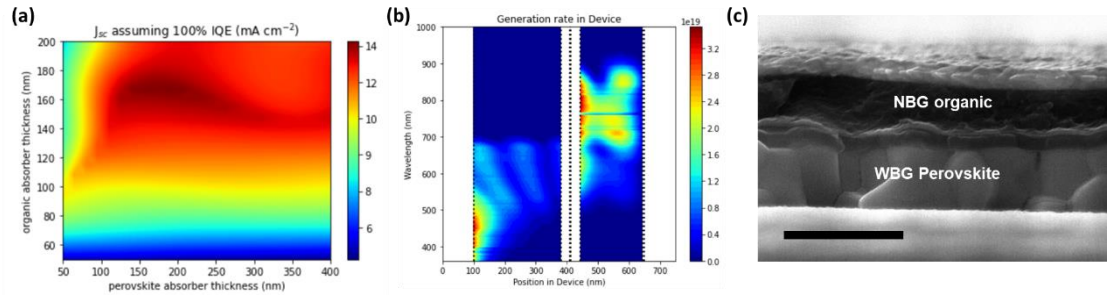


Fig. 6.8 Optical simulation for device optimization.
(a) Simulated Jsc as a function of the variable thicknesses of perovskite and organic absorbers. **(b)** Photon absorption rate distribution within a POTSC. Light comes through from left to right, along with the device fabrication steps. **(c)** Cross sectional SEM image for a POTSC, scale bar = 500 nm.

The device performance of champion POTSC is demonstrated in **Fig. 6.9a** and

Table 6.5. The champion cell obtained a PCE of 22.6%, a Jsc of 13.6 mA cm^{-2}, a FF of

0.79 and a notable Voc of 2.11 V with a small voltage loss of 0.02 V which demonstrates the effectiveness of Yb_2O_3-based ICL (**Fig. 6.9c**). The PCE was tracked at the MPP with a voltage of 1.76 V and obtained a SPO of 21.5% (**Fig. 6.9d**). From the **Fig. 6.9e,f**, the POTSC possesses good storage and thermal stability (65°C) in nitrogen atmosphere without encapsulation. A good POTSC should achieve high PCE and Voc, while the Voc loss is also an important figure of merit to demonstrate the quality of ICL. Compared this work with representative p-i-n POTSCs reported in the literature in terms of these three key parameters. In **Fig. 6.10**, the top right corner refers to the ideal region, where it is clearly that the device achieved a well-balanced performance. The device performance statistics are presented in **Fig. 6.11**, indicating a good reproducibility among batches.

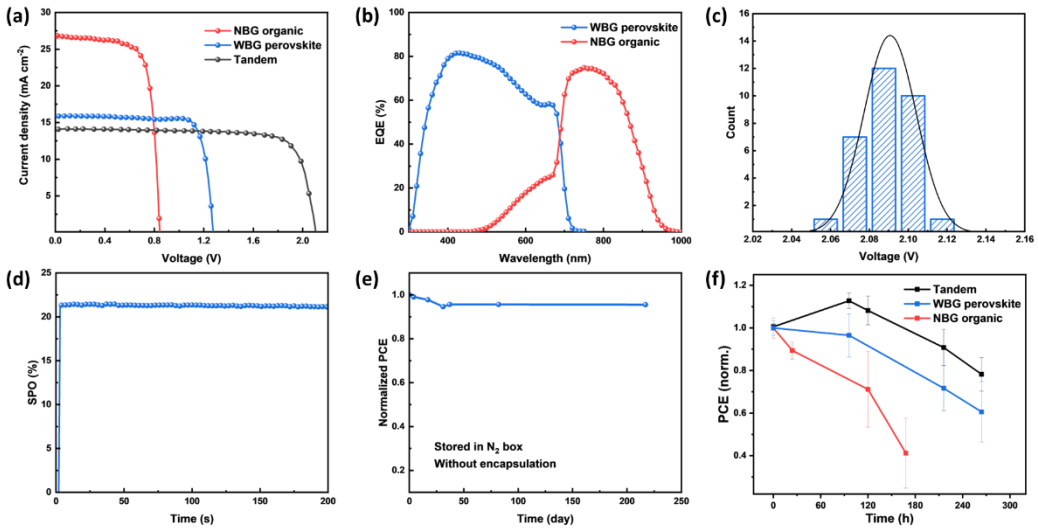


Fig. 6.9 Device performance of POTSC.
(a) J-V curves of perovskite, organic subcells and tandem cell under AM1.5G 100mW/cm^2. **(b)** EQE of perovskite and organic subcells. **(c)** Voc distribution of POTSC over different batches. **(d)** Steady-state power output of POTSC at maximum power point under one-sun illumination AM1.5G spectrum. **(e)** Storage stability for POTSC without encapsulation stored in a N_2 box. **(f)** Thermal stability for perovskite, organic subcells and tandem cells. The unencapsulated cells were placed on a 65°C hot plate in the N_2 glovebox. The EQE were measured by Peng Chen, Peking University.

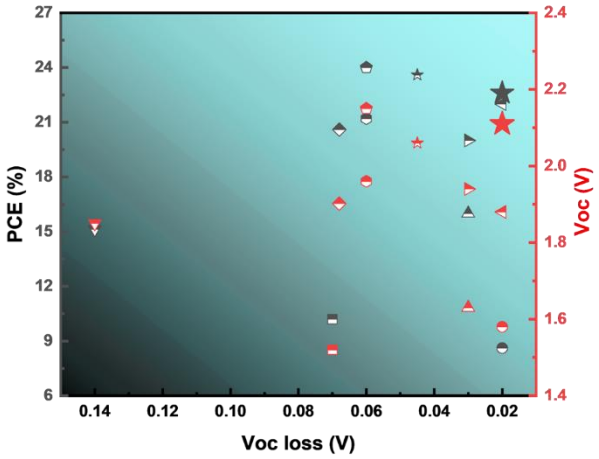


Fig. 6.10 Literature comparison of POTSCs.
Three key parameters are featured: PCE (black), Voc (red) and Voc loss (x-axis). Each publication contains two symbols with the same pattern whereas different colors. Data from total 11 publications including this work are shown here for comparison and summarized in **Table 6.6**.

Table 6.5 Device performance of champion POTSC and subcells.

		Voc (V)	Jsc (mA cm^{-2})	FF	PCE (%)
WBG perovskite		1.28	15.3	0.83	16.1
NBG organic	Best	0.85	26.3	0.71	15.7
	(Average)	(0.84±0.00)	(26.3±0.14)	(0.71±0.01)	(15.60±0.15)
POTSC	Best	2.11	13.6	0.79	22.6
	(Average)	(2.09±0.01)	(13.5±0.17)	(0.78±0.01)	(21.9±0.30)

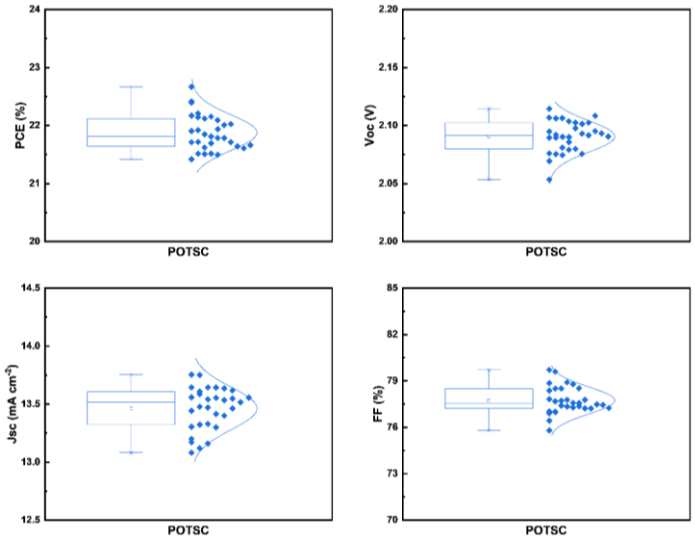


Fig. 6.11 Statistics of device performance parameters for 31 POTSC devices.

Table 6.6 Summary of the key device performances of representative p-i-n POTSCs reported.

ICL	V_{OC} (V)	J_{SC} (mA cm^{-2})	FF	PCE (%)	Voc loss (V)	Year	Ref.
PFN/TiO_2/PEDOTPSS PH500/PEDOTPSS 4082	1.52	10.05	0.67	10.2	0.07	2015	[336]
PCBM/PFN/Ag/MoO_x	1.58	8.02	0.68	8.62	0.02	2016	[337]
PCBM/C60-SB/Ag/MoO_x	1.63	13.1	0.75	16.0	0.03	2016	[243]
PCBM/BCP/Au/MoO_x	1.85	15.1	0.71	11.5	0.14	2020	[338]
C60/BCP/Ag/MoO_x	1.88	15.7	0.75	22.0	0.02	2022	[240]
PCBM/BCP/Au/MoO_x	1.94	20.0	0.79	13.1	0.03	2022	[339]
C60/BCP/Ag/MoO_x	1.90	13.1	0.83	20.6	0.068	2020	[242]
PCBM/BCP/Ag/MoO_x	1.96	13.8	0.78	21.2	0.06	2022	[241]
C60/BCP/IZO/MoO_x	2.06	14.8	0.77	23.6	0.045	2022	[127]
PCBM/AZO-NP/SnO_x/InO_x/MoO_x	2.15	14.1	0.78	24.0	0.06	2022	[237]
C60/Yb_2O_3/Au/MoO_x	2.11	13.6	0.79	22.6	0.02	2023	**This work**

6.6 Conclusion

In summary, the effectiveness of surface treatment over WBG perovskite films in interfacial passivation was demonstrated and achieved a PCE of 20.1% with a Voc of 1.3 V. Then an ICL design was developed based on thermally deposited Yb_2O_3. The insertion of Yb_2O_3 modifies the overall work function of CRL and forms the Ohmic contact, facilitating charge extraction and recombination as evidenced by the high Voc and FF. The Yb_2O_3-based ICL also has high transmittance over the NIR range and uniform film morphology, which is benefit for the NBG organic layer in both optical and mechanical aspects. Optical simulation results are analyzed to balance the light absorption in both subcells. The POTSC with optimized absorber thicknesses is fabricated and achieved a PCE of 22.6% and a notable Voc of 2.11 V. The small voltage loss of 0.02 V achieved is among the smallest voltage loss in reported POTSCs and is attributed to the effectiveness of Yb_2O_3-based ICL. Also the ICL can be fully thermally evaporated in a row which is manufacturing friendly and provides strong competitiveness in scalable production.

7. Summary and outlook

Given that PSCs and OSCs made great progress respectively in the past decade, the design of POTSCs combining both merits provides new way for fabricating efficient TSCs. However the efficiency of POTSC still lags behind other types of perovskite-based TSCs. The works presented in this thesis aim to address the key factors impeding from achieving efficient POTSCs.

A good WBG PSC is the foundation for a good perovskite-based TSC. In **Chapter 4** a strategy is introduced to manipulate the geometric morphology of WBG perovskite films. It is found that the fill factor is strongly affected by the perovskite film morphology which strongly impacts on the interfacial carrier extraction. The manipulation of the film morphology also improves the film quality, giving rise to the distinct enhancement in FF from 0.65 to 0.80 on average. The champion cell obtains a FF of 0.83 and a PCE over 18%. The in-situ characterization indicates that the optimal morphology is related to the delayed crystallization process. The work in this Chapter suggests that geometric manipulation could be new method for improving WBG PSCs.

In **Chapter 5**, a 1.5 nm thin Yb_2O_3 was employed as the buffer layer between the ETL and the metal electrode for p-i-n PSCs. The Yb_2O_3 has no marked interaction with perovskite and adjacent layers, demonstrating good chemical stability. It can also act as the barrier preventing the interdiffusion of metal ions, thereby alleviating the risk of electrode-induced degradation. Three types of PSCs with NBG, MBG and WBG perovskites are fabricated respectively, and the high PCEs achieved in all three bandgaps indicate that Yb_2O_3 does little damage to the device performance. In addition, Yb_2O_3 is cost-effective materials and thermally evaporable, suggesting the great

potentials in the commercialization of PSCs. These results demonstrate that Yb_2O_3 is a qualified buffer material for efficient and stable PSCs.

The fabrication of POTSCs is illustrated in **Chapter 6**. Learning from the lessons in **Chapter 4 & 5**, an efficient WBG PSC with a PCE of 20.1% and a Voc of 1.3 V is firstly prepared. Then an ICL is designed based on the thin Yb_2O_3 introduced in **Chapter 5**. Characterizations prove that the Yb_2O_3-based ICL is capable of forming Ohmic contact and allowing sufficient light passing through. NBG organic materials are selected to pair with WBG perovskite. The optical simulation is performed to analyse the light absorption and guide the fabrication of full devices. Finally the optimized POTSC achieves a PCE of 22.6% with a notable Voc of 2.11 eV which is among the smallest voltage loss in the reported POTSCs.

Generally, this thesis has presented a systematic work on how to fabricate efficient POTSCs. Indeed there is still plenty of room to explore in the future. Here several key points are discussed as the hints for future research.

Firstly, the Jsc in POTSCs (<15 mA cm^{-2}) is still far from that of perovskite-Si TSCs (>19 mA cm^{-2}) and all-perovskite TSCs (>16 mA cm^{-2}), which contributes most to the efficiency gap among the perovskite-based TSCs. The deficit of Jsc is mainly due to the nonideal paired bandgaps of perovskite and organic materials. More specifically, the OSCs with ultranarrow bandgap < 1.2 eV is still much inferior to silicon solar cells and NBG PSCs, resulting in the overall deficit of POTSCs. Therefore, the design of new organic materials with ultranarrow bandgap helps extend the light absorption range towards 1100nm.

Secondly, WBG PSCs have not yet reach their limit. Although massive efforts aim to increase the Voc, the Voc loss in WBG PSC is still larger than that in their counterparts with lower bandgaps. As the widened bandgap usually requires composition engineering, the multiple mixed ions interweave and make it more difficult to investigate and passivate the defects. The advance in understanding the loss mechanism would not only minimize the voltage loss but also address the long concerns on stability of WBG PSCs.

Thirdly, a facile and effective ICL is to be designed. Considering the requirements of commercialization, an ICL should contains as few layers as possible, and the processing should be timesaving and energy-saving. Currently most of good ICLs need either multiple layer or sophisticated processing or both, making the realistic fabrication of ICLs in a dilemma. Hence, new ICLs is expected to be one layer with proper band structures aligning with adjacent materials, high transmittance in NIR range, highly conductive and robust. Addressing the three points above enables POTSCs to release their full potentials.

Finally, the stability of POTSCs should be stressed. This requires further understanding and improvement for both WBG perovskite and NBG organic absorbers. Moreover, the stability should be treated as a whole so that the choice of other functiona layers should also be taken into consideration with equal importance. On this basis, POTSCs could take their competitiveness one step further.

8. Reference

1. NREL. NREL cell efficiency. https://www.nrel.gov/pv/interactive-cell-efficiency.html.
2. Xu, X. *et al.* Sequential Deposition of Multicomponent Bulk Heterojunctions Increases Efficiency of Organic Solar Cells. *Advanced Materials* 2208997 (2023) doi:10.1002/adma.202208997.
3. Bi, P. *et al.* Enhancing Photon Utilization Efficiency for High-Performance Organic Photovoltaic Cells via Regulating Phase-Transition Kinetics. *Advanced Materials* 2210865 (2023) doi:10.1002/adma.202210865.
4. Park, J. *et al.* Controlled growth of perovskite layers with volatile alkylammonium chlorides. *Nature* (2023) doi:10.1038/s41586-023-05825-y.
5. Shockley, W. & Queisser, H. J. Detailed balance limit of efficiency of p-n junction solar cells. *J Appl Phys* **32**, 510–519 (1961).
6. Chakhmouradian, A. R. & Woodward, P. M. Celebrating 175 years of perovskite research: a tribute to Roger H. Mitchell. *Phys Chem Miner* **41**, 387–391 (2014).
7. Yin, W.-J., Shi, T. & Yan, Y. Superior Photovoltaic Properties of Lead Halide Perovskites: Insights from First-Principles Theory. *The Journal of Physical Chemistry C* **119**, 5253–5264 (2015).
8. De Wolf, S. *et al.* Organometallic Halide Perovskites: Sharp Optical Absorption Edge and Its Relation to Photovoltaic Performance. *J Phys Chem Lett* **5**, 1035–1039 (2014).
9. Ugur, E. *et al.* Life on the Urbach Edge. *J Phys Chem Lett* **13**, 7702–7711 (2022).
10. Urbach, F. The Long-Wavelength Edge of Photographic Sensitivity and of the Electronic Absorption of Solids. *Physical Review* **92**, 1324–1324 (1953).
11. Huang, J., Yuan, Y., Shao, Y. & Yan, Y. Understanding the physical properties of

hybrid perovskites for photovoltaic applications. *Nat Rev Mater* **2**, 17042 (2017).

12. Jean, J. *et al.* Radiative Efficiency Limit with Band Tailing Exceeds 30% for Quantum Dot Solar Cells. *ACS Energy Lett* **2**, 2616–2624 (2017).
13. Dong, Q. *et al.* Electron-hole diffusion lengths > 175 μm in solution-grown $CH_3NH_3PbI_3$ single crystals. *Science (1979)* **347**, 967–970 (2015).
14. Yang, X. *et al.* Superior Carrier Lifetimes Exceeding 6 μs in Polycrystalline Halide Perovskites. *Advanced Materials* **32**, 2002585 (2020).
15. Miyata, K., Atallah, T. L. & Zhu, X.-Y. Lead halide perovskites: Crystal-liquid duality, phonon glass electron crystals, and large polaron formation. *Sci Adv* **3**, (2017).
16. Batignani, G. *et al.* Probing femtosecond lattice displacement upon photo-carrier generation in lead halide perovskite. *Nat Commun* **9**, 1971 (2018).
17. Stranks, S. D. *et al.* Recombination Kinetics in Organic-Inorganic Perovskites: Excitons, Free Charge, and Subgap States. *Phys Rev Appl* **2**, 034007 (2014).
18. Shi, D. *et al.* Low trap-state density and long carrier diffusion in organolead trihalide perovskite single crystals. *Science (1979)* **347**, 519–522 (2015).
19. Stranks, S. D. & Snaith, H. J. Metal-halide perovskites for photovoltaic and light-emitting devices. *Nat Nanotechnol* **10**, 391–402 (2015).
20. Guo, J. *et al.* Ultralong Carrier Lifetime Exceeding 20 μs in Lead Halide Perovskite Film Enable Efficient Solar Cells. *Advanced Materials* **35**, (2023).
21. Ablekim, T. *et al.* Exceeding 200 ns Lifetimes in Polycrystalline CdTe Solar Cells. *Solar RRL* **5**, (2021).
22. Krause, M. *et al.* Microscopic origins of performance losses in highly efficient Cu(In,Ga)Se2 thin-film solar cells. *Nat Commun* **11**, 4189 (2020).
23. Guzelturk, B. *et al.* Terahertz Emission from Hybrid Perovskites Driven by

Ultrafast Charge Separation and Strong Electron–Phonon Coupling. *Advanced Materials* **30**, 1704737 (2018).

24. Zhu, H. *et al.* Screening in crystalline liquids protects energetic carriers in hybrid perovskites. *Science (1979)* **353**, 1409–1413 (2016).
25. Miyata, K. *et al.* Large polarons in lead halide perovskites. *Sci Adv* **3**, (2017).
26. Neukirch, A. J. *et al.* Polaron Stabilization by Cooperative Lattice Distortion and Cation Rotations in Hybrid Perovskite Materials. *Nano Lett* **16**, 3809–3816 (2016).
27. Bischak, C. G. *et al.* Origin of Reversible Photoinduced Phase Separation in Hybrid Perovskites. *Nano Lett* **17**, 1028–1033 (2017).
28. Wu, X. *et al.* Light-induced picosecond rotational disordering of the inorganic sublattice in hybrid perovskites. *Sci Adv* **3**, (2017).
29. Jiang, C.-S. *et al.* Carrier separation and transport in perovskite solar cells studied by nanometre-scale profiling of electrical potential. *Nat Commun* **6**, 8397 (2015).
30. Tan, L. Z. *et al.* Shift current bulk photovoltaic effect in polar materials—hybrid and oxide perovskites and beyond. *NPJ Comput Mater* **2**, 16026 (2016).
31. Frost, J. M. *et al.* Atomistic Origins of High-Performance in Hybrid Halide Perovskite Solar Cells. *Nano Lett* **14**, 2584–2590 (2014).
32. Jena, A. K., Kulkarni, A. & Miyasaka, T. Halide Perovskite Photovoltaics: Background, Status, and Future Prospects. *Chem Rev* **119**, 3036–3103 (2019).
33. Kojima, A., Teshima, K., Shirai, Y. & Miyasaka, T. Organometal Halide Perovskites as Visible-Light Sensitizers for Photovoltaic Cells. *J Am Chem Soc* **131**, 6050–6051 (2009).
34. Burschka, J. *et al.* Tris(2-(1 *H* -pyrazol-1-yl)pyridine)cobalt(III) as p-Type Dopant for Organic Semiconductors and Its Application in Highly Efficient

Solid-State Dye-Sensitized Solar Cells. *J Am Chem Soc* **133**, 18042–18045 (2011).

35. Kim, H.-S. *et al.* Lead Iodide Perovskite Sensitized All-Solid-State Submicron Thin Film Mesoscopic Solar Cell with Efficiency Exceeding 9%. *Sci Rep* **2**, 591 (2012).

36. Lee, M. M., Teuscher, J., Miyasaka, T., Murakami, T. N. & Snaith, H. J. Efficient Hybrid Solar Cells Based on Meso-Superstructured Organometal Halide Perovskites. *Science (1979)* **338**, 643–647 (2012).

37. Liu, M., Johnston, M. B. & Snaith, H. J. Efficient planar heterojunction perovskite solar cells by vapour deposition. *Nature* **501**, 395–398 (2013).

38. Jeng, J. Y. *et al.* CH3NH3PbI3 perovskite/fullerene planar-heterojunction hybrid solar cells. *Advanced Materials* **25**, 3727–3732 (2013).

39. Docampo, P., Ball, J. M., Darwich, M., Eperon, G. E. & Snaith, H. J. Efficient organometal trihalide perovskite planar-heterojunction solar cells on flexible polymer substrates. *Nat Commun* **4**, (2013).

40. Shao, Y., Xiao, Z., Bi, C., Yuan, Y. & Huang, J. Origin and elimination of photocurrent hysteresis by fullerene passivation in CH3NH3PbI3 planar heterojunction solar cells. *Nat Commun* **5**, (2014).

41. Lin, Q., Armin, A., Nagiri, R. C. R., Burn, P. L. & Meredith, P. Electro-optics of perovskite solar cells. *Nat Photonics* **9**, 106–112 (2015).

42. Zheng, X. *et al.* Defect passivation in hybrid perovskite solar cells using quaternary ammonium halide anions and cations. *Nat Energy* **2**, (2017).

43. Luo, D. *et al.* Enhanced photovoltage for inverted planar heterojunction perovskite solar cells. *Science (1979)* **360**, 1442–1446 (2018).

44. Zheng, X. *et al.* Managing grains and interfaces via ligand anchoring enables

22.3%-efficiency inverted perovskite solar cells. *Nat Energy* **5**, 131–140 (2020).

45. Li, F. *et al.* Regulating Surface Termination for Efficient Inverted Perovskite Solar Cells with Greater Than 23% Efficiency. *J Am Chem Soc* **142**, 20134–20142 (2020).

46. Chen, S. *et al. Stabilizing perovskite-substrate interfaces for high-performance perovskite modules*. *Science* vol. 373 https://www.science.org (2021).

47. Li, X. *et al.* Constructing heterojunctions by surface sulfidation for efficient inverted perovskite solar cells. *Science (1979)* **375**, 434–437 (2022).

48. Chen, H. *et al.* Quantum-size-tuned heterostructures enable efficient and stable inverted perovskite solar cells. *Nat Photonics* **16**, 352–358 (2022).

49. Azmi, R. *et al.* Damp heat-stable perovskite solar cells with tailored-dimensionality 2D/3D heterojunctions. *Science (1979)* **376**, 73–77 (2022).

50. Zhang, S. *et al.* Minimizing buried interfacial defects for efficient inverted perovskite solar cells. *Science (1979)* **380**, 404–409 (2023).

51. Peng, W. *et al.* Reducing nonradiative recombination in perovskite solar cells with a porous insulator contact. *Science (1979)* **379**, 683–690 (2023).

52. Tan, Q. *et al.* Inverted perovskite solar cells using dimethylacridine-based dopants. *Nature* (2023) doi:10.1038/s41586-023-06207-0.

53. Park, J. *et al.* Controlled growth of perovskite layers with volatile alkylammonium chlorides. *Nature* **616**, 724–730 (2023).

54. NREL. NREL cell efficiency chart. https://www.nrel.gov/pv/cell-efficiency.html.

55. Luo, D. *et al.* Dual-Source Precursor Approach for Highly Efficient Inverted Planar Heterojunction Perovskite Solar Cells. *Advanced Materials* **29**, 1604758 (2017).

56. Chen, W. *et al.* Efficient and stable large-area perovskite solar cells with

inorganic charge extraction layers. *Science (1979)* **350**, 944–948 (2015).

57. Price, M. B. *et al.* Hot-carrier cooling and photoinduced refractive index changes in organic–inorganic lead halide perovskites. *Nat Commun* **6**, 8420 (2015).

58. Richter, J. M. *et al.* Ultrafast carrier thermalization in lead iodide perovskite probed with two-dimensional electronic spectroscopy. *Nat Commun* **8**, 376 (2017).

59. Joshi, P. P., Maehrlein, S. F. & Zhu, X. Dynamic Screening and Slow Cooling of Hot Carriers in Lead Halide Perovskites. *Advanced Materials* **31**, 1803054 (2019).

60. Bretschneider, S. A. *et al.* Quantifying Polaron Formation and Charge Carrier Cooling in Lead-Iodide Perovskites. *Advanced Materials* **30**, 1707312 (2018).

61. Yang, Y. *et al.* Observation of a hot-phonon bottleneck in lead-iodide perovskites. *Nat Photonics* **10**, 53–59 (2016).

62. Wang, K. *et al.* Overcoming Shockley-Queisser limit using halide perovskite platform? *Joule* **6**, 756–771 (2022).

63. Huang, J., Yuan, Y., Shao, Y. & Yan, Y. Understanding the physical properties of hybrid perovskites for photovoltaic applications. *Nat Rev Mater* **2**, 17042 (2017).

64. Bridgman, P. W. Note on the Principle of Detailed Balancing. *Physical Review* **31**, 101–102 (1928).

65. Johnston, M. B. & Herz, L. M. Hybrid Perovskites for Photovoltaics: Charge-Carrier Recombination, Diffusion, and Radiative Efficiencies. *Acc Chem Res* **49**, 146–154 (2016).

66. Stranks, S. D., Hoye, R. L. Z., Di, D., Friend, R. H. & Deschler, F. The Physics of Light Emission in Halide Perovskite Devices. *Advanced Materials* **31**, 1803336 (2019).

67. Richter, J. M. *et al.* Enhancing photoluminescence yields in lead halide perovskites by photon recycling and light out-coupling. *Nat Commun* **7**, 13941 (2016).

68. Yuan, Y. *et al.* Electric-Field-Driven Reversible Conversion Between Methylammonium Lead Triiodide Perovskites and Lead Iodide at Elevated Temperatures. *Adv Energy Mater* **6**, 1501803 (2016).

69. Eames, C. *et al.* Ionic transport in hybrid lead iodide perovskite solar cells. *Nat Commun* **6**, 7497 (2015).

70. Hoke, E. T. *et al.* Reversible photo-induced trap formation in mixed-halide hybrid perovskites for photovoltaics. *Chem Sci* **6**, 613–617 (2015).

71. Brennan, M. C., Draguta, S., Kamat, P. v. & Kuno, M. Light-Induced Anion Phase Segregation in Mixed Halide Perovskites. *ACS Energy Lett* **3**, 204–213 (2018).

72. Slotcavage, D. J., Karunadasa, H. I. & McGehee, M. D. Light-Induced Phase Segregation in Halide-Perovskite Absorbers. *ACS Energy Lett* **1**, 1199–1205 (2016).

73. Zhang, T. *et al.* Profiling the organic cation-dependent degradation of organolead halide perovskite solar cells. *J Mater Chem A Mater* **5**, 1103–1111 (2017).

74. Carrillo, J. *et al.* Ionic Reactivity at Contacts and Aging of Methylammonium Lead Triiodide Perovskite Solar Cells. *Adv Energy Mater* **6**, 1502246 (2016).

75. Besleaga, C. *et al.* Iodine Migration and Degradation of Perovskite Solar Cells Enhanced by Metallic Electrodes. *J Phys Chem Lett* **7**, 5168–5175 (2016).

76. Kato, Y. *et al.* Silver Iodide Formation in Methyl Ammonium Lead Iodide Perovskite Solar Cells with Silver Top Electrodes. *Adv Mater Interfaces* **2**, 1500195 (2015).

77. Zhang, T. *et al.* Profiling the organic cation-dependent degradation of organolead halide perovskite solar cells. *J Mater Chem A Mater* **5**, 1103–1111 (2017).

78. Guo, X. *et al.* The compatibility of methylammonium and formamidinium in mixed cation perovskite: the optoelectronic and stability properties. *Nanotechnology* **32**, 075406 (2021).

79. Pavlovetc, I. M. *et al.* Suppressing Cation Migration in Triple-Cation Lead Halide Perovskites. *ACS Energy Lett* **5**, 2802–2810 (2020).

80. Chatterjee, R., Pavlovetc, I. M., Aleshire, K., Hartland, G. v. & Kuno, M. Subdiffraction Infrared Imaging of Mixed Cation Perovskites: Probing Local Cation Heterogeneities. *ACS Energy Lett* **3**, 469–475 (2018).

81. Bella, F., Renzi, P., Cavallo, C. & Gerbaldi, C. Caesium for Perovskite Solar Cells: An Overview. *Chemistry - A European Journal* **24**, 12183–12205 (2018).

82. Chen, J. *et al.* Mixed-Organic-Cation $(FA)_x(MA)_{1-x}PbI_3$ Planar Perovskite Solar Cells with 16.48% Efficiency via a Low-Pressure Vapor-Assisted Solution Process. *ACS Appl Mater Interfaces* **9**, 2449–2458 (2017).

83. Lee, J.-W. *et al.* Formamidinium and Cesium Hybridization for Photo- and Moisture-Stable Perovskite Solar Cell. *Adv Energy Mater* **5**, 1501310 (2015).

84. Jiang, L.-L. *et al.* Flower-like MoS_2 nanocrystals: a powerful sorbent of Li^+ in the Spiro-OMeTAD layer for highly efficient and stable perovskite solar cells. *J Mater Chem A Mater* **7**, 3655–3663 (2019).

85. Dawson, J. A. *et al.* Mechanisms of Lithium Intercalation and Conversion Processes in Organic–Inorganic Halide Perovskites. *ACS Energy Lett* **2**, 1818–1824 (2017).

86. Leguy, A. M. A. *et al.* Reversible Hydration of $CH_3NH_3PbI_3$ in Films, Single Crystals, and Solar Cells. *Chemistry of Materials* **27**, 3397–3407 (2015).

87. Leijtens, T. *et al.* Hydrophobic Organic Hole Transporters for Improved Moisture Resistance in Metal Halide Perovskite Solar Cells. *ACS Appl Mater Interfaces* **8**, 5981–5989 (2016).

88. Ding, C. *et al.* Synergetic effects of electrochemical oxidation of Spiro-OMeTAD and Li^+ ion migration for improving the performance of n–i–p type perovskite solar cells. *J Mater Chem A Mater* **9**, 7575–7585 (2021).

89. Zhang, J. *et al.* Extrinsic Movable Ions in $MAPbI_3$ Modulate Energy Band Alignment in Perovskite Solar Cells. *Adv Energy Mater* **8**, 1701981 (2018).

90. Li, Z. *et al.* Extrinsic ion migration in perovskite solar cells. *Energy Environ Sci* **10**, 1234–1242 (2017).

91. Ceratti, D. R. *et al.* Eppur si Muove: Proton Diffusion in Halide Perovskite Single Crystals. *Advanced Materials* **32**, 2002467 (2020).

92. Sadhu, S., Buffeteau, T., Sandrez, S., Hirsch, L. & Bassani, D. M. Observing the Migration of Hydrogen Species in Hybrid Perovskite Materials through D/H Isotope Exchange. *J Am Chem Soc* **142**, 10431–10437 (2020).

93. Domanski, K. *et al.* Not All That Glitters Is Gold: Metal-Migration-Induced Degradation in Perovskite Solar Cells. *ACS Nano* **10**, 6306–6314 (2016).

94. Sultana, N., Demarais, N. J., Shevchenko, D. & Derrick, P. J. Laser Desorption/Ionization Mass Spectrometry of Perovskite Solar Cells: Identification of Interface Interactions and Degradation Reactions. *Solar RRL* **2**, 1800022 (2018).

95. Zhang, T. *et al.* Profiling the organic cation-dependent degradation of organolead halide perovskite solar cells. *J Mater Chem A Mater* **5**, 1103–1111 (2017).

96. Lu, Y., Ge, Y. & Sui, M. Different Degradation Mechanism of $CH_3NH_3PbI_3$ Based Perovskite Solar Cells under Ultraviolet and Visible Light Illumination.

Acta Chimi Sin **79**, 344 (2021).

97. Pospisil, J. *et al.* Reversible Formation of Gold Halides in Single-Crystal Hybrid-Perovskite/Au Interface upon Biasing and Effect on Electronic Carrier Injection. *Adv Funct Mater* **29**, 1900881 (2019).

98. Drozdov, M. N., Yunin, P. A., Travkin, V. v., Koptyaev, A. I. & Pakhomov, G. L. Direct Imaging of Current-Induced Transformation of a Perovskite/Electrode Interface. *Adv Mater Interfaces* **6**, 1900364 (2019).

99. Ming, W., Yang, D., Li, T., Zhang, L. & Du, M. Formation and Diffusion of Metal Impurities in Perovskite Solar Cell Material $CH_3NH_3PbI_3$: Implications on Solar Cell Degradation and Choice of Electrode. *Advanced Science* **5**, 1700662 (2018).

100. Kerner, R. A. *et al.* Low Threshold Voltages Electrochemically Drive Gold Migration in Halide Perovskite Devices. *ACS Energy Lett* **5**, 3352–3356 (2020).

101. Bai, S. *et al.* Planar perovskite solar cells with long-term stability using ionic liquid additives. *Nature* **571**, 245–250 (2019).

102. Domanski, K. *et al.* Not All That Glitters Is Gold: Metal-Migration-Induced Degradation in Perovskite Solar Cells. *ACS Nano* **10**, 6306–6314 (2016).

103. Wu, S. *et al.* A chemically inert bismuth interlayer enhances long-term stability of inverted perovskite solar cells. *Nat Commun* **10**, 1161 (2019).

104. Kaltenbrunner, M. *et al.* Flexible high power-per-weight perovskite solar cells with chromium oxide–metal contacts for improved stability in air. *Nat Mater* **14**, 1032–1039 (2015).

105. Dong, X. *et al.* Improvement of the humidity stability of organic–inorganic perovskite solar cells using ultrathin Al_2O_3 layers prepared by atomic layer deposition. *J Mater Chem A Mater* **3**, 5360–5367 (2015).

106. Sanehira, E. M. *et al.* Influence of Electrode Interfaces on the Stability of Perovskite Solar Cells: Reduced Degradation Using MoO_x/Al for Hole Collection. *ACS Energy Lett* **1**, 38–45 (2016).

107. Snaith, H. J. *et al.* Anomalous Hysteresis in Perovskite Solar Cells. *J Phys Chem Lett* **5**, 1511–1515 (2014).

108. Kang, D. & Park, N. On the Current–Voltage Hysteresis in Perovskite Solar Cells: Dependence on Perovskite Composition and Methods to Remove Hysteresis. *Advanced Materials* **31**, 1805214 (2019).

109. Kim, H.-S. *et al.* Control of $I-V$ Hysteresis in $CH_3NH_3PbI_3$ Perovskite Solar Cell. *J Phys Chem Lett* **6**, 4633–4639 (2015).

110. Cojocaru, L. *et al.* Origin of the Hysteresis in $I-V$ Curves for Planar Structure Perovskite Solar Cells Rationalized with a Surface Boundary-induced Capacitance Model. *Chem Lett* **44**, 1750–1752 (2015).

111. Lu, Q. *et al.* A Review on Encapsulation Technology from Organic Light Emitting Diodes to Organic and Perovskite Solar Cells. *Adv Funct Mater* **31**, 2100151 (2021).

112. Ma, S. *et al.* Development of encapsulation strategies towards the commercialization of perovskite solar cells. *Energy Environ Sci* **15**, 13–55 (2022).

113. Chen, H. *et al.* Regulating surface potential maximizes voltage in all-perovskite tandems. *Nature* **613**, 676–681 (2023).

114. Jiang, Q. *et al.* Compositional texture engineering for highly stable wide-bandgap perovskite solar cells. *Science (1979)* **378**, 1295–1300 (2022).

115. Noh, J. H., Im, S. H., Heo, J. H., Mandal, T. N. & Seok, S. Il. Chemical Management for Colorful, Efficient, and Stable Inorganic–Organic Hybrid

Nanostructured Solar Cells. *Nano Lett* **13**, 1764–1769 (2013).

116. Eperon, G. E. *et al.* Formamidinium lead trihalide: a broadly tunable perovskite for efficient planar heterojunction solar cells. *Energy Environ Sci* **7**, 982 (2014).

117. Bi, C., Yuan, Y., Fang, Y. & Huang, J. Low-Temperature Fabrication of Efficient Wide-Bandgap Organolead Trihalide Perovskite Solar Cells. *Adv Energy Mater* **5**, 1401616 (2015).

118. Hu, M., Bi, C., Yuan, Y., Bai, Y. & Huang, J. Stabilized Wide Bandgap MAPbBr $_x$ I $_{3-x}$ Perovskite by Enhanced Grain Size and Improved Crystallinity. *Advanced Science* **3**, 1500301 (2016).

119. Zhu, W. *et al.* An efficient planar-heterojunction solar cell based on wide-bandgap CH $_3$ NH $_3$ PbI $_{2.1}$ Br $_{0.9}$ perovskite film for tandem cell application. *Chemical Communications* **52**, 304–307 (2016).

120. Yang, Z. *et al.* Stabilized Wide Bandgap Perovskite Solar Cells by Tin Substitution. *Nano Lett* **16**, 7739–7747 (2016).

121. McMeekin, D. P. *et al.* A mixed-cation lead mixed-halide perovskite absorber for tandem solar cells. *Science (1979)* **351**, 151–155 (2016).

122. Lin, Y. *et al.* Matching Charge Extraction Contact for Wide-Bandgap Perovskite Solar Cells. *Advanced Materials* **29**, 1700607 (2017).

123. Bush, K. A. *et al.* Compositional Engineering for Efficient Wide Band Gap Perovskites with Improved Stability to Photoinduced Phase Segregation. *ACS Energy Lett* **3**, 428–435 (2018).

124. Lin, R. *et al.* Monolithic all-perovskite tandem solar cells with 24.8% efficiency exploiting comproportionation to suppress Sn(ii) oxidation in precursor ink. *Nat Energy* **4**, 864–873 (2019).

125. Chen, C. *et al.* Achieving a high open-circuit voltage in inverted wide-bandgap

perovskite solar cells with a graded perovskite homojunction. *Nano Energy* **61**, 141–147 (2019).

126. Yu, Z. *et al.* Simplified interconnection structure based on C60/SnO2-x for all-perovskite tandem solar cells. *Nat Energy* **5**, 657–665 (2020).

127. Chen, W. *et al.* Monolithic perovskite/organic tandem solar cells with 23.6% efficiency enabled by reduced voltage losses and optimized interconnecting layer. *Nat Energy* **7**, 229–237 (2022).

128. Wang, C. *et al.* A universal close-space annealing strategy towards high-quality perovskite absorbers enabling efficient all-perovskite tandem solar cells. *Nat Energy* **7**, 744–753 (2022).

129. Wen, J. *et al.* Steric Engineering Enables Efficient and Photostable Wide-Bandgap Perovskites for All-Perovskite Tandem Solar Cells. *Advanced Materials* 2110356 (2022) doi:10.1002/adma.202110356.

130. Lin, R. *et al.* All-perovskite tandem solar cells with improved grain surface passivation. *Nature* **603**, 73–78 (2022).

131. Lin, R. *et al.* All-perovskite tandem solar cells with 3D/3D bilayer perovskite heterojunction. *Nature* **620**, 994–1000 (2023).

132. He, R. *et al.* Improving interface quality for 1-cm2 all-perovskite tandem solar cells. *Nature* **618**, 80–86 (2023).

133. Hoke, E. T. *et al.* Reversible photo-induced trap formation in mixed-halide hybrid perovskites for photovoltaics. *Chem Sci* **6**, 613–617 (2015).

134. Conings, B. *et al.* Intrinsic Thermal Instability of Methylammonium Lead Trihalide Perovskite. *Adv Energy Mater* **5**, 1500477 (2015).

135. Stranks, S. D. & Snaith, H. J. Metal-halide perovskites for photovoltaic and light-emitting devices. *Nat Nanotechnol* **10**, 391–402 (2015).

136. Pellet, N. *et al.* Mixed-Organic-Cation Perovskite Photovoltaics for Enhanced Solar-Light Harvesting. *Angewandte Chemie International Edition* **53**, 3151–3157 (2014).

137. Stoumpos, C. C., Malliakas, C. D. & Kanatzidis, M. G. Semiconducting Tin and Lead Iodide Perovskites with Organic Cations: Phase Transitions, High Mobilities, and Near-Infrared Photoluminescent Properties. *Inorg Chem* **52**, 9019–9038 (2013).

138. Pang, S. *et al.* $NH_2CH{=}NH_2PbI_3$: An Alternative Organolead Iodide Perovskite Sensitizer for Mesoscopic Solar Cells. *Chemistry of Materials* **26**, 1485–1491 (2014).

139. Binek, A., Hanusch, F. C., Docampo, P. & Bein, T. Stabilization of the Trigonal High-Temperature Phase of Formamidinium Lead Iodide. *J Phys Chem Lett* **6**, 1249–1253 (2015).

140. Eperon, G. E. *et al.* Formamidinium lead trihalide: a broadly tunable perovskite for efficient planar heterojunction solar cells. *Energy Environ Sci* **7**, 982 (2014).

141. Yu, Y. *et al.* Synergistic Effects of Lead Thiocyanate Additive and Solvent Annealing on the Performance of Wide-Bandgap Perovskite Solar Cells. *ACS Energy Lett* **2**, 1177–1182 (2017).

142. Zhou, Y. *et al.* Composition-Tuned Wide Bandgap Perovskites: From Grain Engineering to Stability and Performance Improvement. *Adv Funct Mater* **28**, 1803130 (2018).

143. Abdi-Jalebi, M. *et al.* Maximizing and stabilizing luminescence from halide perovskites with potassium passivation. *Nature* **555**, 497–501 (2018).

144. Kim, J. *et al.* Amide-Catalyzed Phase-Selective Crystallization Reduces Defect Density in Wide-Bandgap Perovskites. *Advanced Materials* **30**, 1706275 (2018).

145. Jiang, Q. *et al.* Surface passivation of perovskite film for efficient solar cells. *Nat Photonics* **13**, 460–466 (2019).

146. Moghadamzadeh, S. *et al.* Spontaneous enhancement of the stable power conversion efficiency in perovskite solar cells. *J Mater Chem A Mater* **8**, 670–682 (2020).

147. Zhou, Y. *et al.* Benzylamine-Treated Wide-Bandgap Perovskite with High Thermal-Photostability and Photovoltaic Performance. *Adv Energy Mater* **7**, 1701048 (2017).

148. Belisle, R. A. *et al.* Impact of Surfaces on Photoinduced Halide Segregation in Mixed-Halide Perovskites. *ACS Energy Lett* **3**, 2694–2700 (2018).

149. Jaysankar, M. *et al.* Minimizing Voltage Loss in Wide-Bandgap Perovskites for Tandem Solar Cells. *ACS Energy Lett* **4**, 259–264 (2019).

150. Sadhanala, A. *et al.* Preparation of Single-Phase Films of $CH_3NH_3Pb(I_{1-x}Br_x)_3$ with Sharp Optical Band Edges. *J Phys Chem Lett* **5**, 2501–2505 (2014).

151. Zhou, Y., Poli, I., Meggiolaro, D., De Angelis, F. & Petrozza, A. Defect activity in metal halide perovskites with wide and narrow bandgap. *Nat Rev Mater* **6**, 986–1002 (2021).

152. Lin, Y. *et al.* Matching Charge Extraction Contact for Wide-Bandgap Perovskite Solar Cells. *Advanced Materials* **29**, 1700607 (2017).

153. Kallmann, H. & Pope, M. Photovoltaic Effect in Organic Crystals. *J Chem Phys* **30**, 585–586 (1959).

154. Deibel, C. *et al.* Energetics of excited states in the conjugated polymer poly(3-hexylthiophene). *Phys Rev B* **81**, 085202 (2010).

155. Tang, C. W. Two-layer organic photovoltaic cell. *Appl Phys Lett* **48**, 183–185 (1986).

156. Yu, G., Gao, J., Hummelen, J. C., Wudl, F. & Heeger, A. J. Polymer Photovoltaic Cells: Enhanced Efficiencies via a Network of Internal Donor-Acceptor Heterojunctions. *Science (1979)* **270**, 1789–1791 (1995).

157. Kumari, T., Lee, S. M., Kang, S.-H., Chen, S. & Yang, C. Ternary solar cells with a mixed face-on and edge-on orientation enable an unprecedented efficiency of 12.1%. *Energy Environ Sci* **10**, 258–265 (2017).

158. Zhang, J., Tan, H. S., Guo, X., Facchetti, A. & Yan, H. Material insights and challenges for non-fullerene organic solar cells based on small molecular acceptors. *Nat Energy* **3**, 720–731 (2018).

159. Xiao, Z. *et al.* 26 mA cm−2 Jsc from organic solar cells with a low-bandgap nonfullerene acceptor. *Sci Bull (Beijing)* **62**, 1494–1496 (2017).

160. Yuan, J. *et al.* Single-Junction Organic Solar Cell with over 15% Efficiency Using Fused-Ring Acceptor with Electron-Deficient Core. *Joule* **3**, 1140–1151 (2019).

161. Zhang, G. *et al.* Delocalization of exciton and electron wavefunction in non-fullerene acceptor molecules enables efficient organic solar cells. *Nat Commun* **11**, 3943 (2020).

162. Wu, J. *et al.* Exceptionally low charge trapping enables highly efficient organic bulk heterojunction solar cells. *Energy Environ Sci* **13**, 2422–2430 (2020).

163. Li, C. *et al.* Non-fullerene acceptors with branched side chains and improved molecular packing to exceed 18% efficiency in organic solar cells. *Nat Energy* **6**, 605–613 (2021).

164. Li, Y. *et al.* Mechanism study on organic ternary photovoltaics with 18.3% certified efficiency: from molecule to device. *Energy Environ Sci* **15**, 855–865 (2022).

165. Gao, W. *et al.* Achieving 19% Power Conversion Efficiency in Planar-Mixed Heterojunction Organic Solar Cells Using a Pseudosymmetric Electron Acceptor. *Advanced Materials* **34**, 2202089 (2022).

166. Shaheen, S. E., Radspinner, R., Peyghambarian, N. & Jabbour, G. E. Fabrication of bulk heterojunction plastic solar cells by screen printing. *Appl Phys Lett* **79**, 2996–2998 (2001).

167. Li, G. *et al.* High-efficiency solution processable polymer photovoltaic cells by self-organization of polymer blends. *Nat Mater* **4**, 864–868 (2005).

168. Liang, Y. *et al.* For the Bright Future-Bulk Heterojunction Polymer Solar Cells with Power Conversion Efficiency of 7.4%. *Advanced Materials* **22**, E135–E138 (2010).

169. He, Z. *et al.* Enhanced power-conversion efficiency in polymer solar cells using an inverted device structure. *Nat Photonics* **6**, 591–595 (2012).

170. Liao, S.-H., Jhuo, H.-J., Cheng, Y.-S. & Chen, S.-A. Fullerene Derivative-Doped Zinc Oxide Nanofilm as the Cathode of Inverted Polymer Solar Cells with Low-Bandgap Polymer (PTB7-Th) for High Performance. *Advanced Materials* **25**, 4766–4771 (2013).

171. Zhao, J. *et al.* Efficient organic solar cells processed from hydrocarbon solvents. *Nat Energy* **1**, 15027 (2016).

172. Cui, Y. *et al.* Organic photovoltaic cell with 17% efficiency and superior processability. *Natl Sci Rev* **7**, 1239–1246 (2020).

173. Liu, Q. *et al.* 18% Efficiency organic solar cells. *Sci Bull (Beijing)* **65**, 272–275 (2020).

174. Cai, Y. *et al.* A Well-Mixed Phase Formed by Two Compatible Non-Fullerene Acceptors Enables Ternary Organic Solar Cells with Efficiency over 18.6%.

Advanced Materials **33**, (2021).

175. Gao, W. *et al.* Achieving 19% Power Conversion Efficiency in Planar-Mixed Heterojunction Organic Solar Cells Using a Pseudosymmetric Electron Acceptor. *Advanced Materials* **34**, (2022).

176. Xu, X. *et al.* Sequential Deposition of Multicomponent Bulk Heterojunctions Increases Efficiency of Organic Solar Cells. *Advanced Materials* **35**, (2023).

177. Armin, A. *et al.* A History and Perspective of Non-Fullerene Electron Acceptors for Organic Solar Cells. *Adv Energy Mater* **11**, 2003570 (2021).

178. Zhang, G. *et al.* Nonfullerene Acceptor Molecules for Bulk Heterojunction Organic Solar Cells. *Chem Rev* **118**, 3447–3507 (2018).

179. Brédas, J.-L., Norton, J. E., Cornil, J. & Coropceanu, V. Molecular Understanding of Organic Solar Cells: The Challenges. *Acc Chem Res* **42**, 1691–1699 (2009).

180. Scharber, M. C. & Sariciftci, N. S. Efficiency of bulk-heterojunction organic solar cells. *Prog Polym Sci* **38**, 1929–1940 (2013).

181. Marcus, R. A. Electron Transfer Reactions in Chemistry: Theory and Experiment (Nobel Lecture). *Angewandte Chemie International Edition in English* **32**, 1111–1121 (1993).

182. Zhao, J. *et al.* Efficient organic solar cells processed from hydrocarbon solvents. *Nat Energy* **1**, 15027 (2016).

183. Liu, Y. *et al.* Aggregation and morphology control enables multiple cases of high-efficiency polymer solar cells. *Nat Commun* **5**, 5293 (2014).

184. Baran, D. *et al.* Reduced voltage losses yield 10% efficient fullerene free organic solar cells with >1 V open circuit voltages. *Energy Environ Sci* **9**, 3783–3793 (2016).

185. Chen, S. *et al.* A Wide-Bandgap Donor Polymer for Highly Efficient Non-fullerene Organic Solar Cells with a Small Voltage Loss. *J Am Chem Soc* **139**, 6298–6301 (2017).

186. Cheng, P. *et al.* Realizing Small Energy Loss of 0.55 eV, High Open-Circuit Voltage >1 V and High Efficiency >10% in Fullerene-Free Polymer Solar Cells via Energy Driver. *Advanced Materials* **29**, 1605216 (2017).

187. Liu, J. *et al.* Fast charge separation in a non-fullerene organic solar cell with a small driving force. *Nat Energy* **1**, 16089 (2016).

188. Yao, J. *et al.* Quantifying Losses in Open-Circuit Voltage in Solution-Processable Solar Cells. *Phys Rev Appl* **4**, 014020 (2015).

189. Yao, J. *et al.* Quantifying Losses in Open-Circuit Voltage in Solution-Processable Solar Cells. *Phys Rev Appl* **4**, 014020 (2015).

190. Zhang, G. *et al.* Renewed Prospects for Organic Photovoltaics. *Chem Rev* **122**, 14180–14274 (2022).

191. Gillett, A. J. *et al.* The role of charge recombination to triplet excitons in organic solar cells. *Nature* **597**, 666–671 (2021).

192. Chow, P. C. Y. *et al.* Factors That Prevent Spin-Triplet Recombination in Non-fullerene Organic Photovoltaics. *J Phys Chem Lett* **12**, 5045–5051 (2021).

193. Chen, Z. *et al.* Triplet exciton formation for non-radiative voltage loss in high-efficiency nonfullerene organic solar cells. *Joule* **5**, 1832–1844 (2021).

194. Hörantner, M. T. *et al.* The Potential of Multijunction Perovskite Solar Cells. *ACS Energy Lett* **2**, 2506–2513 (2017).

195. NREL. NREL Pv Research Cell Record Efficiency Chart. *https://www.nrel.gov/pv/assets/pdfs/cell-pv-eff-emergingpv-rev220630.pdf*.

196. Mailoa, J. P. *et al.* A 2-terminal perovskite/silicon multijunction solar cell

enabled by a silicon tunnel junction. *Appl Phys Lett* **106**, 121105 (2015).

197. Werner, J. *et al.* Efficient Monolithic Perovskite/Silicon Tandem Solar Cell with Cell Area >1 cm ^{2}. *J Phys Chem Lett* **7**, 161–166 (2016).

198. Werner, J. *et al.* Zinc tin oxide as high-temperature stable recombination layer for mesoscopic perovskite/silicon monolithic tandem solar cells. *Appl Phys Lett* **109**, 233902 (2016).

199. Albrecht, S. *et al.* Monolithic perovskite/silicon-heterojunction tandem solar cells processed at low temperature. *Energy Environ Sci* **9**, 81–88 (2016).

200. Zheng, J. *et al.* 21.8% Efficient Monolithic Perovskite/Homo-Junction-Silicon Tandem Solar Cell on 16 cm ^{2}. *ACS Energy Lett* **3**, 2299–2300 (2018).

201. Jena, A. K., Numata, Y., Ikegami, M. & Miyasaka, T. Role of spiro-OMeTAD in performance deterioration of perovskite solar cells at high temperature and reuse of the perovskite films to avoid Pb-waste. *J Mater Chem A Mater* **6**, 2219–2230 (2018).

202. Jung, E. H. *et al.* Efficient, stable and scalable perovskite solar cells using poly(3-hexylthiophene). *Nature* **567**, 511–515 (2019).

203. Bittkau, K., Kirchartz, T. & Rau, U. Optical design of spectrally selective interlayers for perovskite/silicon heterojunction tandem solar cells. *Opt Express* **26**, A750 (2018).

204. Bush, K. A. *et al.* 23.6%-efficient monolithic perovskite/silicon tandem solar cells with improved stability. *Nat Energy* **2**, (2017).

205. Sahli, F. *et al.* Fully textured monolithic perovskite/silicon tandem solar cells with 25.2% power conversion efficiency. *Nat Mater* **17**, 820–826 (2018).

206. Hou, Y. *et al.* Efficient tandem solar cells with solution-processed perovskite on textured crystalline silicon. *Science (1979)* **367**, 1135–1140 (2020).

207. Chen, B. *et al.* Blade-Coated Perovskites on Textured Silicon for 26%-Efficient Monolithic Perovskite/Silicon Tandem Solar Cells. *Joule* **4**, 850–864 (2020).

208. Tockhorn, P. *et al.* Nano-optical designs enhance monolithic perovskite/silicon tandem solar cells toward 29.8% eeciency. doi:10.21203/rs.3.rs-1439562/v1.

209. Leijtens, T., Bush, K. A., Prasanna, R. & McGehee, M. D. Opportunities and challenges for tandem solar cells using metal halide perovskite semiconductors. *Nature Energy* vol. 3 828–838 Preprint at https://doi.org/10.1038/s41560-018-0190-4 (2018).

210. Kim, D. *et al.* Efficient, stable silicon tandem cells enabled by anion-engineered wide-bandgap perovskites. *Science (1979)* **368**, 155–160 (2020).

211. Xu, J. *et al. Triple-halide wide-band gap perovskites with suppressed phase segregation for efficient tandems*. *Science* vol. 367 http://science.sciencemag.org/ (2020).

212. Luo, D., Su, R., Zhang, W., Gong, Q. & Zhu, R. Minimizing non-radiative recombination losses in perovskite solar cells. *Nature Reviews Materials* vol. 5 44–60 Preprint at https://doi.org/10.1038/s41578-019-0151-y (2020).

213. Al-Ashouri, A. *et al. Monolithic perovskite/silicon tandem solar cell with >29% efficiency by enhanced hole extraction*. https://www.science.org.

214. Mariotti, S. *et al.* Interface engineering for high-performance, triple-halide perovskite–silicon tandem solar cells. *Science (1979)* **381**, 63–69 (2023).

215. Chin, X. Y. *et al.* Interface passivation for 31.25%-efficient perovskite/silicon tandem solar cells. *Science (1979)* **381**, 59–63 (2023).

216. Liu, J. *et al.* Efficient and stable perovskite-silicon tandem solar cells through contact displacement by MgF_x. *Science (1979)* **377**, 302–306 (2022).

217. Yang, G. *et al.* Defect engineering in wide-bandgap perovskites for efficient

perovskite–silicon tandem solar cells. *Nat Photonics* **16**, 588–594 (2022).

218. Ningbo Institute of Materials Technology & Engineering Has Developed a New Perovskite/Crystalline Silicon Tandem Solar Cell with an Efficiency of 28.2% Based on TOPCon Substrate Cell with Black Silicon Structure. *Ningbo Institute of Materials Technology & Engineering* Ningbo Institute of Materials Technology & Engineering Has Developed a New Perovskite/Crystalline Silicon Tandem Solar Cell with an Efficiency of 28.2% Based on TOPCon Substrate Cell with Black Silicon Structure. (2021).

219. Oxford Pv Perovskite Solar Cell Achieves 28% Efficiency. https://www.oxfordpv.com/news/oxford-pv-perovskite-solar-cell-achieves-28-efficiency (2018).

220. Wu, Y. *et al.* 27.6% Perovskite/c-Si Tandem Solar Cells Using Industrial Fabricated TOPCon Device. *Adv Energy Mater* 2200821 (2022) doi:10.1002/aenm.202200821.

221. Li, Y. *et al.* Wide Bandgap Interface Layer Induced Stabilized Perovskite/Silicon Tandem Solar Cells with Stability over Ten Thousand Hours. *Adv Energy Mater* **11**, (2021).

222. Li, R. *et al.* $CsPbCl_3$ -Cluster-Widened Bandgap and Inhibited Phase Segregation in a Wide-Bandgap Perovskite and its Application to NiO_x -Based Perovskite/Silicon Tandem Solar Cells. *Advanced Materials* **34**, 2201451 (2022).

223. Nogay, G. *et al.* 25.1%-Efficient monolithic perovskite/silicon tandem solar cell based on a p-type monocrystalline textured silicon wafer and high-temperature passivating contacts. *ACS Energy Lett* **4**, 844–845 (2019).

224. Jiang, F. *et al.* A two-terminal perovskite/perovskite tandem solar cell. *J Mater Chem A Mater* **4**, 1208–1213 (2016).

225. Heo, J. H. & Im, S. H. CH3NH3PbBr3-CH3NH3PbII3 Perovskite-Perovskite Tandem Solar Cells with Exceeding 2.2 V Open Circuit Voltage. *Advanced Materials* **28**, 5121–5125 (2016).

226. Hao, F., Stoumpos, C. C., Cao, D. H., Chang, R. P. H. & Kanatzidis, M. G. Lead-free solid-state organic–inorganic halide perovskite solar cells. *Nat Photonics* **8**, 489–494 (2014).

227. McMeekin, D. P. *et al.* Solution-Processed All-Perovskite Multi-junction Solar Cells. *Joule* **3**, 387–401 (2019).

228. Zhu, R. Inverted devices are catching up. *Nat Energy* **5**, 123–124 (2020).

229. Eperon, G. E. *et al.* Perovskite-perovskite tandem photovoltaics with optimized band gaps. *Science (1979)* **354**, 861–865 (2016).

230. Zhao, D. *et al.* Efficient two-terminal all-perovskite tandem solar cells enabled by high-quality low-bandgap absorber layers. *Nat Energy* **3**, 1093–1100 (2018).

231. Tong, J. *et al.* Carrier lifetimes of >1 ms in Sn-Pb perovskites enable efficient all-perovskite tandem solar cells. *Science (1979)* **364**, 475–479 (2019).

232. Xiao, K. *et al.* All-perovskite tandem solar cells with 24.2% certified efficiency and area over 1 cm2 using surface-anchoring zwitterionic antioxidant. *Nat Energy* **5**, 870–880 (2020).

233. Yang, Z. *et al.* Enhancing electron diffusion length in narrow-bandgap perovskites for efficient monolithic perovskite tandem solar cells. *Nat Commun* **10**, (2019).

234. Lin, R. *et al.* All-perovskite tandem solar cells with 3D/3D bilayer perovskite heterojunction. *Nature* **620**, 994–1000 (2023).

235. Yu, Z. *et al.* Gradient Doping in Sn–Pb Perovskites by Barium Ions for Efficient Single-Junction and Tandem Solar Cells. *Advanced Materials* **34**, (2022).

236. Tong, J. *et al.* Carrier control in Sn–Pb perovskites via 2D cation engineering for all-perovskite tandem solar cells with improved efficiency and stability. *Nat Energy* (2022) doi:10.1038/s41560-022-01046-1.

237. Brinkmann, K. O. *et al.* Perovskite–organic tandem solar cells with indium oxide interconnect. *Nature* **604**, 280–286 (2022).

238. Chen, W. *et al.* Monolithic perovskite/organic tandem solar cells with 23.6% efficiency enabled by reduced voltage losses and optimized interconnecting layer. *Nat Energy* **7**, 229–237 (2022).

239. Palmstrom, A. F. *et al.* Enabling Flexible All-Perovskite Tandem Solar Cells. *Joule* **3**, 2193–2204 (2019).

240. Qin, S. *et al.* Constructing Monolithic Perovskite/Organic Tandem Solar Cell with Efficiency of 22.0% via Reduced Open-Circuit Voltage Loss and Broadened Absorption Spectra. *Advanced Materials* **34**, (2022).

241. Xie, Y. M. *et al.* Homogeneous Grain Boundary Passivation in Wide-Bandgap Perovskite Films Enables Fabrication of Monolithic Perovskite/Organic Tandem Solar Cells with over 21% Efficiency. *Adv Funct Mater* **32**, (2022).

242. Chen, X. *et al.* Efficient and Reproducible Monolithic Perovskite/Organic Tandem Solar Cells with Low-Loss Interconnecting Layers. *Joule* **4**, 1594–1606 (2020).

243. Liu, Y. *et al.* High Efficiency Tandem Thin-Perovskite/Polymer Solar Cells with a Graded Recombination Layer. *ACS Appl Mater Interfaces* **8**, 7070–7076 (2016).

244. Liu, Y. *et al.* Recent progress in organic solar cells (Part I material science). *Sci China Chem* **65**, 224–268 (2022).

245. Liu, Y. & Chen, Y. Integrated Perovskite/Bulk-Heterojunction Organic Solar Cells. *Advanced Materials* **32**, 1–11 (2020).

246. Chen, C. C. *et al.* Perovskite/polymer monolithic hybrid tandem solar cells utilizing a low-temperature, full solution process. *Mater Horiz* **2**, 203–211 (2015).

247. Fu, H. *et al.* A Top-Down Strategy to Engineer ActiveLayer Morphology for Highly Efficient and Stable All-Polymer Solar Cells. *Advanced Materials* **34**, (2022).

248. Crisp, R. W. *et al.* Tandem Solar Cells from Solution-Processed CdTe and PbS Quantum Dots Using a ZnTe–ZnO Tunnel Junction. *Nano Lett* **17**, 1020–1027 (2017).

249. Pettersson, L. A. A., Roman, L. S. & Inganäs, O. Modeling photocurrent action spectra of photovoltaic devices based on organic thin films. *J Appl Phys* **86**, 487–496 (1999).

250. Burkhard, G. F., Hoke, E. T. & McGehee, M. D. Accounting for Interference, Scattering, and Electrode Absorption to Make Accurate Internal Quantum Efficiency Measurements in Organic and Other Thin Solar Cells. *Advanced Materials* **22**, 3293–3297 (2010).

251. Ayadi, Z. Ben, El Mir, L., Djessas, K. & Alaya, S. The properties of aluminum-doped zinc oxide thin films prepared by rf-magnetron sputtering from nanopowder targets. *Materials Science and Engineering: C* **28**, 613–617 (2008).

252. Van Toan, N., Tuoi, T. T. K., Inomata, N., Toda, M. & Ono, T. Aluminum doped zinc oxide deposited by atomic layer deposition and its applications to micro/nano devices. *Sci Rep* **11**, 1204 (2021).

253. McMeekin, D. P. *et al.* Solution-Processed All-Perovskite Multi-junction Solar Cells. *Joule* **3**, 387–401 (2019).

254. Jiang, Q. *et al.* Surface reaction for efficient and stable inverted perovskite solar

cells. *Nature* **611**, 278–283 (2022).

255. Rau, U. Reciprocity relation between photovoltaic quantum efficiency and electroluminescent emission of solar cells. *Phys Rev B Condens Matter Mater Phys* **76**, (2007).

256. Tauc, J., Grigorovici, R. & Vancu, A. Optical Properties and Electronic Structure of Amorphous Germanium. *physica status solidi (b)* **15**, 627–637 (1966).

257. Melitz, W., Shen, J., Kummel, A. C. & Lee, S. Kelvin probe force microscopy and its application. *Surf Sci Rep* **66**, 1–27 (2011).

258. Pettersson, L. A. A., Roman, L. S. & Inganäs, O. Modeling photocurrent action spectra of photovoltaic devices based on organic thin films. *J Appl Phys* **86**, 487–496 (1999).

259. Zhao, X., Mi, B., Gao, Z. & Huang, W. Recent progress in the numerical modeling for organic thin film solar cells. *Sci China Phys Mech Astron* **54**, 375–387 (2011).

260. Green, M. A. *et al.* Solar cell efficiency tables (Version 60). *Progress in Photovoltaics: Research and Applications* **30**, 687–701 (2022).

261. Song, Z. *et al.* Wide-bandgap, low-bandgap, and tandem perovskite solar cells. *Semiconductor Science and Technology* vol. 34 Preprint at https://doi.org/10.1088/1361-6641/ab27f7 (2019).

262. Oliver, R. D. J. *et al.* Understanding and suppressing non-radiative losses in methylammonium-free wide-bandgap perovskite solar cells. *Energy Environ Sci* **15**, 714–726 (2022).

263. Mahesh, S. *et al.* Revealing the origin of voltage loss in mixed-halide perovskite solar cells. *Energy Environ Sci* **13**, 258–267 (2020).

264. Yang, X. *et al.* Buried Interfaces in Halide Perovskite Photovoltaics. *Advanced*

Materials **33**, (2021).

265. Gharibzadeh, S. *et al.* Record Open-Circuit Voltage Wide-Bandgap Perovskite Solar Cells Utilizing 2D/3D Perovskite Heterostructure. *Adv Energy Mater* **9**, 1803699 (2019).

266. Li, M. H. *et al.* Highly Efficient 2D/3D Hybrid Perovskite Solar Cells via Low-Pressure Vapor-Assisted Solution Process. *Advanced Materials* **30**, (2018).

267. Braunger, S. *et al.* Cs x FA1- xPb(I1- yBr y)3 Perovskite Compositions: The Appearance of Wrinkled Morphology and its Impact on Solar Cell Performance. *Journal of Physical Chemistry C* **122**, 17123–17135 (2018).

268. Bush, K. A. *et al.* Controlling Thin-Film Stress and Wrinkling during Perovskite Film Formation. *ACS Energy Lett* **3**, 1225–1232 (2018).

269. Kim, S. G. *et al.* How antisolvent miscibility affects perovskite film wrinkling and photovoltaic properties. *Nat Commun* **12**, (2021).

270. Stolterfoht, M. *et al.* Approaching the fill factor Shockley–Queisser limit in stable, dopant-free triple cation perovskite solar cells. *Energy Environ Sci* **10**, 1530–1539 (2017).

271. Ma, C. & Park, N.-G. A Realistic Methodology for 30% Efficient Perovskite Solar Cells. *Chem* **6**, 1254–1264 (2020).

272. Peng, J. *et al.* Nanoscale localized contacts for high fill factors in polymer-passivated perovskite solar cells. *Science (1979)* **371**, 390–395 (2021).

273. Chen, K. *et al.* Charge-Carrier Balance for Highly Efficient Inverted Planar Heterojunction Perovskite Solar Cells. *Advanced Materials* **28**, 10718–10724 (2016).

274. Lin, Y. *et al.* Matching Charge Extraction Contact for Wide-Bandgap Perovskite Solar Cells. *Advanced Materials* **29**, 1700607 (2017).

275. Schneider, B. W., Lal, N. N., Baker-Finch, S. & White, T. P. Pyramidal surface textures for light trapping and antireflection in perovskite-on-silicon tandem solar cells. *Opt Express* **22**, A1422 (2014).

276. Shi, B. *et al.* Enhanced light absorption of thin perovskite solar cells using textured substrates. *Solar Energy Materials and Solar Cells* **168**, 214–220 (2017).

277. Stolterfoht, M. *et al.* Visualization and suppression of interfacial recombination for high-efficiency large-area pin perovskite solar cells. *Nat Energy* **3**, 847–854 (2018).

278. Chen, Y. *et al.* Strain engineering and epitaxial stabilization of halide perovskites. *Nature* **577**, 209–215 (2020).

279. Qin, M., Chan, P. F. & Lu, X. A Systematic Review of Metal Halide Perovskite Crystallization and Film Formation Mechanism Unveiled by In Situ GIWAXS. *Advanced Materials* **33**, 2105290 (2021).

280. Wang, K. *et al.* Kinetic Stabilization of the Sol–Gel State in Perovskites Enables Facile Processing of High-Efficiency Solar Cells. *Advanced Materials* **31**, 1808357 (2019).

281. Hu, M., Bi, C., Yuan, Y., Bai, Y. & Huang, J. Stabilized Wide Bandgap MAPbBr $_x$ I $_{3-x}$ Perovskite by Enhanced Grain Size and Improved Crystallinity. *Advanced Science* **3**, 1500301 (2016).

282. McMeekin, D. P. *et al.* Intermediate-phase engineering via dimethylammonium cation additive for stable perovskite solar cells. *Nat Mater* **22**, 73–83 (2023).

283. McMeekin, D. P. *et al.* Crystallization Kinetics and Morphology Control of Formamidinium–Cesium Mixed-Cation Lead Mixed-Halide Perovskite via Tunability of the Colloidal Precursor Solution. *Advanced Materials* **29**, 1607039 (2017).

284. Yang, Z. *et al.* Stabilized Wide Bandgap Perovskite Solar Cells by Tin Substitution. *Nano Lett* **16**, 7739–7747 (2016).

285. Zheng, X. *et al.* Improved Phase Stability of Formamidinium Lead Triiodide Perovskite by Strain Relaxation. *ACS Energy Lett* **1**, 1014–1020 (2016).

286. Wang, J. T.-W. *et al.* Efficient perovskite solar cells by metal ion doping. *Energy Environ Sci* **9**, 2892–2901 (2016).

287. Tripathi, N., Shirai, Y., Yanagida, M., Karen, A. & Miyano, K. Novel Surface Passivation Technique for Low-Temperature Solution-Processed Perovskite PV Cells. *ACS Appl Mater Interfaces* **8**, 4644–4650 (2016).

288. Jeon, N. J. *et al.* Solvent engineering for high-performance inorganic–organic hybrid perovskite solar cells. *Nat Mater* **13**, 897–903 (2014).

289. Zhao, Y. *et al.* Inactive (PbI_2)$_2$RbCl stabilizes perovskite films for efficient solar cells. *Science (1979)* **377**, 531–534 (2022).

290. Snaith, H. J. Present status and future prospects of perovskite photovoltaics. *Nat Mater* **17**, 372–376 (2018).

291. Lin, Y. H. *et al.* A piperidinium salt stabilizes efficient metal-halide perovskite solar cells. *Science (1979)* **369**, 96–102 (2020).

292. Azmi, R. *et al. Damp heat-stable perovskite solar cells with tailored-dimensionality 2D/3D heterojunctions*. https://www.science.org.

293. Macpherson, S. *et al.* Local nanoscale phase impurities are degradation sites in halide perovskites. *Nature* **607**, 294–300 (2022).

294. Guo, R. *et al.* Degradation mechanisms of perovskite solar cells under vacuum and one atmosphere of nitrogen. *Nat Energy* **6**, 977–986 (2021).

295. Nazir, G. *et al.* Stabilization of Perovskite Solar Cells: Recent Developments and Future Perspectives. *Advanced Materials* **34**, 2204380 (2022).

296. Hu, J. *et al.* Tracking the evolution of materials and interfaces in perovskite solar cells under an electric field. *Commun Mater* **3**, 39 (2022).

297. Li, J., Dong, Q., Li, N. & Wang, L. Direct Evidence of Ion Diffusion for the Silver-Electrode-Induced Thermal Degradation of Inverted Perovskite Solar Cells. *Adv Energy Mater* **7**, 1602922 (2017).

298. Wu, S. *et al.* 2D metal–organic framework for stable perovskite solar cells with minimized lead leakage. *Nat Nanotechnol* **15**, 934–940 (2020).

299. Zhang, S. *et al.* Barrier Designs in Perovskite Solar Cells for Long-Term Stability. *Adv Energy Mater* **10**, 2001610 (2020).

300. Lin, X. *et al.* Efficiency progress of inverted perovskite solar cells. *Energy and Environmental Science* vol. 13 3823–3847 Preprint at https://doi.org/10.1039/d0ee02017f (2020).

301. Pham, H. D. *et al.* Organic interfacial materials for perovskite-based optoelectronic devices. *Energy Environ Sci* **12**, 1177–1209 (2019).

302. Li, X. *et al.* High-Efficiency and Durable Inverted Perovskite Solar Cells with Thermally-Induced Phase-Change Electron Extraction Layer. *Adv Energy Mater* **11**, 2102844 (2021).

303. Wu, M.-H., Lee, J.-H., Leung, M.-K., Liao, C.-C. & Chang, Y. Low-power-consumption and long-lifetime OLED with a high Tg n-type organic transport material. in (eds. Kafafi, Z. H. & Lane, P. A.) 263 (2004). doi:10.1117/12.559561.

304. Greiner, M. T., Chai, L., Helander, M. G., Tang, W.-M. & Lu, Z.-H. Metal/Metal-Oxide Interfaces: How Metal Contacts Affect the Work Function and Band Structure of MoO $_3$. *Adv Funct Mater* **23**, 215–226 (2013).

305. Material price. https://www.metal.com/price,.

306. Man, J.-X., Hu, J.-T., Wang, D.-K., He, S.-J. & Lu, Z.-H. Ytterbium oxide

electron injection interface in organic light-emitting diode. *Appl Phys Lett* **120**, 121101 (2022).

307. Chen, N., Wang, D., Hu, J., Guan, L. & Lu, Z.-H. Measuring Energy Gaps of Organic Semiconductors by Electron Energy Loss Spectroscopies. *physica status solidi (b)* **259**, (2022).

308. Zhang, F. *et al.* Comprehensive passivation strategy for achieving inverted perovskite solar cells with efficiency exceeding 23% by trap passivation and ion constraint. *Nano Energy* **89**, 106370 (2021).

309. Huang, Y. *et al.* Finite perovskite hierarchical structures *via* ligand confinement leading to efficient inverted perovskite solar cells. *Energy Environ Sci* **16**, 557–564 (2023).

310. Li, Z. *et al.* Organometallic-functionalized interfaces for highly efficient inverted perovskite solar cells. *Science (1979)* **376**, 416–420 (2022).

311. Zhu, Z. *et al.* Correlating the perovskite/polymer multi-mode reactions with deep-level traps in perovskite solar cells. *Joule* **6**, 2849–2868 (2022).

312. Chen, B. *et al.* Passivation of the Buried Interface via Preferential Crystallization of 2D Perovskite on Metal Oxide Transport Layers. *Advanced Materials* **33**, 2103394 (2021).

313. Chen, H. *et al.* Regulating surface potential maximizes voltage in all-perovskite tandems. *Nature* **613**, 676–681 (2023).

314. Li, Z. *et al.* Minimized surface deficiency on wide-bandgap perovskite for efficient indoor photovoltaics. *Nano Energy* **78**, 105377 (2020).

315. He, R. *et al.* Pure 2D Perovskite Formation by Interfacial Engineering Yields a High Open-Circuit Voltage beyond 1.28 V for 1.77-eV Wide-Bandgap Perovskite Solar Cells. *Advanced Science* **9**, 2203210 (2022).

316. Zhang, X. *et al.* The Voltage Loss in Tin Halide Perovskite Solar Cells: Origins and Perspectives. *Adv Funct Mater* **32**, 2108832 (2022).

317. Tong, J. *et al.* Wide-Bandgap Metal Halide Perovskites for Tandem Solar Cells. *ACS Energy Lett* **6**, 232–248 (2021).

318. Ganose, A. M., Scanlon, D. O., Walsh, A. & Hoye, R. L. Z. The defect challenge of wide-bandgap semiconductors for photovoltaics and beyond. *Nat Commun* **13**, 4715 (2022).

319. Zhao, L. *et al.* Chemical Polishing of Perovskite Surface Enhances Photovoltaic Performances. *J Am Chem Soc* **144**, 1700–1708 (2022).

320. Carlson, D. E., Lin, G. & Ganguly, G. Temperature dependence of amorphous silicon solar cell PV parameters. in *Conference Record of the Twenty-Eighth IEEE Photovoltaic Specialists Conference - 2000 (Cat. No.00CH37036)* 707–712 (IEEE). doi:10.1109/PVSC.2000.915967.

321. Jiang, Q., Zhang, X. & You, J. SnO_2 : A Wonderful Electron Transport Layer for Perovskite Solar Cells. *Small* **14**, 1801154 (2018).

322. Lee, J. H. *et al.* Interfacial α-FAPbI3 phase stabilization by reducing oxygen vacancies in SnO2−x. *Joule* **7**, 380–397 (2023).

323. Ye, M. *et al.* Recent advances in interfacial engineering of perovskite solar cells. *J Phys D Appl Phys* **50**, 373002 (2017).

324. Kim, M. *et al.* Conformal quantum dot–SnO_2 layers as electron transporters for efficient perovskite solar cells. *Science (1979)* **375**, 302–306 (2022).

325. Jeong, M. *et al.* Stable perovskite solar cells with efficiency exceeding 24.8% and 0.3-V voltage loss. *Science (1979)* **369**, 1615–1620 (2020).

326. Yuan, J. *et al.* Single-Junction Organic Solar Cell with over 15% Efficiency Using Fused-Ring Acceptor with Electron-Deficient Core. *Joule* **3**, 1140–1151

(2019).

327. Burkhard, G. F., Hoke, E. T. & McGehee, M. D. Accounting for Interference, Scattering, and Electrode Absorption to Make Accurate Internal Quantum Efficiency Measurements in Organic and Other Thin Solar Cells. *Advanced Materials* **22**, 3293–3297 (2010).

328. König, T. A. F. *et al.* Electrically Tunable Plasmonic Behavior of Nanocube–Polymer Nanomaterials Induced by a Redox-Active Electrochromic Polymer. *ACS Nano* **8**, 6182–6192 (2014).

329. Hossain, M. I. *et al.* Electrical and Optical Properties of Nickel-Oxide Films for Efficient Perovskite Solar Cells. *Small Methods* **4**, 2000454 (2020).

330. Manzoor, S. *et al.* Optical modeling of wide-bandgap perovskite and perovskite/silicon tandem solar cells using complex refractive indices for arbitrary-bandgap perovskite absorbers. *Opt Express* **26**, 27441 (2018).

331. McPeak, K. M. *et al.* Plasmonic Films Can Easily Be Better: Rules and Recipes. *ACS Photonics* **2**, 326–333 (2015).

332. Vos, M. F. J., Macco, B., Thissen, N. F. W., Bol, A. A. & Kessels, W. M. M. (Erwin). Atomic layer deposition of molybdenum oxide from $(N^tBu)_2(NMe_2)_2Mo$ and O_2 plasma. *Journal of Vacuum Science & Technology A: Vacuum, Surfaces, and Films* **34**, 01A103 (2016).

333. Xie, S. *et al.* Efficient monolithic perovskite/organic tandem solar cells and their efficiency potential. *Nano Energy* **78**, 105238 (2020).

334. Xia, R. *et al.* Optical Analysis for Semitransparent Organic Solar Cells. *Solar RRL* **3**, 1800270 (2019).

335. Werner, W. S. M., Glantschnig, K. & Ambrosch-Draxl, C. Optical Constants and Inelastic Electron-Scattering Data for 17 Elemental Metals. *J Phys Chem Ref*

Data **38**, 1013–1092 (2009).

336. Chen, C.-C. *et al.* Perovskite/polymer monolithic hybrid tandem solar cells utilizing a low-temperature, full solution process. *Mater Horiz* **2**, 203–211 (2015).

337. Liu, J., Lu, S., Zhu, L., Li, X. & Choy, W. C. H. Perovskite-organic hybrid tandem solar cells using a nanostructured perovskite layer as the light window and a PFN/doped-MoO_3/MoO_3 multilayer as the interconnecting layer. *Nanoscale* **8**, 3638–3646 (2016).

338. Li, Z. *et al.* Hybrid Perovskite-Organic Flexible Tandem Solar Cell Enabling Highly Efficient Electrocatalysis Overall Water Splitting. *Adv Energy Mater* **10**, 2000361 (2020).

339. Xie, Y.-M. *et al.* Understanding the role of interconnecting layer on determining monolithic perovskite/organic tandem device carrier recombination properties. *Journal of Energy Chemistry* **71**, 12–19 (2022).

340. Shi, J. *et al.* From Ultrafast to Ultraslow: Charge-Carrier Dynamics of Perovskite Solar Cells. *Joule* **2**, 879–901 (2018).

341. Yan, X. *et al.* Ion migration in hybrid perovskites: Classification, identification, and manipulation. *Nano Today* **44**, 101503 (2022).

342. Zhang, G. *et al.* Renewed Prospects for Organic Photovoltaics. *Chem Rev* **122**, 14180–14274 (2022).

343. Meredith, P., Li, W. & Armin, A. Nonfullerene Acceptors: A Renaissance in Organic Photovoltaics? *Adv Energy Mater* **10**, 2001788 (2020).

344. Wang, K. *et al.* Overcoming Shockley-Queisser limit using halide perovskite platform? *Joule* **6**, 756–771 (2022).

345. David R Lide. *CRC handbook of chemistry and physics*.

346. Ohno, Y. XPS studies of the intermediate valence state of Yb in (YbS)1.25CrS2. *J Electron Spectros Relat Phenomena* **165**, 1–4 (2008).

347. Lang, W. C., Padalia, B. D., Watson, L. M. & Fabian, D. J. Reinvestigation of the core levels of pure and oxydised ytterbium and lutetium. *J Electron Spectros Relat Phenomena* **7**, 357–358 (1975).

348. Hu, J. *et al.* Damage-Free Depth Profiling of Electronic Structures in Multilayered Organic Semiconductors by Photoelectron Spectroscopy and Cluster Ion Beam. *physica status solidi (b)* **258**, 2100130 (2021).

349. Lof, R. W., van Veenendaal, M. A., Koopmans, B., Jonkman, H. T. & Sawatzky, G. A. Band gap, excitons, and Coulomb interaction in solid <math display="inline"> <mrow> <msub> <mrow> <mi mathvariant="normal">C</mi> </mrow> <mrow> <mn>60</mn> </mrow> </msub> </mrow> </math>. *Phys Rev Lett* **68**, 3924–3927 (1992).

350. Dhanasankar, M., Purushothaman, K. K. & Muralidharan, G. Optical, structural and electrochromic studies of molybdenum oxide thin films with nanorod structure. *Solid State Sci* **12**, 246–251 (2010).

Publications

(Co-)first authored works

1. **Yun Xiao**[#], Xiaoyu Yang[#], Rui Zhu and Henry J. Snaith, Unlocking Interfaces in Perovskite Photovoltaics. Under review, 2023
2. **Yun Xiao**[#], Fan Xu[#], Xiaoyu Yang[#], Peng Chen, Maotao Yu, Shunde Li, Qiuyang Li, Lichen Zhao, Lei Li, Tinglu Song, Bin Liu, Rui Zhu and Henry J. Snaith, Geometric Manipulation for Efficient Wide-Bandgap Perovskite Solar Cells. In preparation. (**Chapter 4**)
3. **Yun Xiao**[#], Peng Chen[#], Xiaohan Jia[#], Nan Chen, Deying Luo, Juntao Hu, Hongyu Xu, Congmeng Li, Shunde Li, Xin Jiang, Maotao Yu, Haoming Yan, Haoxin Chen, Bin Liu, Qiuyang Li, Suhas Mahesh, Lei Li, Hui Li, Dengke Wang, Xiaojun Li, Zheng-Hong Lu, Moritz Riede, Rui Zhu and Henry J. Snaith. Ytterbium Oxide-based Interconnecting Layer for Monolithic Peorvksite-organic Tandem Solar Cells with Small Voltage Loss, In preparation. (**Chapter 6**)
4. Peng Chen[#], **Yun Xiao**[#], Lei Li[#], Lichen Zhao, Maotao Yu, Shunde Li, Juntao Hu, Bin Liu, Yingguo Yang, Deying Luo, Cheng-Hung Hou, Xugang Guo, Jing-Jong Shyue, Zheng-Hong Lu, Qihuang Gong, Henry J. Snaith and Rui Zhu, Efficient Inverted Perovskite Solar Cells via Improved Sequential Deposition. *Advanced Materials*, 2023, 35(5): 2206345.
5. Peng Chen[#], **Yun Xiao**[#], Juntao Hu[#], Deying Luo, Shunde Li, Rui Su, Pietro Caprioglio, Pascal Kaienburg, Xiaohan Jia, Nan Chen, Jingjing Wu, Yanping Sui, Pengyi Tang, Haoming Yan, Tianyu Huang, Maotao Yu, Qiuyang Li, Lichen Zhao, Dengke Wang, Xiaojun Li, Qing Zhao, Qihuang Gong, Zheng-Hong Lu, Henry J. Snaith, Rui Zhu, Multifunctional ytterbium oxide buffer for perovskite solar cells, Under review, 2023 **(Chapter 5)**
6. Peng Chen[#], **Yun Xiao**[#], Shunde Li[#], Xiaohan Jia, Wei Zhang, Henry J. Snaith, Qihuang Gong and Rui Zhu, The Promise and Challenges of Inverted Perovskite Solar Cells. Submitted, 2022 (**Section 2.3**)
7. Shunde Li[#], **Yun Xiao**[#], Rui Su[#], Linjie Dai[#], Deying Luo, Peng Chen, Pietro Caprioglio, Karim Elmestekawy, Cullen Chosy, Milos Dubajic, Juntao Hu, Irfan Habib, Akash Dasgupta, Dengyang Guo, Szymon Zelewski, Zhangyuchang Lu,

Tianyu Huang, Qiuyang Li, Haoming Yan, Lichen Zhao, Dengke Wang, Moritz Riede, Laura M. Herz, Zheng-Hong Lu, Qihuang Gong, Samuel D. Stranks, Henry J. Snaith and Rui Zhu, Realizing high-quality micron-scale-thick perovskite absorber for efficient and stable p-i-n solar cells. Submitted.

8. Hongyu Xu[#], **Yun Xiao**[#], Pietro Caprioglio, Qiuyang Li, Karim Elmestekawy, Lichen Zhao, Laura M. Herz, Moritz Riede, Henry J. Snaith and Rui Zhu. Minimizing the Voc losses for efficient and stable perovskite solar cells. In preparation.

Other authored works

1. Jiang Wu[#], Peng Chen[#], Han Xu, Maotao Yu, Lei Li, Haoming Yan, Yiming Huangfu, **Yun Xiao**, Xiaoyu Yang, Lichen Zhao, Wei Wang, Qihuang Gong, Rui Zhu, Ultralight flexible perovskite solar cells. *Science China Materials*, 2022, 65(9): 2319-2324.
2. Lei Li, Peng Chen, Hongyu Xu, Qiuyang Li, Qixuan Zhong, Haoming Yan, Xiaoyu Yang, Juntao Hu, Shunde Li, Tianyu Huang, **Yun Xiao**, Bin Liu, Huiliang Sun, Xugang Guo, Zheng-Hong Lu, Henry J. Snaith, Qihuang Gong, Lichen Zhao, Rui Zhu, Buried-metal-grid electrodes for efficient parallel-connected perovskite solar cells. *Advanced Materials*. DOI: 10.1002/adma.202305238.
3. Yongqiang Ji[#], Qixuan Zhong[#], Maotao Yu, Haoming Yan, Zhongchen Xing, Lei Li, Qiuyang Li, Hongyu Xu, Shunde Li, Peng Chen, Lei Zhao, Xiaohan Jia, **Yun Xiao**, Fan Xu, Lichen Zhao, Deying Luo, Xiaoyu Yang, Qihuang Gong, Xinqiang Wang, Rui Zhu. Monodispersed FAPbI3 nanocrystallite films enable efficient near-infrared light-emitting diodes. Submitted.

[#] denotes equal contribution.